

UNIVERSITÀ DEGLI STUDI DI TRIESTE



XXIV ciclo del Dottorato di Ricerca in Fisica

settore scientifico disciplinare FIS03 Fisica della Materia

**Structural investigation of  
complex surface interfaces by  
means of X-ray Photoelectron  
Diffraction**

Dottoranda:  
Rong Rong Zhan

Direttore Scuola di Dottorato:  
Chiar.mo Prof. Paolo Camerini

Supervisore:  
Dott. Alessandro Baraldi

Correlatore:  
Dott. Erik Vesselli

Anno accademico 2010–2011



# Abstract

In these three years of research activity, I have carried out a series of experiments aimed at the structural determination of low-dimensional atomic systems, including artificially grown phases, formed on transition metal surfaces. X-ray Photoelectron Diffraction (XPD) has been the main technique employed in all these experiments, and it has proved to be an excellent approach for an accurate structural determination of different surface phases. A particular attention has been devoted to the growth of ultra-thin films on well-oriented metal surfaces, ranging from ultra-thin oxide films, to surfactant metallic ad-layers and adsorbed alkali metal films on epitaxial graphene. The considerable interest in these systems is stimulated by the perspective that peculiar electronic and magnetic properties can arise as an effect of the spatial confinement of the surface electronic states and of the stress induced by lattice matching. For these reasons, XPD plays an important role in the attempt to establish a relationship between a given interface structure and its physical and chemical properties.

Most of the surface systems I investigated are related to ultra-thin oxide films. For instance, the interface matching between  $\text{RhO}_2$  and the  $\text{Rh}(100)$  substrate was studied in close relationship with the bulk  $\text{RhO}_2$  structure. The observed interface matching and buckling were successfully explained on the basis of the analogy with the bulk phase bonding configuration. A thorough structural characterization was carried out both for the Ni layers grown on  $\text{Rh}(111)$  and for the different ordered phases obtained by Ni overlayer post-oxidation. The mechanism of strain relaxation occurring in the Ni adlayers during Ni deposition was determined by means of XPD. A quasi-2D Ni oxide was observed and studied by means of photoemission measurements, in order to characterize their chemical and geometrical properties. I also took part in the XPD analysis of a two-dimensional  $\text{Mn}_x\text{O}_y$  layer formed on the vicinal surface of  $\text{Pd}(100)$ : the local structure of this thin oxide film was determined and compared with the corresponding phase observed on a flat Pd substrate. In another experiment, a surfactant Pb monolayer was grown on the  $\text{Ag}(100)$  surface, and subsequently characterized from both the structural and electronic point of view. The combined use of XPD and ARPES in our investigations allowed us a deep understanding of the local interactions involved in the formation of this commensurate ultra-thin Pb film. Finally, in this dissertation I will present the results of a study on the adsorption configuration formed by K on a quasi-free-standing graphene layer epitaxially grown on  $\text{Ir}(111)$ . In this case, we employed XPD for a detailed structural determination of the K-doped graphene layer,

---

which led to a final result showing an excellent agreement with the theoretical calculations based on density functional theory.

# Abstract

Durante questi tre anni di attività di ricerca, ho portato a termine una serie di esperimenti finalizzati alla caratterizzazione strutturale di sistemi atomici a bassa dimensionalità, cresciuti su cristalli singoli di metalli di transizione. La tecnica di Diffrazione di raggi X (XPD), che ho utilizzato per investigare tutti i sistemi discussi in questa tesi, si è dimostrata un approccio sperimentale ideale per la determinazione della geometria delle superfici su scala atomica con un elevato grado di accuratezza. Una particolare attenzione è stata dedicata alla crescita di film ultra-sottili, come nel caso dei film di ossidi di superficie, degli strati singoli di metalli pesanti debolmente interagenti con il substrato, e dell'adsorbimento di metalli alcalini su un supporto di grafene cresciuto epitassialmente su metalli di transizione. La principale motivazione che ha spinto allo studio di questi sistemi consiste nella possibilità di osservare, in questi materiali innovativi, nuove proprietà elettroniche e magnetiche indotte dal confinamento degli stati elettronici di superficie e dallo stress reticolare tra adsorbati e substrato. A questo riguardo, la determinazione strutturale attraverso l'XPD ha un ruolo fondamentale per la comprensione del legame tra gli effetti di struttura all'interfaccia tra film sottili e supporto e le loro proprietà fisiche e chimiche.

La maggior parte dei sistemi superficiali che ho studiato è legata ai film ultrasottili di ossidi di superficie. Ad esempio, la geometria locale derivante dalla sovrapposizione tra l'ossido di superficie di Rh e la superficie di Rh(100) è stata studiata in stretta relazione con la geometria del legame tra Rh e O in un solido cristallino di tipo  $\text{RhO}_2$ . Questa analisi ci ha permesso di spiegare la geometria di adsorbimento dell'ossido di superficie e la deformazione locale osservata sulla superficie del substrato. Un secondo esperimento descritto in questa tesi riguarda lo studio della crescita epitassiale di strati sottili di Ni sulla superficie di Rh(111) e la caratterizzazione strutturale di un ossido di Ni bidimensionale su Rh(111). In quest'ultimo caso è stato spiegato, attraverso un'analisi strutturale basata sull'XPD, il meccanismo di rilassamento dello stress reticolare accumulato durante la crescita del film. Inoltre, l'ossido di Ni supportato da Rh(111) è stato caratterizzato dal punto di vista sia chimico che strutturale. Ho anche partecipato allo studio di un film quasi bidimensionale di  $\text{Mn}_x\text{O}_y$  cresciuto su una superficie steppata del Pd. Il risultato da noi ottenuto, mediante un procedimento di rilassamento strutturale dell'ossido di Mn sulle singole terrazze di Pd, è stato messo a confronto con la struttura dello stesso ossido sulla Pd(100). In un altro lavoro sperimentale, un singolo strato di Pb è stato cresciuto su Ag(100).

---

Successivamente, abbiamo investigato sia la struttura atomica sia la dispersione degli stati elettronici di superficie per interpretare l'interazione all'interfaccia tra Pb e substrato. In questo caso il nostro approccio sperimentale, basato sulla combinazione di due tecniche complementari, XPD e ARPES, ci ha permesso di ottenere una migliore comprensione del processo di formazione del film sottile di Pb. Infine, in questa tesi verrà presentato anche lo studio della geometria d'adsorbimento di atomi di K sullo strato singolo di grafene supportato da Ir(111). Mediante l'impiego dell'XPD su questo sistema, sono stati determinati i siti di adsorbimento degli atomi di K e la loro distanza dagli atomi di carbonio sottostanti, confermando il risultato teorico dei calcoli basati sulla DFT.

# Contents

<b>1</b>	<b>Introduction</b>	<b>1</b>
<b>2</b>	<b>X-ray Photoelectron Diffraction</b>	<b>11</b>
2.1	Photoelectron diffraction theory . . . . .	12
2.1.1	X-ray Photoelectron Spectroscopy . . . . .	12
2.1.2	Photoelectron scattering . . . . .	20
2.2	Experimental setup . . . . .	28
2.2.1	Sample preparation . . . . .	28
2.2.2	X-ray excitation sources . . . . .	30
2.2.3	Electron energy analyzer . . . . .	32
2.2.4	Experimental stations . . . . .	34
2.3	Structural determination . . . . .	38
2.3.1	Photoemission spectra line-shape . . . . .	38
2.3.2	Data processing and theoretical simulations . . . . .	39
<b>3</b>	<b>O-Rh-O trilayer on Rh(100)</b>	<b>47</b>
3.1	Introduction . . . . .	47
3.2	Experimental setup . . . . .	49
3.3	LEED and XPS data discussions . . . . .	50
3.4	XPD results . . . . .	52
3.5	Discussion on the interface structure . . . . .	57
3.6	Conclusions . . . . .	59
<b>4</b>	<b>Ni oxide nanostructures on Rh(111)</b>	<b>63</b>
4.1	Introduction . . . . .	63
4.2	Experimental setup . . . . .	66
4.3	Phase study of the oxidation of ultra-thin Ni films . . . . .	66
4.3.1	Quasi 2D Ni oxides at $\theta_{\text{Ni}} \leq 1$ ML . . . . .	67
4.3.2	Oxidation of $\theta_{\text{Ni}} \geq 2$ ML Ni films . . . . .	72
4.4	Structure of the p(2×2)-O phase $\theta_{\text{Ni}} = 5$ ML . . . . .	74

4.4.1	XPD data and simulation details . . . . .	75
4.4.2	O-induced Ni surface buckling . . . . .	76
4.4.3	Strain relaxation mechanism . . . . .	78
4.5	The 2D $(2\sqrt{3} \times 2)$ - <i>rect</i> -NiO phase . . . . .	80
4.5.1	The <i>ad hoc</i> computational method used in XPD . . . . .	81
4.5.2	Structure determination of the $(2\sqrt{3} \times 2)$ - <i>rect</i> phase . . . . .	85
4.6	Conclusions . . . . .	89
<b>5</b>	<b>Mn<sub>3</sub>O<sub>4</sub> oxide film on stepped Pd(1 1 17)</b>	<b>93</b>
5.1	Introduction . . . . .	93
5.2	Experimental and computational details . . . . .	95
5.3	DFT structural model . . . . .	96
5.4	Structural determination of the thin oxide film by means of XPD . . . . .	97
5.5	Conclusions . . . . .	101
<b>6</b>	<b>Surfactant Pb monolayer on Ag(100)</b>	<b>105</b>
6.1	Introduction . . . . .	105
6.2	Experimental details . . . . .	107
6.3	Qualitative analysis of the $c(6 \times 2)$ -Pb phase . . . . .	107
6.4	XPD results . . . . .	109
6.5	Valence band studies by means of ARPES . . . . .	116
6.6	Conclusions . . . . .	119
<b>7</b>	<b>K adsorption on epitaxial graphene</b>	<b>123</b>
7.1	Introduction . . . . .	123
7.2	Experimental setup . . . . .	124
7.3	Preliminary considerations . . . . .	125
7.4	Structural determination by means of XPD . . . . .	127
7.5	Conclusions . . . . .	131
<b>A</b>	<b>Publications</b>	<b>135</b>
<b>B</b>	<b>List of the Acronyms</b>	<b>137</b>

# Chapter 1

## Introduction

In the past few decades, the development of state-of-art surface science techniques has largely increased the available knowledge on low-dimensional atomic systems. Among these, a relevant class of innovative materials is represented by *ultra-thin films* of different nature. Nowadays it is widely acknowledged that by exploiting the controlled growth of ultra-thin films, and other atomic size nano-materials, new challenging research directions can open up. In fact, the discovery of the size-dependent properties of these systems has gained insight into the possibility of engineering artificial surface structures with tailored structural, electronic and magnetic properties. During my PhD, I have mainly investigated ultra-thin metal oxide films and epitaxial metal adlayers grown on Transition Metal (TM) single crystals. Both of them find relevant applications in the development of low cost functionalized materials for coatings and corrosion-resistant layers [1], in the fabrication of dielectrics for gas sensors [2], and in the production of nano-electric contacts, as well as of magnetic elements for data storage devices [3]. Finally, surface thin films could also play an important role in the engineering of heterogeneous catalysts with high activity and selectivity [4].

It should be stressed that both the fabrication of nano-devices and the engineering of an optimal catalyst have to face a common problem: the complexity of the structures and the interactions involved in the interface between the thin film and the metal support. The larger the spatial confinement of a system is, the higher its surface-to-bulk ratio will be. It follows that the interface characteristics can play a relevant role in determining the structural and electronic state properties of the whole system. In this respect, a key issue for the future technological developments is the exact understanding of how the atomic interactions at the interface shape the actual thin film structure.

Ultra-thin oxide films represent ideal candidates for the supported growth of metal atoms or clusters, which are believed to be very promising catalysts [5]. Moreover, the atomic arrangement at the interface between the adsorbates and the substrate plays a key role in controlling the surface reactivity [6]. It has been suggested that, in principle, when the film thickness is below a critical

---

value ( $3 \text{ ML} < \theta_{cr} < 15 \text{ ML}$ ), the charge state and the binding sites of the adsorbates can be opportunely determined, by exploiting a Cabrera-Mott [7] charge transfer mechanism, also by controlling the location of point defects or the film thickness [4,8,9]. Examples of this kind are provided by studies of the growth of Au and Pd clusters on thin oxide films such as MgO and alumina [10–12]. These atomic species, indeed, are observed to preferentially aggregate close to point defects of the supported ultra-thin oxide films [4]. This suggests that, if one had the capability of fabricating ultra-thin films with a controlled defect density and location, he could tailor these 1D catalysts in a selected way. On a defect-free thin film, however, charging of the adatoms at the interface is another process which increases the surface complexity [13]. For instance, Au atoms adsorbed on MgO(100) are neutral, while those deposited on a supported ultra-thin MgO film are observed to accumulate a negative charge, thus becoming  $\text{Au}^-$  ions [11]. Although the mechanism and the extent of such an interface charge transfer between adsorbates and ultra-thin oxide films have not been completely understood yet, these findings have clearly evidenced new opportunities offered by the interface physics of ultra-thin films.

The use of crystalline ultra-thin oxide films has recently gained new insights into the Tunneling MagnetoResistance (TMR) effect widely observed in the Magnetic Tunnel Junctions (MTJ). An MTJ consists of an insulating barrier, typically a thin oxide film, sandwiched between two ferromagnetic layers. The thickness of the insulating barrier is so small that the electrons can tunnel through it when a bias is applied to the junction. Since the intensity of the tunneling current depends on the relative magnetic orientation of the two ferromagnet layers, which can be changed by applying an external field, this allows to magnetically manipulate the resistance of the junction, a property called magnetoresistance [14]. This peculiarity of MTJs has attracted considerable attentions due to its potential applications in the fabrication of magnetic non-volatile random access memories and storage devices [15,16]. When using crystalline thin oxide films, such as MgO and  $\text{Al}_2\text{O}_3$ , instead of an amorphous insulating barrier, large values of the TMR have been measured [17]. This has in turn stimulated the investigation of the role of well-ordered ultra-thin oxide films in MTJ [17]. Experimental evidence has been proved that both the spin polarization of the ferromagnetic layers and the TMR of the system are strongly affected by the atomic potentials and bonding lengths at the interface between the oxide thin film and each of the two ferromagnetic layers [18,19]. Though the study of the MTJs is beyond the scope of this thesis, it represents an important example of how the complex interface structural effects can dramatically modify the conductive and magnetic properties of a low-dimensional system, especially in the case of ultra-thin films.

As mentioned before, a large part of the research work done during my PhD concerned the structural determination of different kinds of ultra-thin oxide films. One of my first studies was about the  $\text{RhO}_2$  thin films formed on Rh(100), which play an important role in the debate on the relationship between the oxide film formation and the surface reactivity of TM single crystals.

Besides, our structural analysis devoted particular attention to the interface matching between the  $\text{RhO}_2$  film and the substrate. An interesting similarity was established between the film–substrate interface and the  $\text{RhO}_2$  bulk phase local structure, thus highlighting the interplay between the interface buckling effects and the bonding geometries that stabilize the film growth. A second class of ultra-thin oxide films I investigated are the  $3d$ -TM oxide films, such as Ni and Mn oxides. As it will be discussed in detail in chapter 4, these oxides are distinctly characterized by strong Charge Transfer (CT) effects and by  $d$ – $d$  electron Coulomb repulsions, which both contribute to determining the peculiar insulating properties of the film, as first predicted by Mott [20]. This aspect is also reflected in the photoemission spectra of both the  $\text{Ni}2p_{3/2}$  and  $\text{Mn}2p_{3/2}$  core level components of the oxide films. These spectra exhibit multiple core level Binding Energy (BE)–shifted components, owing to the presence of different charge transfer channels from the ligand atoms to the excited metal atoms (Ni or Mn). In addition, ultra-thin Mn oxide films are characterized by a critical interplay among the effects of lattice strain, interface reconstruction and total spin polarization.

Studying the formation of bimetallic nanoclusters, nanofilms and surface alloys is of great interest for the comprehension of fundamental topics in solid state physics such as quantum-size effects [21], surface segregation [22,23] and spin-orbit interactions [24]. More specifically, transition metal thin films have been widely studied in relation to the possibility of manipulating their chemical and electronic properties in such a way to enhance their catalytic activity [25]. Spin-splitting electron band structures are observed in ultra-thin heavy metal films supported on noble metals [26]. This phenomenon was explained for the first time by Rashba and Bychkov (RB) [27]. In the RB model, the spin degeneracy is lifted when the structural inversion symmetry is broken along the direction normal to the surface. Hence the spin-orbit term of the electron Hamiltonian gives rise to two non-degenerate valence states instead of one, which are observed as splitted bands in Angle-Resolved PhotoEmission Spectroscopy (ARPES). Pb ultra-thin films represent a possible example of Rashba-type spin-splitting systems. In addition, in a few ML-thick Pb film, Dil *et al.* observed both the presence of splitted electron states and their dependence on the interface matching effects rather than on the film thickness [28]. Hence the perspective of controlling the spin polarization by means of interface manipulations has been suggested. The understanding of these complex interfaces has motivated our structural investigation of Pb thin films supported by Ag(100) surface, as will be described in chapter 6. The epitaxial growth of metallic films, on the other hand, stressed out the importance of the lattice strain for the stability and properties of the surface phases during the matching process between the overlayer and the substrate.

The single layer of graphite, or *graphene* (GR), has been one of the most popular examples of monolayer thin films in the last decade. Even if this outstanding material had actually been discovered, though not as a free-standing graphene

---

layer, long before the publication of the paper by Geim and Novoselov [29], they were the first scientists who recognized the massive potential of GR for future technological applications. Charge carriers in GR are found to exhibit a giant intrinsic mobility, zero effective mass, and to travel for micrometers without being scattered at room temperature. Hence GR is a promising material for the fabrication of atomic scale devices with a much higher carrier density and mobility compared to semiconductors [30]. However, GR has a gapless band structure, which makes it unsuitable for application in nanoelectronics. Many methods have been proposed for manipulating the electronic band structure of GR, which often exploit its high sensitivity to the lattice symmetry. For example, the presence of non-equivalent C atoms in a GR layer breaks the in-plane symmetry of the latter and opens a bandgap at the Dirac crossing point [31]. Moreover, a selective alkali atom doping of supported GR seems to provide a viable method for tuning the bandgap [32,33]. However, a thorough understanding of the bonding mechanism between GR and the adsorbates is the starting point for the interpretation of all the interactions involving GR. In this respect, we carried out a study of K adsorption on GR/Ir(111) (reported in chapter 7), which represents a model system for the investigation of both the GR–dopant interaction and the effects of GR doping on the GR–substrate bond strength.

Since the interface effects between the ultra-thin film and the substrate can determine the physical and chemical properties of the whole system, the knowledge of the atomic identities, positions, and bonding mechanisms in the first few atomic layers is essential to get a quantitative microscopic understanding of the macroscopic properties of a low-dimensional material. This includes information on the bond directions and distances, coordination numbers, site symmetries, and the degree of long- and short-range order characterizing the sampled region.

**X-ray Photoelectron Diffraction (XPD)** is an experimental technique which allows to shed light on many of the structural aspects listed above, and it is also the main experimental approach that I have used in all the scientific projects carried out during my PhD. XPD is a powerful tool for the structural investigation of complex interfaces, for several reasons. First of all, when performing an XPD experiment, the probe is the sample itself. In fact, a photoelectron emitted from a photoexcited atom and then elastically scattered by the other atoms around the emitter during its travel to the sample surface, carries information both about the emitting atom and about the scatterers. Therefore, XPD data always supply a wealth of information about the local geometry, which is why this technique is known for its outstanding local sensitivity. It follows that long-range order is not a requirement when performing this kind of measurements. In addition, XPD is based on photoelectron diffraction processes originating from localized core levels, which ensures a high sensitivity to the different atomic species and to the chemically non-equivalent bound states. The local specificity and the surface sensitivity are the characteristics that make the XPD technique particularly suitable for structural determinations of the low-dimensional surface systems, such as ultra-thin films supported by TM surfaces. Due to the lattice stresses occurring at the interface region, many quasi-2D nano-structures usually present point defects, differently oriented domain boundaries and lack of

long-range order, thus troubling those diffraction techniques that necessarily require well-ordered sample surfaces. By contrary, XPD is affected by these effects to a smaller extent, because the XPD signal prevalently reflects the local atomic arrangement, as described above. Moreover, by using the synchrotron radiation to stimulate the photoemission process, XPD can be extremely surface sensitive thanks to the tunable photon energy. This enhanced surface sensitivity is certainly a key requirement for the study of the low-dimensional nano-systems. The wide range of surface phases studied by means of XPD and reported in this dissertation also proved the versatility of this experimental technique for applications on systems of different nature. However, since the experimental XPD patterns are actually interference patterns and not a pure image of the sample structure, the structural determination is typically obtained by means of the comparison between experimental data and simulation results. Hence the employment of appropriate simulation codes is necessary and sometimes *ad hoc* simulation procedures have to be implemented. In addition, XPD technique doesn't provide every useful information about the system under investigation. For instance, while the XPD is an efficient probe of the atomic structure, it ignores the details of the electronic structure of the investigated system. These are the reasons why in surface science more than one surface sensitive technique is generally used for the analysis of the same system, thus providing complementary information and leading to a more complete and reliable final result. Indeed, besides X-ray photoelectron diffraction, there are several other methods used for the characterization of low-dimensional surface systems. The most widely used ones are Scanning Tunnelling Microscopy (STM), Grazing Incidence X-ray diffraction (GIXRD) and Low Energy Electron Diffraction (LEED).

Scanning tunnelling microscopy, as well as scanning tunnelling spectroscopy (STS), are two surface-specific techniques which both exploit the electron tunnelling mechanism ensuing between the sample and a metallic tip when they are placed at a mutual distance of few Å (comparable with atomic dimensions). STM allows to explore the surface topography with atomic resolution, while STS yields insight into the surface electronic Density Of States (DOS), which is not accessible to XPD. However, these two techniques are not very sensitive to the chemical identity of the surface atomic species, nor to the chemical bonding state of the atoms on the sample. Most importantly, while STM and STS provide detailed information on the sample surface, they do not allow the exploration of the interface region below the sample surface. This means that, in many cases, when using only STM or STS, a direct characterization of the interface lattice matching mechanisms or the strain-induced reconstructions is usually precluded. On the other hand, when using XPD as a probe, the sampling depth can be adjusted by changing the photon energy, so that we can choose to stimulate photoemission from the surface as well as from the deeper atomic layers underneath the sample surface. Another non-trivial issue related to STM and STS is the strong dependence of the electronic tunnelling process on the DOS of both the sample surface and the tip. As a consequence, the image (or spectrum) that is measured is actually a superposition of the contributions of both the sample and the tip, and an accurate deconvolution is needed in order

---

to isolate the information regarding only the sample surface. This makes the interpretation of the data acquired with electron tunnelling-based techniques less straightforward [34].

Grazing incidence X-ray diffraction is another surface sensitive technique widely adopted for the investigation of ultra-thin films, especially for monitoring the epitaxial growth of semiconductor films [35]. This technique exploits a well-collimated X-ray beam as a probe and allows modelling the lattice structure of the sample by analysing the intensity and positions of the diffracted beams in the reciprocal space. For these studies, synchrotron radiation (SR) is generally required, owing to its high photon flux and narrow angular spread, which are a fundamental requirement for performing GIXRD. In order to ensure a high surface sensitivity, GIXRD experiments are typically carried out at very grazing incidence angles, in such a way to work in total external reflection conditions, thus limiting the beam penetration to the near-surface region of the sample. The primary advantage of GIXRD with respect to XPD relies on the longer Inelastic Mean Free Path (IMFP) of X-ray beams compared to that of photoelectrons in a high background pressure. For example, *in situ* GIXRD measurements allow to monitor the sample surface even during the epitaxial growth of a film, which generally represents a prohibitive condition for all electron diffraction-based techniques. Nevertheless, GIXRD can be efficiently employed only on crystalline samples with a long-range ordered lattice structure. XPD, on the contrary, is affected by the lack of long-range order to a much smaller extent due to its local structural sensitivity, since the scattering events take place at atoms localized around the emitter rather than at Bragg planes. Furthermore, the identification of the atomic species and of the chemical states by means of GIXRD is also less straightforward than by using XPD, especially in the case of new surface phases which do not have a reference in the X-ray diffraction database.

Finally, LEED is also an excellent surface sensitive technique which yields direct insight into the symmetry and periodicity of the sample surface. Besides, it is an effective tool to monitor the lattice commensurability between layers of different geometries during lattice matching processes. Similarly to GIXRD, LEED is based on Bragg diffraction, but a low energy electron beam is employed as a probe. It is not sensitive to chemical states, and long-range order is needed for the same reasons as the ones illustrated for GIXRD. A more quantitative application of this technique is represented by LEED I-V, which allows investigating the surface structure by studying the intensity (I) modulations of a diffracted electron beam as a function of the electron energy (V). However, LEED I-V shows a higher sensitivity to the interlayer spacing with respect to the in-plane bond distances, and its effective sampling depth is limited to few atomic layers, due to the small electron IMFP at low energies.

Since different experimental approaches provide complementary structural information, surface scientists often employ a combination of different techniques to probe the same surface phase. In fact, many scientific projects I have been involved in during my PhD have been carried out by combining the re-

sults obtained from XPD, ARPES, LEED and STM measurements. Moreover, a fundamental support on the theoretical front has been provided by Density Functional Theory (DFT) calculations. Besides the experimental setup required to perform an XPD experiment, the main difficulty of this technique concerns its data analysis. In fact, since XPD data basically consist of interference patterns, the structural determination of a system is typically based on the comparison between the experimental and the simulated XPD patterns, as obtained on the basis of theoretical structural models. In this regard, I learned to run two different XPD simulation codes, both used for the calculations of multiple scattering pathways and photoelectron wave functions, in order to simulate the resulting interference patterns. Moreover, a considerable amount of time was devoted to the development of new methods for our XPD analysis, which allowed us to avoid the simplest but time consuming trial-and-error procedure and to achieve the best fitting theoretical model in a more efficient way. In particular, thanks to the employment of the steepest descent algorithm and of genetic algorithms for the implementation of a custom-made method for our XPD analysis, the structural determination of several surface phases was made possible.

This thesis is organized as follows. Chapter 2 describes in detail the x-ray photoelectron diffraction technique, both from the theoretical and from the experimental point of view. An introduction to the underlying physics of this technique will be given, and the basic experimental equipment needed to perform XPD measurements will be briefly described. Chapter 3 reports on the results of our structural analysis of the  $\text{RhO}_2/\text{Rh}(100)$  system. Chapter 4 is devoted to the epitaxial growth of Ni layers on  $\text{Rh}(111)$ , as well as to the 1D and 2D nickel oxides obtained from the post-oxidation of the deposited Ni films. In chapter 5 the atomic structure of ultra-thin  $\text{Mn}_3\text{O}_4$  grown on stepped Pd surface is studied in comparison with a similar oxide film formed on a flat Pd surface. The deposition of Pb layers on  $\text{Ag}(100)$  and the subsequent structural and electronic valence band investigation of the system will be discussed in chapter 6. Finally, in chapter 7, I will present a study of atomic K adsorbates on epitaxial graphene supported on  $\text{Ir}(111)$ .

---

## References

- [1] Mayrhofer, P. H., Hovsepian, P. E., Mitterer, C. & Münz, W. D. Calorimetric evidence for frictional self-adaptation of TiAlN/VN superlattice coatings. *Surf. Coat. Tech.* **177**, 341 (2004).
- [2] Wan, Q. *et al.* Fabrication and ethanol sensing characteristics of ZnO nanowire gas sensors. *Appl. Phys. Lett.* **84**, 3654 (2004).
- [3] Chappert, C., Fert, A. & Van Dau, F. N. The emergence of spin electronics in data storage. *Nat. Mater.* **6**, 813 (2007).
- [4] Freund, H. J. & Pacchioni, G. Oxide ultra-thin films on metals: new materials for the design of supported metal catalysts. *Chem. Soc. Rev.* **37**, 2224 (2008).
- [5] McClure, S. M. & Goodman, D. W. New insights into catalytic CO oxidation on Pt-group metals at elevated pressures. *Chem. Phys. Lett.* **469**, 1 (2009).
- [6] Kulawik, M., Nilius, N. & Freund, H. J. Influence of the metal substrate on the adsorption properties of thin oxide layers: Au atoms on a thin alumina film on NiAl(110). *Phys. Rev. Lett.* **96**, 036103 (2006).
- [7] Ocal, C., Ferrer, S. & García, N. Cabrera-moti mechanism for oxidation of metals explains diffusion of metallic atoms through thin defective oxide layers. *Surf. Sci.* **163**, 335 (1985).
- [8] Yoon, B. *et al.* Charging effects on bonding and catalyzed oxidation of CO on Au<sub>8</sub> clusters on MgO. *Science* **307**, 403 (2005).
- [9] Repp, J., Meyer, G., Olsson, F. E. & Persson, M. Controlling the charge state of individual gold adatoms. *Science* **305**, 493 (2004).
- [10] Ricci, D., Bongiorno, A., Pacchioni, G. & Landman, U. Bonding trends and dimensionality crossover of gold nanoclusters on metal-supported MgO thin films. *Phys. Rev. Lett.* **97**, 036106 (2006).
- [11] Sterrer, M. *et al.* Control of the charge state of metal atoms on thin MgO films. *Phys. Rev. Lett.* **98**, 096107 (2007).
- [12] Nilius, N. *et al.* Counting electrons transferred through a thin alumina film into Au chains. *Phys. Rev. Lett.* **100**, 096802 (2008).
- [13] Zhang, C., Yoon, B. & Landman, U. Predicted oxidation of CO catalyzed by Au nanoclusters on a thin defect-free MgO film supported on a Mo(100) surface. *J. Am. Chem. Soc.* **129**, 2228 (2007).
- [14] Moodera, J. S., Kinder, L. R., Wong, T. M. & Meservey, R. Large magnetoresistance at room temperature in ferromagnetic thin film tunnel junction. *Phys. Rev. Lett.* **74**, 3273 (1995).

- [15] Åkerman, J. Toward a universal memory. *Science* **308**, 508 (2005).
- [16] Chambers, S. A. *et al.* Ferromagnetism in oxide semiconductors. *Mater. Today* **9**, 28 (2006).
- [17] Parkin, S. S. P. *et al.* Giant tunnelling magnetoresistance at room temperature with MgO(100) tunnel barriers. *Nat. Mater.* **3**, 862 (2004).
- [18] Tsymbal, E. Y. *et al.* Interface effects in spin-dependent tunneling. *Prog. Mater. Sci.* **52**, 401 (2007).
- [19] Niizeki, T., Sukegawa, H., Mitani, S., Tezuka, N. & Inomata, K. Correlation between symmetry-selective transport and spin-dependent resonant tunneling in fully epitaxial Cr/ultrathin-Fe/MgO/Fe(001) magnetic tunnel junctions. *Appl. Phys. Lett.* **99**, 182508 (2011).
- [20] Mott, N. F. The basis of the electron theory of metals, with special reference to the transition metals. *Proc. Phys. Soc. A* **62**, 416 (1949).
- [21] Han, Y. & Liu, D. J. Quantum size effects in metal nanofilms: Comparison of an electron-gas model and density functional theory calculations. *Phys. Rev. B* **80**, 155404 (2009).
- [22] Woodruff, D. P. *The chemical physics of solid surface – Surface Alloy and Alloy surface*, vol. 10 (ELSEVIER, 2002).
- [23] Andersson, K. J., Calle-Vallejo, F., Rossmeisl, J. & Chorkendorff, I. Adsorption-driven surface segregation of the less reactive alloy component. *J. Am. Chem. Soc.* **131**, 2404 (2009).
- [24] Ast, C. R. *et al.* Giant spin splitting through surface alloying. *Phys. Rev. Lett.* **98**, 186807 (2007).
- [25] Goodman, D. W. Chemistry on monolayer metallic films. *Ultramicroscopy* **34**, 1 (1990).
- [26] Mathias, S. *et al.* Quantum-well-induced giant spin-orbit splitting. *Phys. Rev. Lett.* **104**, 066802 (2010).
- [27] Bychkov, Y. A. & Rashba, E. I. Properties of a 2D electron gas with lifted spectral degeneracy. *JETP Lett.* **39**, 78 (1984).
- [28] Dil, J. H. *et al.* Rashba-type spin-orbit splitting of quantum well states in ultrathin Pb films. *Phys. Rev. Lett.* **101**, 266802 (2008).
- [29] Geim, A. K. & Novoselov, K. S. The rise of graphene. *Nat. Mater.* **6**, 187 (2007).
- [30] Geim, A. K. Graphene: Status and prospects. *Science* **324**, 1530 (2009).
- [31] McCann, E. & Fal'ko, V. I. Landau level degeneracy and quantum hall effect in a graphite bilayer. *Phys. Rev. Lett.* **96**, 086805 (2006).

- [32] Ohta, T., Bostwick, A., Seller, T., Horn, K. & Rotenberg, E. Controlling the electronic structure of bilayer graphene. *Science* **313**, 1130681 (2006).
- [33] Bostwick, A., Ohta, T., Seller, T., Horn, K. & Rotenberg, E. Quasi particle dynamics in graphene. *Science* **313**, 1130681 (2006).
- [34] Ciraci, S., Baratoff, A. & Batra, I. P. Tip-sample interaction effects in scanning-tunneling and atomic-force microscopy. *Phys. Rev. B* **41**, 2763 (1990).
- [35] Woodruff, D. P. & Delchar, T. A. *Modern techniques of surface science*, vol. 1 (Cambridge University Press, 1994).

## Chapter 2

# X-ray Photoelectron Diffraction

The photoelectron diffraction effect has been observed for the first time in 1970 by K. Siegbahn and coworkers who defined such phenomenon as an “*angular dependence of elastically scattered low energy electrons from various electronic shells in a single crystal*”. They proved the evidence of a crystal structure-related electron intensity modulation and stated that by the “*study of electron interference phenomena in crystals... some new information might be obtained by this technique*” [1]. Only eight years later, X-ray photoelectron diffraction based experiments, aimed at a quantitative study of the surface structures of atomic adsorbates on single crystals, were already independently proposed by Kono, Fadley and Woodruff [2,3]. Nowadays a wide experience has been acquired, both concerning the technical aspects of XPD experiments and the theoretical understanding and simulation of diffraction pattern, as well as accurate interpretation of experimental data [4-6].

XPD provides a direct tool for structure determination, and is particularly suitable for applications on long-rang periodic surfaces like oriented single crystal surfaces, ordered adsorbate layers on single crystals, or thin films. The latter represents a large part of the surface systems that I have investigated by using XPD throughout my research activities. Due to its sensitivity to the local environment, structural XPD analysis can also be performed for small atomic surface complexes and for clusters with the same structure and orientation, but not necessarily periodic. Their size can be very small, down to few nanometers. Clusters of this kind can appear even at the early stage of epitaxial film growth [7].

The first part of this chapter will be devoted to the theoretical description of the XPD process. For the sake of simplicity, the Single Scattering Cluster model with Plane Wave approximation (SSC-PW) will be used in order to easily introduce the fundamental physical quantities involved in XPD. The Multiple Scattering approach, as well as the Spherical Wave approximation (MSC-SW)

will be briefly mentioned. In the second section, I will discuss some of the most relevant experimental aspects and equipment required to perform a XPD measurement. In the final section, I'm going to present the simulation techniques and the algorithms that I have used for the development of an efficient method of XPD data analysis.

## 2.1 Photoelectron diffraction theory

The photoelectron diffraction process basically takes place in a crystal lattice when, once a photoelectron is kicked out from an atom (*emitter*) by excitation with a monochromatic photon beam with energy  $h\nu$ , it undergoes a series of elastic scattering events from all the atoms surrounding the emitter, which are called *scatterers*. Hence, during core level X-ray photoemission measurements, the intensity of the energy-selected photoelectrons at the detector is given by the coherent interference between the directly emitted electrons and all the scattered electrons. Photoemission from core levels is a strategic choice because, unlike the valence band electrons, core level electrons are not directly involved in chemical bonds, but they are localized close to the atomic nuclei. In addition, from the direction in which unscattered electrons are emitted one can trace back to the actual position of the emitter atom. Moreover, the electron Binding Energy (BE) carries the fingerprint of the atomic species and chemical state of the emitter. From scattering theories we know that the localization of the minimum and maximum of a particular interference pattern provides information about the path-length difference between the directly emitted and the scattered electron wave, the scattering amplitude and phases, and the geometrical arrangement of the atoms around the emitter atom. Of course, this is just a simplified picture of XPD, the actual scattering events are much more complicated, as will be described later in this chapter.

### 2.1.1 X-ray Photoelectron Spectroscopy

The physical explanation of the X-ray Photoelectron Spectroscopy (XPS) owes to the Einstein's theory of the photoelectric effect in 1905, in which the interaction between light and matter was first quantitatively derived by the quantization of the electromagnetic radiation. Nowadays, photoemission based experimental techniques have evolved into different branches spanning a wide range of research fields in Solid State Physics [8].

A fundamental relation in photoemission processes is the following energy conservation equation:

$$h\nu = E_B^V + E_K' = E_B^F + E_K + \varphi_{analyzer}. \quad (2.1)$$

Where  $h\nu$  is the incident photon energy,  $E_B^V$  is the electron binding energy relative to the vacuum level, and  $E_K'$  is its kinetic energy immediately outside the sample. Since the final kinetic energy  $E_K$  of the photoelectrons is usually

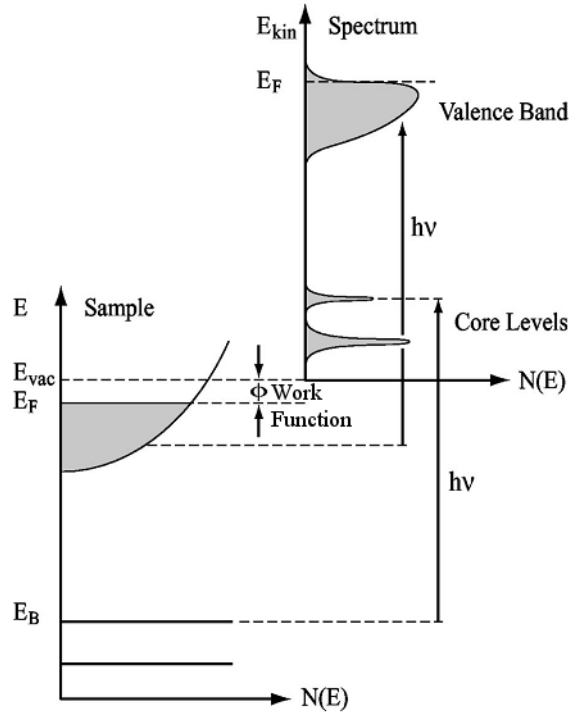


**Figure 2.1:** Energy diagram of the photoemission process.

measured using an electron energy analyzer, the work function of the analyzer,  $\varphi_{analyzer}$ , has to be taken into account. Conventionally the photoelectron binding energy is expressed relative to the Fermi level, hence  $E_B^F$ , so that it is independent of the analyzer work function. In figure 2.1 is shown the relation among all these quantities.

In a simple but very useful description the photoemission process is given by the so-called three-step model. Indeed the whole process can be divided into three phases. i) Penetration of the photon beam underneath the sample surface, followed by the excitation of an atom which emits photoelectrons from a certain core level. The photoemission intensity is proportional to the differential photoelectric cross-section,  $d\sigma_{nlm}(h\nu, \hat{\varepsilon})/d\Omega$ , which depends on the quantum numbers  $nlm$  of the initial state, the radiation polarization  $\hat{\varepsilon}$  and energy  $h\nu$ , and also the experimental geometry. ii) Transport of the photoelectrons from the emitter towards the surface. Here the electron intensity can be attenuated because of electron mean free path related to inelastic scattering events, of the elastic scattering and the diffraction processes such as XPD. iii) Escape from the surface into the vacuum, which involves refraction and reflection at the surface potential barrier, quantitatively expressed by the inner potential  $V_0$ .

### Binding Energy and Photoelectric Cross-section

From the point of view of the interacting electrons in a solid, the photoemission process is a photon-induced transition from a initial  $N$  bound electron state to a final state with  $N-1$  bound electrons and one free electron. If the absorbed photon energy equals to  $h\nu$  and the  $k_{th}$  electron is emitted with kinetic energy  $E_{kin}^k$ , then the whole process can be depicted by the sequence below:

$$\begin{array}{ccc} \text{Initial state} & & \text{Final state} \\ \Psi_i(N), E_i(N) & \xrightarrow{h\nu} & \Psi_f(N-1) + \phi_k(1), E_f(N-1) + E_{kin}^k \end{array}$$

The measured binding energy referred to vacuum level is, in a general many-electron framework,

$$E_B^V(k) = h\nu - E_{kin}^k = E_f(N-1) - E_i(N) \quad (2.2)$$

The evaluation of the exact final ( $N-1$ ) *interacting* electron wave function is a thorny theoretical issue. This is because the final state effects manifest themselves always in a complicated manner and are strongly system-dependent. A quite accurate approximation is given by the Hartree-Fock (HF) method, which represents the  $N$ -electron wave function as a self-consistent single Slater determinant of one-electron *spin-orbitals*  $\phi_k$ . The solution of the HF equations yields to energy eigenvalues of the *spin-orbitals*,  $\epsilon_k$ , also called *orbital-energies* [9]. Actually, the single electron BEs are not  $\epsilon_k$ , but they are  $\epsilon_k$  minus the relaxation energy of the ion state  $\delta E_{relax}$ . However, if we apply the Koopman's Theorem (KT) approximation, the orbital-energies coincide exactly with  $E_B^V(k)$ . KT relies on the assumption that, after the emission of the  $k_{th}$  electron, the spin-orbital wave function of the remaining electrons are unchanged, hence the final state wave function,  $\Psi_f(N-1)$ , is simply the Slater determinant of the initial state spin-orbitals. Then the BE of the photoelectrons in the KT approximations equals to the  $k_{th}$  orbital-energy with opposite sign:

$$E_B^V(k)^{KT} = -\epsilon_k \quad (2.3)$$

A more accurate formalism, aimed at taking into account also the electron-electron interaction, is proposed by the Configuration Interaction (CI) method [9]. In this case the  $N$  electron wave function  $\Psi_i(N)$  is expressed as a linear combination of HF single determinants.

In summary, using the HF Theory and the Koopman theorem, a satisfactory equation for the electron binding energy is given by eq. 2.4, where the contributions of electron-electron correlation  $\delta E_{corr}$  are included. A part from this, the ion relaxation, as well as the relativistic correlation  $\delta E_{relat}$  should be further included [10], thus the total binding energy is:

$$E_B^V(k) = -\epsilon_k - \delta E_{relax} + \delta E_{relat} + \delta E_{corr} \quad (2.4)$$

The photoemission intensity from a core level  $nlm$  from an atomic species  $Q$  can be defined as:

$$I_{Q,nlm} = C \iiint_{\text{all space}} I_{h\nu\rho_Q} \frac{d\sigma_{Q,nlm}(h\nu, \hat{\epsilon})}{d\Omega} \exp\left[\frac{z}{\Lambda_e \sin\theta}\right] \Omega(h\nu, x, y) d\vec{r} \quad (2.5)$$

where  $C$  is a characteristic constant which accounts for the experimental geometry,  $I_{hv}$  is the photon intensity inside the sample,  $\vec{\varepsilon}$  corresponds to the direction of the field polarization,  $\rho_Q$  is density of atoms of type Q and  $\Omega(h\nu, x, y)$  is the *acceptance solid angle* of the spectrometer on the sample surface [8]. The exponential term accounts for the inelastic attenuation, and will be explained later.

The most important term in eq. 2.5 is the differential photoelectric cross-section  $d\sigma_{Q,ntm}(h\nu, \hat{\varepsilon})/d\Omega$ , because it directly determines the intensity of each XPS peak. The photoelectric cross-section is defined as the transition probability per unit time of exciting a solid (or atom/molecule) from an initial to a final state; and is expressed in units of incident photon flux per square  $cm^{-2}s^{-1}$ . Such transition probabilities can be calculated by making use of the *Fermi golden rule* [9]:

$$\frac{d\sigma}{d\Omega} = \frac{2\pi}{\hbar} \sum_{i,f} |\langle N, f | \hat{H}_{int} | N, i \rangle|^2 \delta(E_f - E_i - h\nu) \quad (2.6)$$

where,  $\hat{H}_{int}$  is the photon-electron interaction operator that is introduced in the previous matrix element by using a perturbative approach.

$$\begin{aligned} H_{int} &= -\frac{e}{m} (\vec{A} \cdot \vec{\nabla} + \frac{1}{2} \vec{\nabla} \cdot \vec{A} - \frac{e}{\hbar} |\vec{A}|^2) \\ &\approx -\frac{e}{m} \vec{A} \cdot \vec{\nabla} \end{aligned} \quad (2.7)$$

Here,  $\vec{A}$  is the vector potential of the radiation field,  $\vec{A} = \hat{\varepsilon} A_0 e^{i(\vec{k}' \cdot \vec{r} - \omega t)}$ , where  $\vec{k}'$  is the electron wave vector and is related to the wave length  $\lambda$  by the equation  $|\vec{k}'| = 2\pi/\lambda$ ,  $\omega = 2\pi\nu/\lambda$  is the angular frequency of the e.m. field. The approximation in equation 2.7 is valid for small field strengths, so that  $|A_0|^2$  can be neglected, and, when the typical amplitude of the field oscillation is large with respect to the solid lattice parameters ( $\vec{\nabla} \cdot \vec{A} \cong 0$ ). For any given initial state, moreover, the polarization direction of incoming radiation  $\hat{\varepsilon}$  determines the electron final state on the basis of the symmetry selection rules. If one assumes that the photon wavelength  $\lambda$  is much larger than the common lattice dimensions, so that  $\vec{k}' \cdot \vec{r} \approx 0$ , the exponential term within the definition of  $\vec{A}$  can be put equal to 1, thus yielding  $\vec{A} \cong \hat{\varepsilon} A_0$  (*the dipole approximation*).

Finally, the differential cross-section in equation 2.6 can be cast in the simplified form:

$$\frac{d\sigma}{d\Omega} = \frac{C}{g_i} \sum_{i,f} \left| \langle N, f | \hat{\varepsilon} \cdot \vec{\nabla} | N, i \rangle \right|^2 \rho(E_f^N) \delta(E_f - E_i - h\nu) \quad (2.8)$$

$C$  is a combination of fundamental constants,  $g_i$  accounts for the possible initial state degeneracy,  $\rho(E_f^N)$  includes the final density of state of the whole system. The sum runs over all allowed initial and final states ( $i, j$ ).

Until now, the photoemission process, and in particular the matrix element  $|\langle N, f | \hat{\varepsilon} \cdot \vec{\nabla} | N, i \rangle|$  in eq. 2.8, have been treated by using the total wave functions of all the N electrons both for the initial and the final states. In the weak

electron-coupling limit, the emitted photoelectron can be assumed to undergo a “sudden” transition compared to the relaxation time of the remaining (N-1) electrons, which therefore behave like spectators of the single electron excitation event. This is called “*Sudden Approximation*” and is a successful and simple method for predicting the photoionization cross-section in the weakly-interacting electrons systems. The total wave function results from the antisymmetrized product of the “active” electron spin-orbit and the total wave function of all the “passive” electrons. The matrix element thus becomes:

$$\langle N, f | \sum_{i=1}^N \hat{t}_i | N, i \rangle = \langle \phi_k^f(1) | \hat{t}_k | \phi_k^i(1) \rangle \langle \Psi^f(N-1) | \Psi^i(N-1) \rangle \quad (2.9)$$

where  $\hat{t}$  is the one-electron transition operator, hence the term in left hand side of eq. 2.9 is called one-electron matrix [10].

In a strongly interacting electron system, such as in valence band photoemission, electron relaxation and ion-hole screening effects can become predominant, and transition matrices need to be calculated with a many-body formalism. The final (N-1) electron state is obtained by adding to the non-interacting N electron system a *quasiparticle*, which takes into account the interaction effects. The energy correction to the non-interacting system is expressed by a complex quantity called *Self-Energy*,  $\Sigma$ , that includes the relaxation effects to the adiabatic peak of the photoelectron spectrum. In fact, the real part of  $\Sigma$  correspond to the  $\delta E_{relax}$  term in eq. 2.4, while its imaginary part takes into account the photoelectron finite core-hole lifetime, which is responsible of spectral broadening [11].

When performing a photoemission experiment on a solid, one generally encounters some common initial state and final state effects that should be carefully understood and described. Almost to each of them is associated a parameter designated to include the corresponding effect with a proper mathematical form, for obtaining a most realistic phenomenological and quantitative explanation as possible. These quantities play a fundamental role in XPD and they will be frequently considered case by case. A relevant example of the final state effects will be given in chapter4, in which the complex XPS spectrum of Ni oxide will be discussed. For now, I will provide some general introductory remarks in the paragraphs below.

#### *Electron inelastic scattering and plasmon losses*

The determination of the inelastic mean free path (IMFP)  $\Lambda_e$  of electrons in solids is a key issue in electron spectroscopy and diffraction investigations. The IMFP, in fact, controls the depth sensitivity in a solid sample. This is not purely a intrinsic property of the material, but depends on the kinetic energy and on the experimental geometry. If the inelastic scattering is assumed to be isotropic in the material, then the signal from a given emission depth  $z$  will decay as  $I(z) = I_0 \exp[-z/\Lambda_e \cos \theta]$ , where  $\theta$  is the electron take-off angle with respect

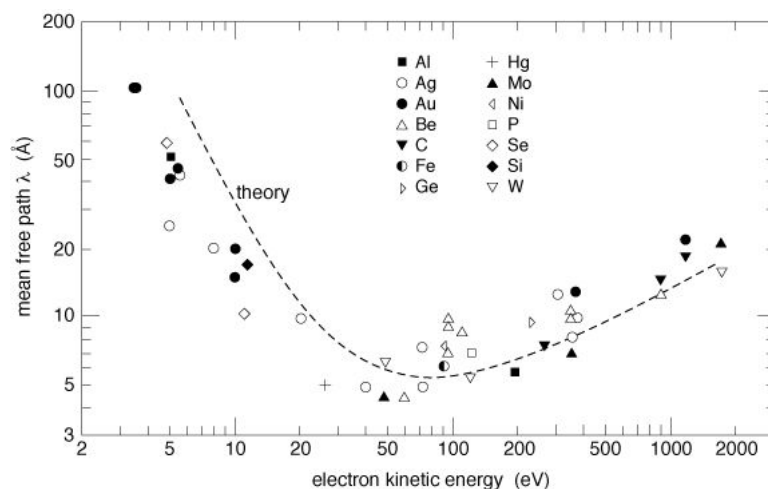


**Figure 2.2:** Universal curve of the electron IMFP as a function of the electron kinetic energy.

to the surface normal, and  $I_0$  the unscattered intensity. However, if elastic scattering and surface escape effects are also included, the effective attenuation length should be considered instead. Figure 2.2 shows the “universal curve” of the IMFP as function of electron kinetic energy for various elements. Notice that the IMFP can be very small for low kinetic energies, and in this regime there is also a strong dependence on the material. Most elements show a common broad minimum at energies of approximately 50–100 eV. Electrons in this energy range show a maximum surface sensitivity (as observed in LEED). At kinetic energies above 150 eV, the IMFP of the electrons becomes large again. In a solid, inelastic scattering contributes to the photoemission spectra, by the electron-hole pair creation, thus forming an inelastic tail on the high binding energy side of the main peak.

Beside the inelastic tail of XPS spectra, in some cases more pronounced energy loss peaks originating from plasmon excitations can be found. This can be a final state effect caused by the photoholes deexcitation, which in turn induces the quantized excitation of the conducting electrons in the solid, in which case we speak of *intrinsic plasmons*. Alternatively, plasmons can be excited by the photoelectrons traveling from the emitter to the surface. These are called *extrinsic plasmons*, because their origin is not an intrinsic effect of photoemission process. In a solid the plasmon states are strongly localized at the surface, in such a way that one can distinguish surface plasmon from bulk plasmon, whose frequencies are related by the equation  $\omega_{surf} = \omega_{bulk}/\sqrt{2}$ . It should be mentioned that plasmons strongly influence the electron IMFP.

#### *Electron refraction at the surface: the inner potential $V_0$*

Another physical effect that is always present during any kind of photoemission experiment is the electron refraction at the solid/vacuum interface. Due to the interaction with the free electron gas, photoelectrons inside the solid

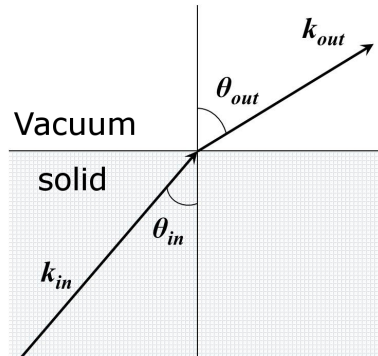


**Figure 2.3:** The inner potential correction.

have higher kinetic energy than in vacuum, and electron energy loss occurring in crossing the surface is due to the *inner potential*  $V_0$ . Hence  $E_{out} = E_{in} - V_0$ , where  $V_0$  is approximately the sum of the valence band width and work function. The energy relevant to the electron scattering is the kinetic energy inside the solid,  $E_{in}$ ; while  $E_{out}$  is the final energy at the detector. For this reason, the inner potential has always to be properly considered. The inner potential barrier at the solid-vacuum interface refracts the photoelectrons in the direction away from the surface normal, so that the measured take-off angle will be a few degrees larger than the actual emission angle. Since the potential step is present only along the direction normal to the surface, the parallel component of the electron momentum is conserved during refraction:  $k_{in} \sin \theta_{in} = k_{out} \sin \theta_{out}$ . The refraction geometry is schematically depicted in fig. 2.3, and the emission angle correction is related to the inner potential as:

$$\theta_{in} = \sin^{-1}\left(\frac{k_{out}}{k_{in}} \cdot \sin \theta_{out}\right), \quad k_{in} = \sqrt{k_{out}^2 + 0.262483V_0}. \quad (2.10)$$

Typically values of  $V_0$  can range from 2 eV to 20 eV, and, they are very sensitive to the surface composition. For example, adsorbates on the sample surface will modify the  $V_0$  of the clean substrate. This happens because the charge rearrangement directly affects the surface potential barrier, and thus the refraction angle. Due to the dependence of the inner potential on the sample composition, it is conventionally treated as an adjustable parameters during an XPD experiment. From eq. 2.10, it is clear to which extent the inner potential can affect the kinetic energy and diffraction angle in angle-resolved photoemission experiment, such as XPD.

#### *Vibrational effects*

Temperature dependent atomic lattice vibrations, or phonon levels, can broaden the XPS components and attenuate the interference patterns in an XPD experiment. The simplest way to include the vibrational effects is multiplying each scattered photoelectron wave function  $\phi_j$  by the Debye-Waller

factor:

$$W_j(T) = \exp \left[ - \Delta k_j^2 \overline{U_j^2}(T) \right] \quad (2.11)$$

where  $\Delta k_j^2$  is the squared magnitude of the wave vector variation caused by scattering, and  $\overline{U_j^2}(T)$  is the temperature-dependent one dimensional mean squared vibrational displacement of the  $j^{\text{th}}$  emitter. In the Debye model, the mean square displacement is calculated in terms of the *Debye temperature*,  $\theta_D$ , as  $\overline{U_j^2}(T) = 9\hbar^2 T / mk_B \theta_D$  [12].

However, in low energy regime or in some specific geometrical configurations, correlated vibrational motions of atoms should be considered instead. In this case the isotropic mean squared vibrational displacement  $\overline{U_j^2}(T)$  is replaced by  $\sigma_j^2(T) = \langle (\Delta \vec{k}_j \cdot u_j)^2 \rangle$ , which is the thermal average of the projection of the atomic displacement of the  $j^{\text{th}}$  emitter,  $u_j$ , onto the direction of the wave vector change  $\Delta \vec{k}_j$ . Its  $\theta_D$  dependence has a much more complicated form as discussed in detail by Kaduwela and Fadley [13].

### Core level chemical shifts

XPS is also known as Electron Spectroscopy for Chemical Analysis (ESCA) which emphasizes the chemical sensitivity of this experimental technique. In fact, Core Level chemical Shifts (CLS), including also Surface Core Level Shift (SCLS), provide a powerful tool for the interpretation of XPS spectra, thus helping in the determination of surface structures and the different chemical bonding mechanisms.

Two components of a XPS spectrum are chemically shifted when they originate from the same core level of the same atomic species, but are found in different chemical environments. While valence band electrons change dramatically their photoemission profile, core level electrons show characteristic binding energy shifts ranging from few meV to several eV [14]. The chemical non-equivalence between atoms of the same element can arise from various surface events, such as the presence of an atomic or molecular adsorbates, phase transitions, coordination heterogeneity etc. In general terms, the chemical shift between two system A and B can be expressed as:

$$\Delta E_B = (E_{ion,A}(N-1) - E_{GS,A}(N)) - (E_{ion,B}(N-1) - E_{GS,B}(N)) \ .$$

$E_{ion,A(B)}(N-1)$  is the final  $(N-1)$  electron state for the two systems, including all possible final state effects, and,  $E_{GS,A(B)}(N)$  is the initial ground state of  $N$  electrons.

Examples of strong chemical shift are described in chapters 3, 4 and 5, where the oxidation of  $d$ -band transition metals is presented. In such metals, the XPS peaks originating from the oxidized atoms are significantly shifted with respect to the clean metal component. In addition, owing to the complex charge transfer interaction effects within metal-ligand field, multiple components can also arise, which reflects environment-specific bonding states.

SCLSs are the binding energy shifts between the bulk component and the surface component(s). The extent of SCLS is generally smaller compared to the

chemical shifts of other kinds. In fact, high resolution XPS measurements are required to achieve a spectral resolution high enough to accurately resolve the shifted components of this type. Now SCLSs can be measured with an energy resolution down to 10–30 meV, thanks to the employment of highly tunable and polarizable third generation Synchrotron Radiation (SR) light sources, combined with high energy resolution and fast acquisition electron detectors. The samples that I have studied by means of core level photoemission mainly concern the transition metal surfaces. In these systems, the origin of the SCLS can be basically explained by the difference in structural environment between atoms of the bulk and of the first few surface layers. Compared to bulk atoms, the atoms located close to the surface have a narrower  $d$ -band, and the center of gravity of the  $d$ -band,  $B_d^{surf}$ , is either lowered or lifted depending on whether the  $d$ -band is more or less than half-filled. Charge redistribution around the Fermi level then creates a surface potential shift,  $\Delta B_d = -(B_d^{surf} - B_d^{bulk})$ , which affects both the surface  $d$ -band and core levels [15,16].  $\Delta B_d$  is often proportional to SCLS.

Chemical shifts is also structural sensitive, in the sense that, different BE-shifted components in the XPS spectrum can be ascribed to atoms in structurally non-equivalent configurations. SCLS measurements, in combination with an accurate *ab initio* calculations, such as Density Functional Theory (DFT), have proved to be a very successful tool for studying the geometry of atomic adsorption on single crystal surfaces [17–19].

### 2.1.2 Photoelectron scattering

So far, an important effect has been neglected in the discussion of the photoemission process: the elastic scattering of photoelectrons from the surrounding atoms along their path to sample surface. This effect is at the base of the XPD technique, and can introduce direction and energy-dependent modulations as large as 50–70% to the overall photoemission signal. In this section the theoretical background used to describe the scattering patterns will be briefly illustrated.

#### Single Scattering Cluster model (SSC)

The most simple and effective model used to describe electron-atom scattering is the Single Scattering Cluster model with the Plane Wave approximation (SSC-PW), proposed by Fadley *et al.* [2,20]. In fig. 2.4 the main physical processes, as well as the most significant parameters involved in Photoelectron Diffraction (PD) are reported.

Given the wave function of the unscattered photoelectron  $\phi_0$ , and that of the *singly scattered* electron from the  $j^{\text{th}}$  scatterer atom,  $\phi_j$ , then the total intensity

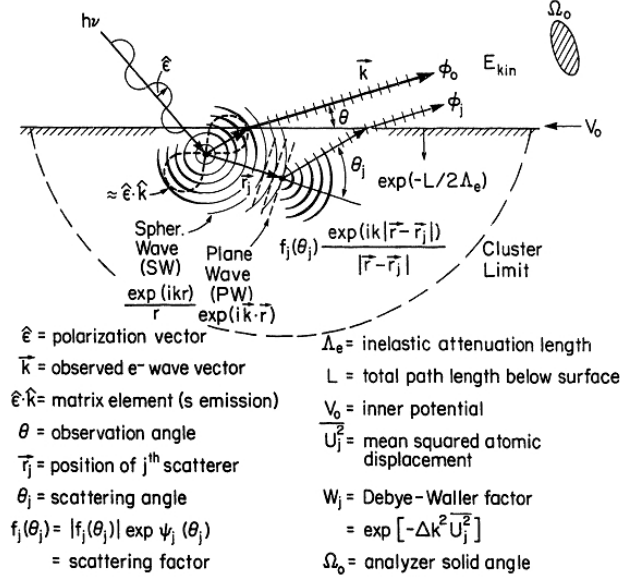


**Figure 2.4:** Schematic drawing of the processes involved in PD and the most significant physical quantities [5].

is proportional to the square of the sum of all final states:

$$\begin{aligned}
 I(\vec{k}) &\propto |\phi_0 + \sum_j \phi_j|^2 \\
 &\propto |\phi_0|^2 + \sum_j (\phi_0^* \phi_j + \phi_0 \phi_j^*) + \sum_j \sum_{j'} \phi_j^* \phi_{j'}
 \end{aligned} \tag{2.12}$$

where the sums  $\sum_j$  and  $\sum_{j'}$  run on all the atoms in a *finite cluster*, i.e. a cluster formed by a *finite* number of scatterers around the emitter. The previous equation can then be rewritten as follows:

$$I(\vec{k}) \propto F_0^2 + 2F_0 \sum_j |F_j(\theta_j)| \cos \left[ \underbrace{k r_j (1 - \cos \theta_j)}_{\text{path length difference}} + \underbrace{\Psi_j(\theta_j, k)}_{\text{scattering phase}} \right]. \tag{2.13}$$

where  $F_0$  is the amplitude of the directly emitted wave,

$$F_0 = I_0^{1/2} = (\hat{\epsilon} \cdot \hat{k}) \exp[-L/2\Lambda_e].$$

$|F_j(\theta_j)|$  represents the effective amplitude of electron wave, whose energy and direction are expressed by the  $\vec{k}$  vector, and that has been scattered by an atom located at  $\vec{r}_j$ ,

$$|F_j(\theta_j)| = (\hat{\epsilon} \cdot \hat{r}_j) \frac{|f_j(\theta_j)|}{r_j} W_j(\theta_j) \exp(-L_j/2\Lambda_e).$$

The cosine function in eq. 2.13 accounts for the total final phase difference between  $\phi_0$  and each  $\phi_j$ , and the labeled parts have important geometrical meaning. Indeed, the *path length difference* is given by the radial distance

between emitter and scatterer, while the *scattering phase* depends on their relative angle. The inelastic attenuation length of the scattered wave,  $\Lambda_e$ , as well as the Debye-Waller factor  $W_j(\theta_j)$  (eq. 2.11), which appear in the two expression above, were already mentioned before. The amplitude  $|F_j(\theta_j)|$  is defined through the electron-atom scattering factor  $f_j(\theta_j)$ , which can be calculated from the partial-wave phase shifts  $\delta_l$ , according to the following equation for plane wave scattering:

$$f_j^{PW}(\theta_j) = \frac{1}{k} \sum_{l=0}^{l_{max}} (2l+1) e^{i\delta_l} \sin \delta_l P_l(\cos \theta_j)$$

where  $l_{max}$  is the highest order of the partial-wave expansion and  $P_l(\cos \theta_j)$  are Legendre polynomials. In the plane wave approximation, the scattered wave  $\phi_j$  can always be written as a spherical wave multiplied by the electron-atom scattering factor  $f_j(\theta_j)$ :

$$\phi_j(k, \theta_j) = f_j(\theta_j) \frac{\exp(ik|\vec{r} - \vec{r}_j|)}{|\vec{r} - \vec{r}_j|}$$

with a total phase shift of  $[kr_j(1 - \cos \theta_j) + \Psi_j(\theta_j)]$ .

In addition, flux conservation imposes that the part of  $\phi_0$  which undergoes a scattering event from the  $j^{th}$  atom thus generating  $\phi_j$ , decays in amplitude like a propagating spherical wave. Also the amplitude of  $\phi_j$ , which is denoted by  $|F_j(\theta_j)|$ , has an  $1/r$  behavior, where  $r$  denotes the distance from the emitting atom. The  $1/r$  dependence of the wave function amplitude on the distance of propagation is the main reason why PD is a *short-range local structure probe*. Indeed the environment of the nearest neighbor of the emitter is the dominant structural factor that determines the final PD pattern. These considerations justify the use of the *cluster model* formed by a limited number of atoms, which is widely used in XPD calculations.

The overall photoelectron signal results from the incoherent summation of the contributions from all the significant emitter atoms. The phase factor and the path length difference in eq. 2.13 are fundamental parameters that are responsible of an oscillating behavior to the measured interference pattern. For example, fig. 2.5 schematically illustrates the interference pattern generated from the superposition of two spherical waves originating from an emitter and a Cu scatterer atom. For simplicity, the phase shift is equal to zero. Note that several scattering orders comes out, and the direct and the scattered waves are coherent. As a consequence, an XPD analysis for polycrystalline or amorphous structures is impossible, because the complete lack of a geometrical order of the emitter's nearest neighbors will produce randomly scattered waves without any spatial or phase coherency.

It is clear from the definition of the PD intensity in eq. 2.13 that  $I(\vec{k})$  depends both on the photoelectron kinetic energy and on the local geometry. Experimentally, there are two acquisition mode for collecting PD patterns: angle-scanned PD and energy-scanned PD. The first measures the intensity modulation while rotating the sample, and the second one while changing the kinetic energy (or

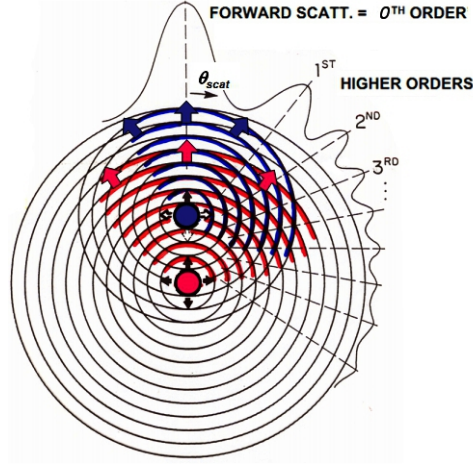


**Figure 2.5:** Diffraction orders and interference patterns originated by spherical waves from an emitter (red) and a scatterer (blue) of Cu, in high kinetic energy regime [13].

excitation energy). In both cases, the most straightforward way to derive this modulation from the raw experimental data is to calculate the *modulation function*  $\chi(|\vec{k}|, \vartheta_e, \varphi_e)$  as a function of the kinetic energy ( $|\vec{k}|$ ) or of the emission angle ( $\vartheta_e, \varphi_e$ ):

$$\chi(|\vec{k}|, \vartheta_e, \varphi_e) = \frac{I(|\vec{k}|, \vartheta_e, \varphi_e) - I_0}{I_0} \quad \text{then,} \quad (2.14)$$

$$\chi(|\vec{k}|, \vartheta_e, \varphi_e) \propto \sum_j |F_j(\theta_j)| \cos [kr_j(1 - \cos \theta_j) + \Psi_j(\theta_j, k)] . \quad (2.15)$$

Calculations have shown that, for small scattering angles, the scattering phase shift  $\Psi_j(\theta_j)$  is small for common elements, while the amplitude of the scattering factor  $|f(\theta)|$  shows a single maximum in the forward direction, particularly when the electron kinetic energy is above  $\sim 300$  eV [4]. The combination of these two peculiar effects gives rise to the **forward scattering/focusing** effect. A large intensity enhancement is observable, due to the scattering events from an atom placed in front of the emitter along the path of the photoelectron to the detector. The most intense features of an experimental pattern usually arise from forward scattering events. When the electron kinetic energy is lower than  $\sim 300$  eV, then **backward scattering** can become the predominant process. In this case, photoelectrons are also elastically scattered by atoms behind the emitter. Experimentally, when working in the forward focusing geometry, i.e. at polar angle  $\cong 0^\circ$ , no path length difference builds up between the emitted and the scattered waves, so that the interference is constructive in this direction. On the contrary, if the PD intensity is measured at a larger polar angle, a path length is geometrically introduced, leading to either constructive or destructive interference phenomena at larger polar angles. Fig. 2.6a shows  $|f(\theta)|$  as a function of the polar angle for Ni and O atoms at different electron kinetic energies. This result clearly indicates that, by increasing the electron energy, a

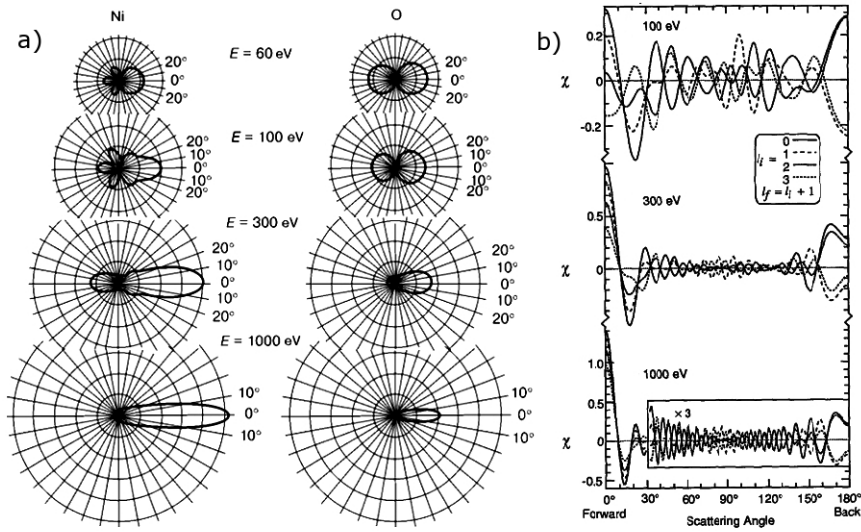


**Figure 2.6:** a) Angular distribution of the electron scattering amplitude  $|f(\theta)|$  on Ni and O atoms for electron energies of 60-1000 eV. The scattering angle of  $0^\circ$  ( $180^\circ$ ) corresponds to the forward (backward) direction [21]. b) Calculated modulation functions  $\chi(\theta)$  from a Cu atom for different various of angular momentum and at different energies [4].

strong raise in intensity shows up along the forward direction ( $\theta \cong 0^\circ$ ) for both species, while backward contributions ( $\theta \cong 180^\circ$ ) disappear.

The same forward enhancement and backward suppression at higher energy emerge also from the plot of  $\chi(\theta)$  reported in fig. 2.6b. This graph proves how the goodness of the forward scattering approximation in the high energy regime is further supported by the fact that, changes in the final state angular momenta  $l_i$  affect only marginally the modulation functions. This is the reason why forward scattering phenomena at KEs higher than  $\sim 500$  eV can always be described, with high enough accuracy, by the plane-wave single scattering approximation.

In a XPD pattern, forward focused features have the great advantage of conveying direct qualitative structural information about the system under investigation. This owes to the fact that the direction at which forward scattering is observed corresponds to the bonding direction between emitter and scatterer; therefore, it offers a simple way to identify the intra-atomic or intra-molecular bond directions inside a solid. In many cases the determination of molecular orientation, as well as the bonding directions, is straightforward. In fact, the position of the intensity maxima allows a straightforward determination of the bond angles relative to the crystal lattice directions, and also the symmetry of the sample surface can be directly derived from the diffraction pattern. However, the forward scattering mode allows to focus only on zero-order diffraction (i.e. events in which the scattering path length difference between the scatterer and emitter is zero); thus losing quantitative information contained in the actual

interference mechanism, generated by the superposition of electron waves with different phase or amplitudes (owing to the path length differences). In order to get a detailed quantitative description of a certain structure, back-scattering effects corresponding to higher order diffraction features have to be included as well. In fact, backward scattered electrons carry more detailed information on the local atomic arrangement, due to phase shifts and amplitude variations of their wave functions induced by path length differences. The analysis of these diffraction features will yield structural details such as inter-atomic distances, bond lengths and inter-layer spacing etc.

In synthesis, the actual XPD pattern results from an interplay between both forward and backward scattering processes, thus making XPD technique a very powerful tool for the investigations of complex local geometries.

### Multiple Scattering Cluster model and Spherical Wave approximation (MSC-SW)

The plane wave approximation is an instructive method for the qualitative description of the most relevant phenomena involved in XPD, but the limitations of this approach in interpreting experimental data are well known, specially at low kinetic energy conditions [22]. Note in fig. 2.6b that the behavior of the  $\chi$  functions on varying the angular momentum  $l_i$  is dramatically different at low kinetic energy (see the top graph). An accurate representation of both the initial and final states of the photoelectron is required in order to carry out a thorough XPD analysis. Therefore, a number of realistic quantum mechanical models have been developed to describe photoelectron diffraction by using a basis set of spherical waves in a multiple-scattering framework. This is the so-called Multi-Scattering Cluster mode with Spherical Wave approximation (MSC-SW). One of the most popular formalism is the *separable Green's function matrix* method, developed by Rehr and Albers (hence RA matrices) [23] and implemented by Friedman *et al.* for photoelectron diffraction calculations [4]. The advantage of the RA-formalism is its ability to provide simple, accurate and computationally fast spherical wave calculations for arbitrary initial states with any  $l_i$ . A detailed mathematical derivation of this formalism is reported in Ref.s [4,24]; in this thesis I will just give a general scheme of this method.

In the many-body framework, wavefunctions are conventionally treated with perturbation theory by introducing a *free electron propagator*, which can be expressed as follows. First of all, let's consider the one-electron Schrödinger equation for a particle subjected to an interaction (or scattering) potential  $V(\vec{r})$ :

$$\left[ -\frac{\hbar^2}{2m}\nabla^2 + V(\vec{r}) \right] \psi(\vec{r}) = E \psi(\vec{r}). \quad (2.16)$$

In the absence of interactions (i.e. in the free-electron approximation), the solution of this equation would be a spherical wave of the form:

$$G(\vec{r}, \vec{r}') = -\frac{m}{2\pi\hbar^2} \frac{\exp(ik_0|\vec{r} - \vec{r}'|)}{|\vec{r} - \vec{r}'|}. \quad (2.17)$$

This spherical wave is also called *Green's function of the free propagator*, and it describes how a free electron, originating from  $\vec{r}'$ , propagates to  $\vec{r}$ . This function satisfies the previous Schrödinger equation everywhere except at  $\vec{r}'$ . Therefore, an alternative definition of the Green's function is given by the solution of the following equation [25]:

$$\left[ E + \frac{\hbar^2}{2m} \nabla^2 \right] G(\vec{r}, \vec{r}') = \delta(\vec{r} - \vec{r}') . \quad (2.18)$$

Then by using the property of the Delta function, it can be proved that an integral form of the solution of the interacting Schrödinger equation can be written by using the Green's function as:

$$\psi(\vec{r}) = \psi_0(\vec{r}) + \int G(\vec{r}, \vec{r}') V(\vec{r}') \psi(\vec{r}') d\vec{r}' . \quad (2.19)$$

where  $\psi_0(\vec{r})$  and  $\psi(\vec{r})$  are the initial and final states measured at  $\vec{r}$  respectively. The latter integral equation leads to a simple physical interpretation of the perturbative approach to the scattering process for interacting electrons. It expresses the final wave as the sum of the incident wave  $\psi_0(\vec{r})$  and the scattered wave (the second term on the right end side), similarly to the definition in eq. 2.12. The solution of the interacting Schrödinger equation  $\psi(\vec{r})$  is given by the superposition between the incident plane wave  $\psi_0(\vec{r})$  and the spherical waves emitted from scattering occurred at position  $\vec{r}'$ . The amplitude of these spherical waves is proportional to the interaction potential  $V(\vec{r}')$  and to the amplitude of the electron wave propagated to  $\vec{r}'$ .

Such a final state wave function is not yet a solution of the Schrödinger equation, because  $\psi(\vec{r}')$  appears at both sides of eq. 2.19. However, if the interaction potential is assumed to be so weak that the amplitude of the scattered wave is lower than the incident wave, then  $V(\vec{r}')$  can be treated perturbatively by replacing  $\psi(\vec{r}')$  with  $\psi_0(\vec{r}')$  as follows:

$$\psi(\vec{r}) = \psi_0(\vec{r}) + \int G(\vec{r}, \vec{r}') V(\vec{r}') \psi_0(\vec{r}') d\vec{r}' . \quad (2.20)$$

Equation 2.20 is the so-called first Born approximation [25].

Now let's go back to the general N interacting electron case, where a propagating electron emitted at  $\vec{R}_0$  can be subjected to scattering events from all the other (N-1) electrons. In this case, a total propagator,  $\mathbf{G}_{00, L_f}^{(N-1)}$ , that includes the  $(N-1)^{th}$ -order scattering processes should be used. The free electron, that is collected at the detector located at an infinite distance, is conventionally labeled as (00)-state.

Within the RA-formalism, the differential photoelectron cross-section (which is proportional to the intensity) can be written as:

$$\frac{d\sigma}{d\Omega} \propto \left| \sum_{L_f, N} \mathbf{G}_{00, L_f}^{(N-1)}(\vec{R}_1, \vec{R}_2, \dots, \vec{R}_N) m_{L_f, c}(\hat{\varepsilon}) e^{i\delta_{L_f}^c} \right|^2 \quad (2.21)$$

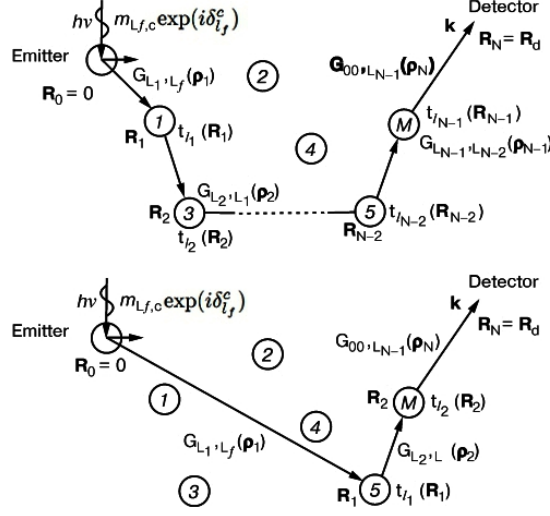


**Figure 2.7:** Diagram of an electron traveling from  $\vec{R}_0$  to  $\vec{R}_d$ . The circles are atoms and the arrows indicate the electron path direction. Top  $(N-1)^{th}$  order scattering propagator  $\mathbf{G}_{00, L_f}^{(N-1)}$ ; bottom, second order scattering propagator  $\mathbf{G}_{00, L_f}^2$  [13].

where  $\vec{R}_0$  is the position of the emitter and  $\{\vec{R}_1, \dots, \vec{R}_{(N-1)}\}$  are the positions of the scatterers. The detector is placed at infinite distance  $\vec{R}_N = \vec{R}_{\text{detector}} = \infty$ , and  $m_{L_f, c}$  and  $e^{i\delta_{l_f}^c}$  represent the amplitude and phase of the core-to-continuum transition dipole matrix element  $\langle \Psi_{E_{kin}, \vec{k}} | \hat{\epsilon} \cdot \vec{r} | \phi_{n_i, l_i, m_i} \rangle$ , from an initial state  $(n_i, l_i, m_i)$  to a final state  $L_f = (l_f, m_f)$ . The sum extends to all possible final states  $L_f$  and to all combinations of  $N$ , which is the number of atoms for a given scattering path. For example,  $N=2$  corresponds to a single scattering event (one atom is the emitter, the other is the scatterer).

Rehr and Albers elaborated a *convergent and separable* representation for the calculation of the matrix elements of the free propagator in eq. 2.17. In this formulation, the total propagator of the  $N$  electron system (so  $(N-1)$  scatterers),  $\mathbf{G}_{00, L_f}^{(N-1)}$ , can be expressed in terms of the *t scattering matrices*,  $t_{l_j}$ , and of the matrix elements of the free propagator  $G_{L, L'}(\vec{\rho})$ :

$$\begin{aligned} G_{L, L'}(\vec{\rho}) &= \langle L, \vec{R} | G | L', \vec{R}' \rangle, & L &= (l, m) \\ t_{l_j} &= \exp(i\delta_{l_j}^c) \sin \delta_{l_j}, & (j &= 1, \dots, N) \\ \vec{\rho} &= k(\vec{R} - \vec{R}') \end{aligned}$$

The new parameter  $\vec{\rho}$  is the so-called *bond vector*, and Rehr and Albers demonstrated that, when expressed as a function of the bond vector,  $G_{L, L'}$  can be written as separable sum of products [23]. Thus the total multiple scattering propagator can be written as:

$$\begin{aligned} \mathbf{G}_{00, L_f}^{(N-1)}(\vec{R}_1, \dots, \vec{R}_N) &= \sum_{\text{paths}} \sum_{L_i} G_{00, L_f}(\vec{\rho}_N) t_{l_{N-1}}(\vec{R}_{N-1}) \times \\ &\times G_{L_{N-1}, L_{N-2}}(\vec{\rho}_{N-1}) t_{l_{N-2}} \times \dots \times t_{l_1}(\vec{R}_1) G_{L_1, L_f} \end{aligned} \quad (2.22)$$

The total scattering path is separated into a sum of products, each one represents a single scattering event of the whole process, and depends only on one pair of atoms at a time. Fig. 2.7 reports a diagram representing the RA description of the multiple scattering process of  $(N - 1)^{th}$  order (top) and of the second order (bottom) occurring from  $\vec{R}_0$  to  $\vec{R}_{detector}$ . The summation runs over all possible paths and all allowed initial states  $L_i$ . This result permits, on one hand, to calculate scattering results of an order as high as the number of the atoms inside the cluster, and on the other hand to account for photoemission processes from all core levels in the spherical wave approximation.

Strictly speaking, the RA formalism has the general purpose of predicting the photoemission intensities associated to multiple scattering events and it has been successfully applied to the photoelectron diffraction case by Friedman and Fadley. Further details can be found in ref. [4]. Substituting the eq. 2.22 into eq. 2.21 one obtains the final expression for the RA approximated photoemission cross-section and intensity. By choosing a high enough degree of accuracy, that means suitably selecting the highest order of scattering, the dimension of the RA matrix and the cluster size, reliable results can be achieved by means of RA calculations for multiple scattering photoelectron diffraction [26].

## 2.2 Experimental setup

In this section I will describe the most important equipments that I have used for performing the angle-scanned X-ray photoelectron diffraction experiments. Sample preparation procedures and related techniques will be discussed in the first place. Radiation sources used for core electron excitation will be then briefly presented. Finally, the electron energy analyzer used to collect and to analyze the photoelectrons, and different multiple degree of freedom manipulators at each experimental stations will be also shown.

### 2.2.1 Sample preparation

X-ray photoelectron diffraction is an extremely demanding structural detection technique that requires particular experimental conditions and a dedicated instrumentation. First of all, like all photoemission-based techniques, XPD must be performed in Ultra-High Vacuum (UHV) environment. Therefore, during the measurements, our experimental chambers are always kept at a base pressure of the order of  $10^{-10}$  mbar. One reason is the small IMFP of low energy photoelectrons, as already discussed in section 2.1.1. The higher the residual gas pressure (typically  $H_2$ ,  $CO$ ,  $CO_2$  and  $H_2O$  molecules and ions produced by molecular cracking) is, the larger is the inelastic and undesired elastic scattering probability of the electrons traveling from the sample to the detector, leading to a dramatic signal attenuation. Most importantly, UHV is needed to maintain a good quality of the sample surface after its preparation. For example, a large amount of  $CO$  can induce the degradation of most of the ultra-thin oxide film that I have investigated, by the oxidation of the impinging  $CO$  molecules on

the sample surface. Moreover, adsorbate-free sample surface is needed prior to the deposition of epitaxial films, as the ones presented in the following chapters. The dependence of the surface contamination rate on the pressure is quantified by the Hertz-Knudsen formula:

$$\Phi = \frac{P}{\sqrt{2mk_B T}}.$$

where  $P$  is the pressure,  $m$  is the molecular mass,  $k_B$  is the Boltzmann constant and  $T$  is the sample temperature. Assuming the sticking probability of a certain molecule equals to 1, at a partial pressure of  $10^{-6}$  mbar the calculated time for reaching 1 ML adsorbed molecules on the surface is just few seconds. Therefore, in order to keep the sample surface clean for hours, a pressure better than  $10^{-9}$  mbar ( $t \cong 1.5$  hours if the sticking probability equals to 1) is necessary. UHV experimental systems generally have pressures down to  $10^{-10} \div 10^{-11}$  mbar, where residual gas contaminations are below the detection limit.

Almost in all the experimental stations (which will be described later), the UHV chambers are equipped with differential pumping systems, typically including diaphragm pumps and scroll pumps for the  $10^3$ – $10^{-3}$  mbar pressure range, turbomolecular pumps for pressures down to  $10^{-4}$ – $10^{-10}$  mbar, and ion pumps that allow pressures lower than  $10^{-9} \div 10^{-10}$  mbar. An efficient pumping systems is always accompanied by a bake-out treatment, which consists in heating the chamber and the UHV-compatible instrumentations to temperatures higher than the evaporation temperature of water (approximately  $150^\circ$ – $250^\circ$ ). Since  $\text{H}_2\text{O}$  molecules easily sticks to the chamber walls and are hard to remove, baking stimulates the desorption of the water molecules and their removal with the pumping system.

A fairly clean surface is the starting point for a good sample preparation. Our TM single crystal samples are prepared by undergoing the noble gas ion sputtering process, followed by annealing. Ion bombardment sputters the sample surface thus uncovering the buried contaminants. Annealing then can promote surface segregation of such contaminants and their subsequent desorption. At the same time, annealing favors the sample surface reordering. Sputter ion guns are used for the ion bombardment, which ionizes and accelerates the noble gases particles (we used  $\text{Ar}^+$ ) towards the sample surface. Then the sputtered sample can be heated by resistive irradiation or by electron bombardment. The latter consists in exposing the sample to the thermoionic emission from a couple of wires below the sample. Fig. 2.8 shows the homemade sample holder that we have used in Surface Science Laboratory (SSL) (Elettra and SSR group of CNR-IOM TASC Laboratory). In this picture, the W filaments used for sample annealing and the K-type thermocouple wires for temperature control are visible. The sample is mounted in such a way that it can be grounded, and it is placed very close to the W filaments in order to increase the heating efficiency. By introducing a bias between the sample and the filaments, the emitted electrons are accelerated towards the sample and can heat up the sample within few seconds. Using this sample holder, temperature much higher than  $1000^\circ\text{C}$  can easily be reached. Finally, the surface cleanliness and crystal ordering were

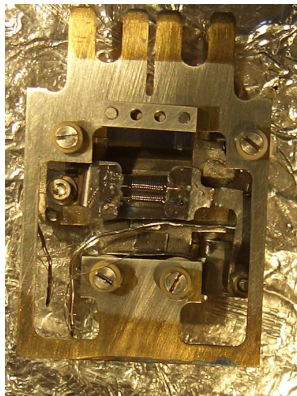


**Figure 2.8:** The homemade sample holder used for electron bombardment heating: in the center there are two W filaments connected to an external power supply; on the lower-left side are visible the junctions for the K-type thermocouple (Chromel-Alumel) for measuring the sample temperature.

checked by using LEED. XPS spectra then gave indications of possible traces of residual contaminants.

### 2.2.2 X-ray excitation sources

In the Surface Science Laboratory, where I have spend most of time during my PhD, two conventional X-ray sources are utilized: a monochromatic Al ( $h\nu = 1486.6$  eV) source and a non monochromatized Mg source ( $h\nu = 1253.6$  eV). A standard X-ray tube consists of a heated cathode filament from which electrons are accelerated towards a water-cooled anode (Al or Mg) held at a large potential difference (13–15 kV) relative to the filament (see fig. 2.9b). The core-holes formed in the inner electron shells of the atoms of the anode material after electron bombardment are radiatively filled by electronic transitions from higher energy levels. These deexcitation process results in the characteristic X-ray emission from the anodes. The X-ray spectra of both the Al and Mg-type sources are dominated by a very intense and unresolved  $K_{\alpha_1}$ - $K_{\alpha_2}$  doublet resulting from  $2p_{3/2} \rightarrow 1s$  and  $2p_{1/2} \rightarrow 1s$  transitions, respectively. In fig. 2.9a is presented the X-ray emission spectrum of the Mg metal, and the most intense lines on the left corresponds to the Mg  $K_{\alpha_{1,2}}$  lines. The horizontal axis indicates the relative energies to the  $K_{\alpha_1}$ - $K_{\alpha_2}$  main line and the intensities on the vertical axis are in logarithmic scale. Some satellite lines are also present due to double ( $KL$ ) and triple ( $KL^2$ ) ionization events. In fact, photoemission spectra from non-monochromatized Al or Mg sources always exhibit also the 10 eV-shifted peaks associated to the  $\alpha_3, \alpha_4$  satellites, which are the most intense ones after  $K_{\alpha_{1,2}}$  lines. In addition, there is a continuous background called “Bremsstrahlung”, which extends up to the energy of incident electron, and adds only a contribution to the background noise, thus lowering the quality of the emitted X-ray radiation. The satellite lines and the “Bremsstrahlung” can be eliminated by using a monochromator which exploits the Bragg diffraction of

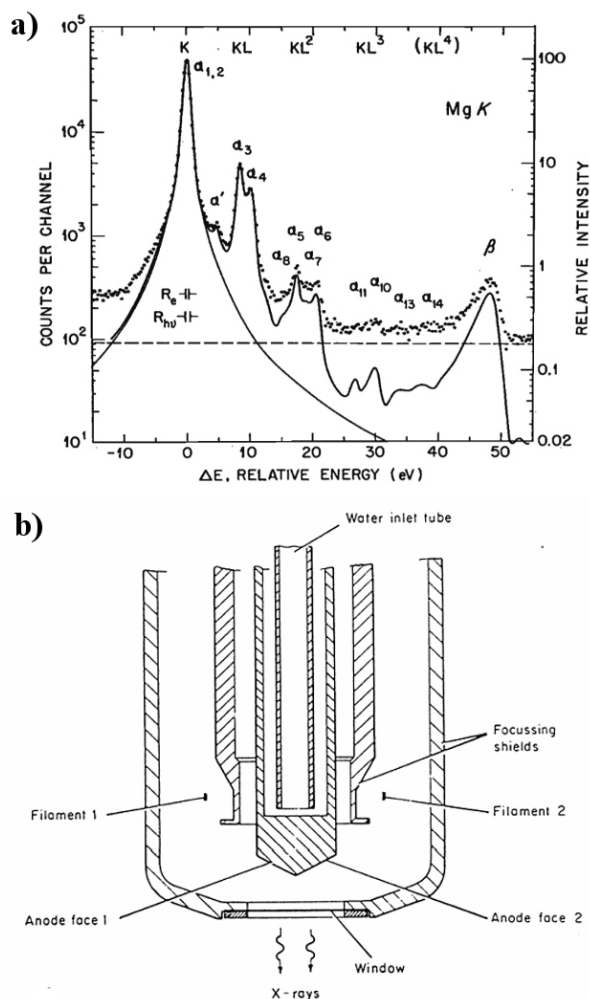


**Figure 2.9:** a) X-ray emission spectrum from metallic Mg. The peaks are associated to the different transitions to the  $K = 1s$  subshell: main line  $K\alpha_{1,2}$  and all the other satellites [10]. b) A schematic representation of the twin-anode X-ray tube present at the SSL.

the photon beam at a crystal grating in combination with a system of reflecting mirrors to monochromatize and focus the outgoing radiation. The commonly used dispersing gratings are made of quartz, because it can be grounded and elastically bent (if thin enough), and it can also resist to the bake-out process without deformations.

In our XPD measurements performed at SSL by using the conventional X-ray source, the photoelectron kinetic energy is typically high enough to allow working in forward scattering regime. As discussed before, forward focused features permit a direct insight into the surface symmetry and bond orientations. Besides the forward scattering enhancement, also the electron IMFP increases with the kinetic energy, and, depending on the photoemission geometry, a max-

imum bulk sensitivity is obtainable as well. A sampling depth up to 10 ML is particularly useful to study bulk properties, thick epitaxial layers and the buried interface interactions.

Higher quality X-ray radiation is provided by the large scale Synchrotron radiation facilities, like Elettra, which is called the synchrotron radiation. Here, bunches of relativistic electrons orbiting inside the storage ring are accelerated through *bending magnets* or insertion devices like *wigglers* and *undulators*, and produce a high brilliance and high flux photon beam. The highest spectral brightness and narrowest beam energy dispersion is attained in undulators, which consist of periodic array of dipole magnets which force the electrons to wiggle and thus to emit coherent light. Besides the high intensity, energy tunability is one of the most important advantages of synchrotron light compared to the light produced by the conventional X-ray source. In fact, a wide energy range (from the IR to the Hard X-ray region, depending on the energy of the electron bunch) can be spanned by changing the undulator gaps between the arrays.

The continuum energy spectrum of the synchrotron radiation gave us the possibility to choose the best photon energy to maximize the photoionization cross-section from a particular core level. In this way, the time required to XPD acquisition was significantly reduced thanks to the higher photoemission signal. Moreover, selecting a low excitation energy enhances the diffracted signal of low kinetic energy electrons, hence the backward scattering regime is always available. The extremely high photon flux with respect to the radiation generated by an X-ray tube, allows to perform photoemission from low density atomic species, such as molecular and atomic adsorbates. In addition, the energy-scanned PD can be carried out only by using synchrotron radiation as the excitation source. Certainly, the combination of conventional sources and synchrotron radiation in XPD is the best method to obtain as much complete structural information as possible.

### 2.2.3 Electron energy analyzer

Once photoelectrons have left the sample surface, they are collected by an electron energy analyzer according to their kinetic energies, and, sent to a detector. The electron energy analyzer that I have used to collect the photoemission signal is the hemispherical analyzer. It is composed by two concentric  $\mu$ -metal shielded hemispheres with different radii, as shown in fig. 2.10. A potential difference,  $V_2 - V_1$ , is applied between the inner hemisphere (or radius  $R_1$ ) and the outer one (or radius  $R_2$ ). The electrons coming from the entrance slit travel between the hemispheric electrodes following specific trajectories determined by their kinetic energies. Therefore the electrons are dispersed along the exit slit and the distances from the center of the exit slit can be converted into energy differences. In particular, electrons closer to the outer hemisphere have higher kinetic energies, whereas the ones with smaller energies are shifted towards the inner electrode. The energy distribution of a photoelectron signal, is determined by the number of electrons at each selected kinetic energy within a certain in-

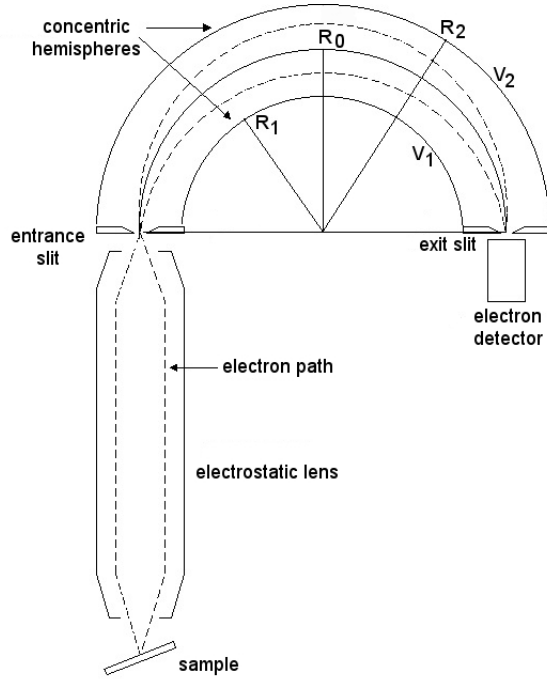


**Figure 2.10:** Schematic plot of the hemispherical electron energy analyzer.

terval. The energy range is chosen by applying the correct potential difference to the hemispheres. In order to force an incoming electron with kinetic energy  $E_0$ , to reach the exit slit following a circular path with radius  $R_0 = (R_1 + R_2)/2$ , the proper potential difference to be utilized must satisfy the equation below.

$$V_2 - V_1 = V_0 \left( \frac{R_2}{R_1} - \frac{R_1}{R_2} \right) \quad (2.23)$$

where  $V_0 = E_0/e$ , and the electron energy  $E_0$  is called *pass energy*. The incoming electrons are focused and decelerated to an energy  $E_0$  by a retarding section, which generally consists of a series of *electrostatic lenses* placed before the entrance slit.

However, eq. 2.23 describes an ideal case, which ignores some experimental limits that contribute to the final energy resolution of the analyzer. Actually, the full width at half maximum (FWHM) of the experimental energy distribution is given by:

$$\text{FWHM} = E_0 \left( \frac{w}{2R_0} + \frac{\alpha^2}{4} \right). \quad (2.24)$$

The average width of the entrance and exit slits,  $w$ , the half-angle of the electrons entering in the analyzer,  $\alpha$ , and the average radius  $R_0$ , should be considered in order to estimate the actual energy resolution [27]. The most important consequence of eq. 2.24 is the linear dependence of the energy resolution of the analyzer on the pass energy. Since it is preferable to keep a constant resolution

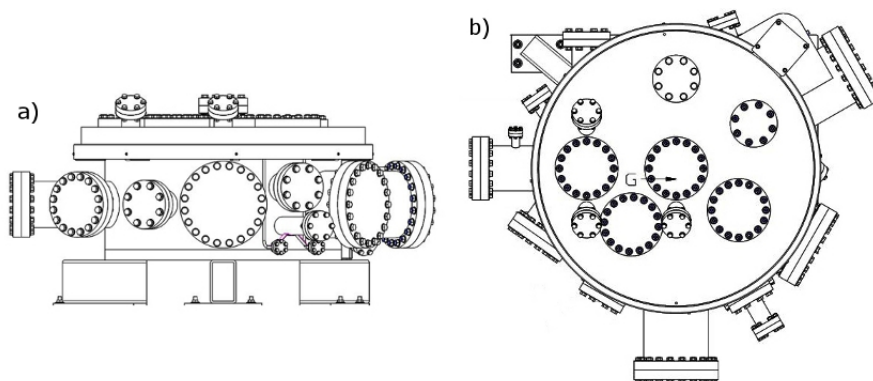


**Figure 2.11:** Side (a) and top (b) view of the main UHV chamber of Surface Science Laboratory.

during an energy scan, the best choice is to fix  $E_0$ , and select the kinetic energy by applying a proper retardation potential with the last element of the lenses. Generally, to achieve the best experimental resolution, one has to choose the lowest possible pass energy that allows retaining an acceptable fraction of the signal at the entrance. This is because the lower the pass energy, the fewer electrons are allowed to enter the analyzer; on the other hand, if the total electron yield is too small, statistical noise become predominant in the final photoemission spectra, thus making the subsequent spectral deconvolution more difficult.

#### 2.2.4 Experimental stations

The availability of dedicated experimental stations is, of course, a determinant ingredient for the realization of any XPD measurement. Setting up a custom system always requires a lot of hard work. In the three years of my PhD, I have mainly worked in the SSL; but I have also had the opportunity of working at two beamlines at Elettra, the third generation synchrotron facility situated near Trieste. They were the SuperESCA beamline and the VUV photoemission beamline. In this section, I will briefly describe the main characteristics of each of the three experimental chambers.

##### The Surface Science Laboratory at Elettra

The Surface Science laboratory is equipped with a multipurpose experimental station devoted to different surface science techniques including XPS, XPD, LEED and LEED-*IV*, Thermal desorption spectroscopy (TDS).

In fig. 2.11 are visible the side (a) and the top (b) view of the main chamber. Different instruments for sample preparation and data acquisition are radially mounted inside the chamber through a series of flanges along the perimeter of the chamber. A large rotating flange covers the top of the chamber, and the

manipulator is placed in a position along the normal to the flange, but out of the rotation axis. This geometry is very convenient since it permits to move the manipulator, and the sample holder, in front of various instruments which instead are fixed.

UHV conditions are obtained by means of a differential pumping system consisting of turbomolecular pumps, an ion pump and a titanium sublimation pump. Inside the main chamber, measurements are normally performed with a residual background pressure of  $10^{-10}$  mbar. The chamber is equipped with two conventional X-ray source, a monochromatic Al- $K_{\alpha}$  and a twin-anode Mg- $K_{\alpha}$  source, a quadrupole mass spectrometer for TDS measurements, a LEED apparatus, a 150 mm mean radius hemispherical analyzer, a quartz microbalance, a sputter ion gun for sample preparation and a magnetic sample transfer line with a fast entry lock. In addition, a gas line and a doser allows the controlled deposition of molecular ad-species during surface reactivity experiments, as well as the preparation of metal clusters or thin films.

The XPD-devoted VG Omniax manipulator, specifically designed for XPD studies, has five degree of freedom, namely three translational motions and two angular rotations, and is remote-controlled by a homemade LabView software. Also the flange rotation is computer-controlled, so that the sample can always be positioned in a precise and reproducible way in front of each instrument. The accuracy of the sample position has a determinant role for angle-resolved XPD measurement; as a matter of fact, the alignment between the axis of rotation of the sample and the focus of the analyzer and the incident excitation light (or focus of the monochromator) depends on a correct positioning of the sample holder. Even a small misalignment among these three axes can introduce artefacts in XPD patterns, e.g. a precession of diffraction spots and a electron signal loss during sample rotation. This manipulator allows sample cooling with liquid nitrogen, and usually the sample temperature can range between 150-1300 K, depending on the sample size, number of heating wires and so on. The methods adopted for sample annealing is either thermionic irradiation or electron bombardment.

### **The SuperESCA beamline at Elettra**

SuperESCA is the first operative beamline at Elettra since 1993, and it is best suited for High Resolution core level Photoemission Spectroscopy (HR-XPS), X-ray absorption (XAS) and XPD. The combination of high flux SR and high resolution (energy resolution down to 30 meV) data acquisition capabilities makes this workstation particularly suitable for the investigation of low density systems such as thin films, surface adsorbates and supported nano-clusters. Until December 2010, the insertion device of SuperESCA was a 56-mm-period undulator with 81 periods, formed by three equal modules. By changing the gap width, the photon energy band can be varied between 85 eV and 1000 eV at 2.0 GeV ring energy. A new linear planar undulator has been recently installed that will produce higher brilliance photon beams and will extend the energy range up to 1500 eV. UHV conditions (less than  $1 \times 10^{-10}$  mbar) are ensured

by a set of two full-range turbomolecular pumps.

The geometry of the chambers and their main instrumentations are shown in fig. 2.12a. The “heart” of this experimental station consists of two chambers separated by a gate valve, the preparation chamber and the main chamber. The preparation chamber is equipped with a VG sputter gun, a plasma ion source, feedthroughs for the evaporators, and it is connected to the gas line. Once the specimen has been prepared, it is transferred into the main chamber where the measurements take place. This bigger chamber is equipped with a PHOIBOS 150 mm hemispherical analyzer coupled with a delay-time detector. Besides the traditional *sweep* mode, the analyzer allows to work also in the so-called *snapshot* mode; which relates the spatial dispersion of the electrons at the detector to their energy distribution, thus significantly reducing the spectra acquisition time. A LEED system, a UV lamp, a monochromatic electron gun, a supersonic molecular beam, gas inlet and a mass spectrometer are also installed for various purposes.

In the fully automated manipulator, which is designed for XPD experiments, movements of the five degree of freedom are controlled by LabView programs, as well as the acquisition of photoemission spectra. Together with the availability of SR and the snapshot acquisition mode, these are reasons why very fast XPS and XPD measurements are possible at this beamline. These appealing features make it possible to monitor the surface reaction in real time by means of high resolution photoemission spectroscopy at the at SuperESCA beamline.

### The VUV photoemission beamline at Elettra

The VUV photoemission beamline (ISM-CNR and Elettra) is designed primarily for surface and solid state experiments by means of high resolution photoemission spectroscopy, including core-level photoemission, Angle-Resolved Photoemission (ARPES) for band mapping, XAS in the VUV and soft X-ray range and, in this case, photoelectron diffraction.

A top-view of the experimental setup of the station is schematically shown in figure 2.12b. The spherical chamber on the left side is dedicated to photoemission data acquisition, and is separated from the cylindrical preparation chamber on the right side by a pneumatic valve. The base pressure in the preparation chamber is low enough ( $10^{-10}$  mbar) to avoid possible sample contamination after preparation, and the pressure in the main chamber is even better ( $10^{-11}$  mbar). In fact, generally it is possible to perform measurements for more than 6 hours without significant degradation of the specimen. In the preparation chamber, two evaporation sources with separate pumping system are mounted, and another Omicron triple evaporator is installed directly in the chamber as well.

Both the measurement and preparation chambers have a manipulator, in the first case, there is a vertical manipulator with five degree of freedom; in the second, a horizontal manipulator with six degree of freedom ( $x, y, z, \vartheta, \varphi$  and *tilt*) is used.

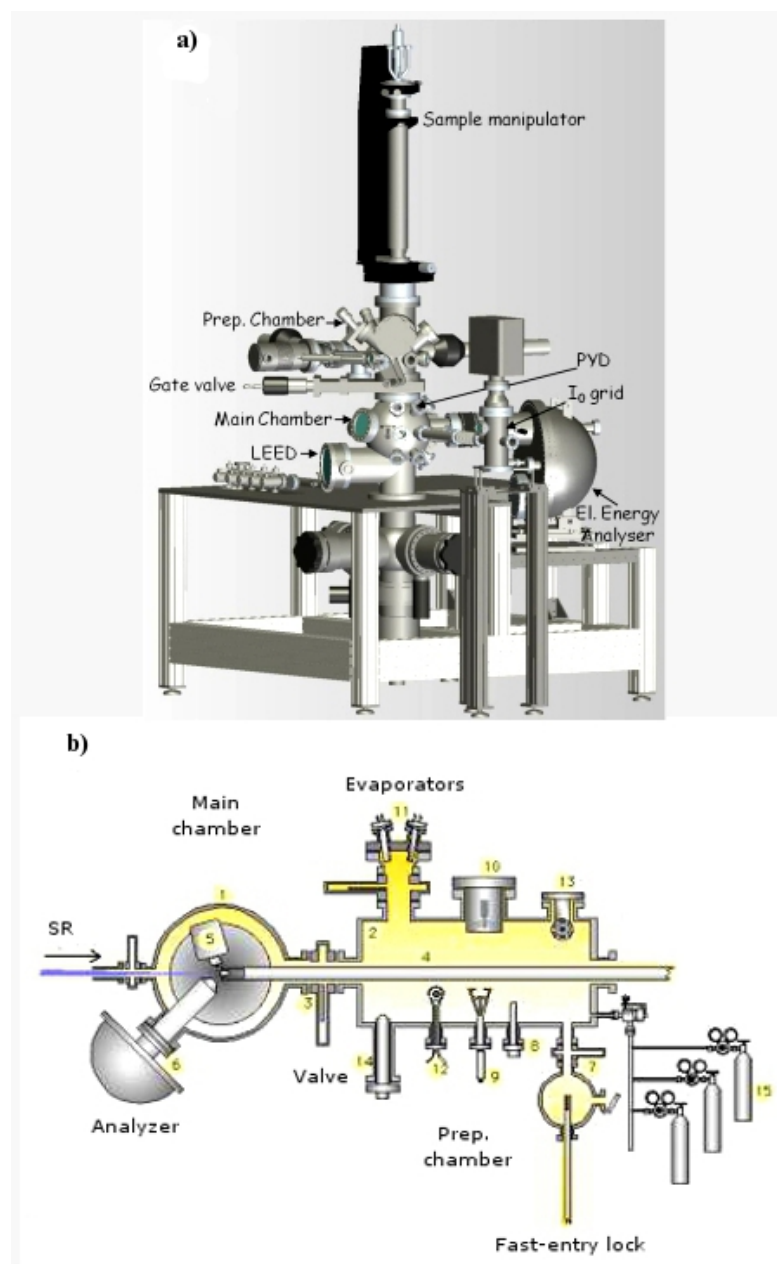


**Figure 2.12:** The experimental station at a) SuperESCA beamline and b) VUV photoemission beamline (top-view).

The VUV photoemission beamline utilizes a Scienta R4000 analyzer, which is particularly suitable for high resolution angle-resolved photoemission measurements. This analyzer has a 30 degree acceptance angle combined with a 2D detector with 670 parallel acquisition channels. This means that, in the energy scan mode, the detector collects in a single sweep 670 spectra at 670 distinct

emission angles distributed at both side of the central angle, with an even angular step. The highest angular resolution is equal to  $0.1^\circ$ , while the energy resolution in a typical Fermi surface mapping is better than 10 meV.

Finally, the motorized manipulator and the automatic data acquisition softwares makes this experimental station suited for X-ray photoemission measurements.

## 2.3 Structural determination

### 2.3.1 Photoemission spectra line-shape

The analysis of our experimental core-level spectra is performed by comparing the experimentally determined peak shape with a theoretical model. The theoretical curve is calculated by summing up the contributions of all the chemically non-equivalent species, plus their satellite or multiplet structures, and adding a background baseline. A single photoemission component is conventionally defined by the binding energy of the peak and its line-shape parameters. The shape of a photoemission component is mainly determined by a Lorentzian contribution, due to the finite core hole lifetime, and a Gaussian broadening, principally caused by thermal excitations and experimental resolution. Every XPS component has an intrinsic linewidth that is related to the core hole lifetime by the Heisenberg indetermination principle that relates time and energy uncertainties. A core hole created by the photo-ionization process can be filled by another electron from an external shell either non radiatively, by an Auger process, or radiatively, by X-ray fluorescence; the latter effect is basically the same physical mechanism exploited in the X-ray tubes described in subsection 2.2.2. The higher is the decay probability of a core hole, the shorter is its lifetime, and the larger is the Lorentzian FWHM,  $\Gamma$ , of the corresponding core level component. The Lorentzian contribution to the intensity is quantified by the following equation:

$$I_{\text{Lor}} = I_0 \frac{\Gamma/2\pi}{[(E_{kin} - E_0)^2] + \Gamma^2/4} \quad (2.25)$$

where  $I_0$  is the maximum intensity and  $E_0$  is the position of the adiabatic peak.

As already mentioned at the beginning of this chapter, core level photoemission peaks from solid metals, such as the TM crystals that we used, always exhibit an asymmetric inelastic tail due to multi-electron excitations that create electron-hole pairs above the Fermi level. This intrinsically asymmetric shape is appropriately described by the Doniach-Šunjić function [28], with which we have simulated all the theoretical XPS spectra during the photoemission spectral deconvolution. This function is a convolution of Dirac  $\delta$ -function that accounts for the photoemission process from a core level with BE  $E_0$ ,  $\delta(E) = 1/(E_0 - E)^{1-\alpha}$ , and the Lorentzian distribution for the previously described lifetime effect. An asymmetry parameter  $\alpha$  is introduced to take into account the inelastic tail of the photoemission spectrum. The  $\alpha$  parameter is related to the occurrence of the electron-hole scattering events by the equation  $\alpha = 2 \sum_l (2l + 1)(\delta_l/\pi)^2$ ,

where  $\delta_l$  represents the phase shift of the electron  $l^{th}$  partial wave from the hole potential. Then the intensity of a photoemission spectrum can be expressed as:

$$I_{DS}(E_{kin}) = I_0 \frac{\Gamma_E(1 - \alpha)}{[(E_0 - E_{kin})^2 + \frac{\Gamma^2}{4}]^{(1-\alpha)/2}} \xi(E_{kin}) , \quad (2.26)$$

$$\text{where } \xi(E_{kin}) = \cos \left[ \frac{1}{2} \pi \alpha + (1 - \alpha) \tan^{-1} \left( 2 \frac{E_0 - E_{kin}}{\Gamma} \right) \right] . \quad (2.27)$$

$\Gamma_E$  is called  $\Gamma$  function defined by

$$\Gamma_E(x) = \int_0^\infty t^{x-1} e^{-t} dt . \quad (2.28)$$

To summarize, the theoretical curves we have employed for XPS data fitting are spectral functions resulting from the convolution of the asymmetric Doniach-Šunjić line-shape with a symmetric Gaussian distribution which accounts for the experimental energy resolution and peak broadening originating from vibrational and inhomogeneity effects.

### 2.3.2 Data processing and theoretical simulations

An accurate fitting procedure is the basis of XPD data analysis. Once the spectra acquired in different angular configurations ( $\vartheta, \varphi$ ) have been deconvoluted, the intensity modulation function for each spectral component,  $\chi(\vartheta, \varphi)$ , represents the actual experimental result from which structural information can be derived. Notice that, thanks to the intrinsic chemical sensitivity of the technique, each XPS component will have its own  $\chi$ -function. However, only the geometrically non-equivalent peaks are characterized by a distinct modulation function; whereas spin-orbit shifted components, and the final state satellites of the same core level will exhibit an identical  $\chi$ -function. This is the reason why, when performing the XPD measurement, we choose to focus on the the energy interval of just one spin-orbit component, thus significantly shorten the acquisition time.

Fig. 2.13a shows the how XPD angular mapping is performed in practice. Experimental XPD patterns show the intensity modulation of a selected XPS peak on the surface of the hemisphere above the plane of the sample surface. XPD patterns are conventionally presented in the form of stereographic projections of the modulation function at a given photon energy for a selected XPS component (an example is shown in fig. 2.13b). In this representation, the amplitude of the modulation function is indicated by the color scale on the left; the polar angle increases radially, as marked on the horizontal axis, and, the azimuthal angle is reported on the circular scale around the plot. In practice, since the XPD pattern is periodic and invariant under azimuthal rotations, we usually restrict the measurement to a smaller subrange of azimuthal angles (larger than the azimuthal period). The XPD pattern obtained from the measured slice can

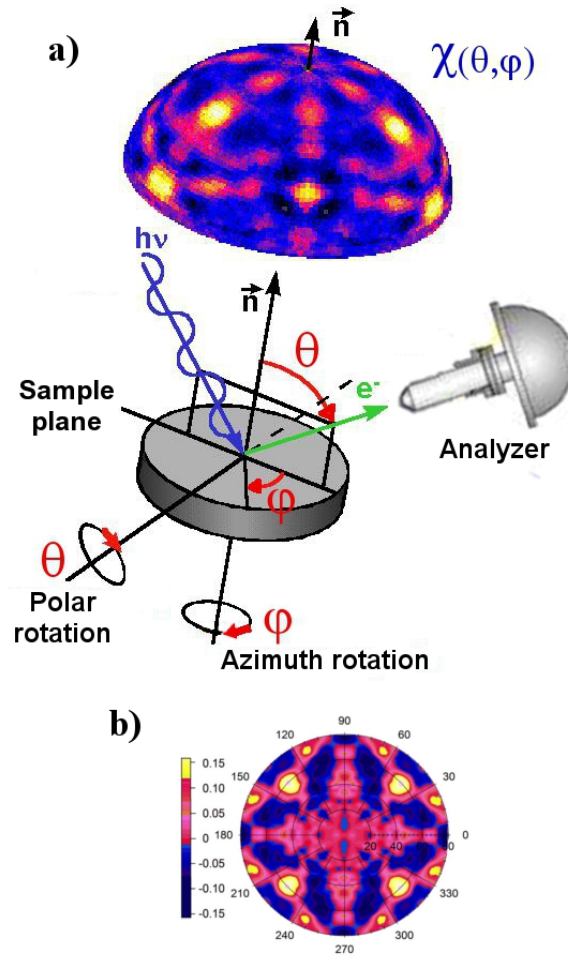


**Figure 2.13:** a) A schematic representation of angle-resolved XPD: a 2D  $\chi$ -function can be obtained by mapping the surface of the hemisphere ( $2\pi$  sterad) above the sample. b) A typical stereographic representation of XPD patterns, where the color scale indicates the amplitude of  $\chi$ -function.

be then replicated in order to reproduce the  $360^\circ$  azimuthal configurations for each polar angles.

The next step, which is the most important one, is the interpretation of the experimental modulation functions. Since the XPD patterns result from interference of direct and diffracted waves, a quantitative evaluation of the sample structure is not so straightforward. The best strategy is instead to compare the experimental data with multi-scattering theoretical calculations performed on a trial structure, and judge the goodness of the trial structure by means of a *reliability factor* (R-factor). In literature R-factor can come in different forms; one of the most accurate ones is the *Pendry's R-factor* widely used in LEED

analysis [29], defined as:

$$R = \sum_i \frac{[\chi_{\text{theory}} - \chi_{\text{exp}}]^2}{[\chi_{\text{theory}}^2 + \chi_{\text{exp}}^2]} \quad (2.29)$$

where  $\chi_{\text{theory}}$  and  $\chi_{\text{exp}}$  are the calculated and measured modulation functions, respectively. The sum runs over the whole data set for each angular positions and each photon energy. According to this definition, the Pendry's R-factor varies between 0 and 2; 0 indicates a perfect agreement between experiment and simulation, 1 means they are uncorrelated, and 2 means that the two patterns have an anti-phase correlation. In usual circumstances, R-factor values smaller than 0.3 are already considered to prove a pretty good agreement, since the theoretical calculations always simulate "ideal" situations which do not correspond to the real ones. In fact, the spurious effects caused by the sample misalignment, the analyzer transmission function, the intrinsic inhomogeneity of the specimen etc. can strongly influence the diffracted intensity, which should be rather avoided. In addition, discrepancies can derive also from limitations of the MS calculations because, exact calculations would request in principle an infinite amount of time and unlimited CPU resources. Therefore, as I will explain below, proper compromise is always necessary in order to get reasonable simulation times.

At this point, the determination of the structure generally reduces to the search of the minimum value of the R-factor, and its complexity increases with the number of independent structural parameters for which an optimum value has to be found. Given a structure which is completely determined by a set of  $n$  structure parameters, then the R-factor becomes a  $n$ -dimensional function with  $n$  independent variables. What one looks for is the absolute minimum of the R-factor (there should be only one) in the  $n$ -dimensional hyperspace. Instead of using a trial-and-error method, which is very time consuming, we developed custom XPD analysis method on the basis of both the *Steepest Descent algorithm* and the *Genetic algorithms* at each structural investigations. These *ad hoc* procedures sped up our R-factor minimizations. The fundamental criteria of genetic algorithms will be described in detail in chapter4, and for now I will discuss the steepest descent method which is widely used throughout the experiments reported in this thesis. The idea of this quite simple algorithm is the following. Starting at any point in the R-factor hyperspace, one can always take an infinitesimally small step, by simultaneously varying all the  $n$  variables along any direction, and calculate the gradient between these two points. If the initial position is already the absolute minimum, then the gradient will be zero; otherwise, it will indicate in which direction the R-factor decreases (sign of the gradient), and also how fast the variation is (modulus of the gradient). Therefore, once a reasonable initial configuration has been chosen, the R-factor minimization procedure consists of calculating a gradient and, if it is negative, moving in the direction of decrease until the lowest R-factor is reached. This process is iterated until the zero gradient point is achieved, and the procedure stops thereby. Obviously, every position is  $n$ -dimensional, and a gradient is

obtained by calculating the variations of R-factor with respect to each variable at every step. Consequently, the larger is the number of parameters, the more calculations are needed. Hence, only an irreducible number of fundamental structural parameters were chosen as variables in our R-factor minimization process.

Finally, to make sure that the zero-gradient R-factor is actually the lowest possible, its dependence on a single parameter variation is studied. The global minimum will not decrease for variations of any of the structural parameters.

I have learned to use two simulation codes for MS calculation, the Multiple Scattering Calculation of Diffraction (MSCD) package [26,30] and the Electron Diffraction in Atomic Cluster (EDAC) package [31]. Both of them have been used for the theoretical calculations in the experiments reported in the following chapters. Historically the MSCD code is older and more complicated than EDAC, but both of them have their own advantages and drawbacks. Some common features of these two codes consist in the implementation of the *atomic cluster method*, and the use multiple scattering theory to model the elemental and state-specific core level PD patterns of a surface. The IMFP and thermal vibrations of the lattice are introduced in a phenomenological way. As already explained before, owing to its local structure sensitivity, using atomic cluster model instead of simulating an infinite 2D surface is a time-saving procedure which avoids, at the same time, the loss of useful information. In addition, when the photoelectron diffraction process takes place very close to the surface (e.g. at low electron KE), parabolic cluster becomes a very efficient method, since it selectively excludes the unnecessary calculations for the deeper layers. Due to inelastic attenuations, the signals originated by the deep layers underneath the emitter are negligible compared to those from the scatterers of the surface layers. At the same time, this method maximizes the number of surface atoms used for MS calculations, which are far more important. A scheme of the parabolic cluster is shown in fig. 2.14. From this picture, it is clear how the number of atoms in a certain layer decreases with its distance from the surface, and how the surface sensitivity can be controlled by the definition of the cluster. For instance in order to enhance the surface contribution, one should reduce the height  $h$ , and increase the radius of the paraboloid  $r$ . In EDAC the extension of the cluster is defined by the distance between the focus (where the emitter is placed) and the border of the paraboloid, indicated with  $R$  in fig. 2.14. Using the EDAC code it is also possible to select cluster of spherical shape, which is useful to evaluate the PD modulations from deeper layers.

The most relevant difference between the two codes is the definition of the electron wave function for multiple scattering calculations. MSCD uses the Rehr-Albers approximation for the free electron Green's function, as described in section 2.1.2, and the *pathcut* parameter to avoid unnecessary calculations for negligible matrix elements, thus saving the computation time ( $t \cong N^3$ , where  $N$  is number of atoms). On the other hand, EDAC does not use the RA approximation, but expresses the electron wave function as a linear combination of *multiple*

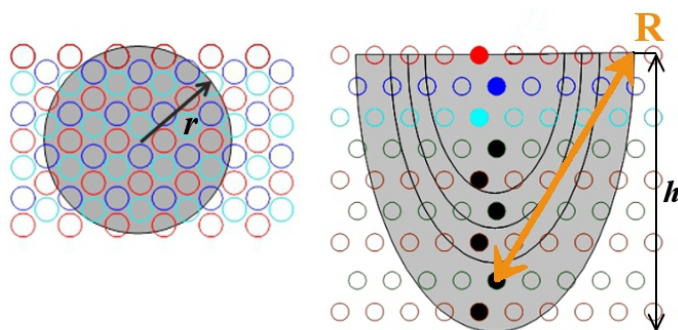


**Figure 2.14:** Top (left) and side (right) view of a typical parabolic cluster, the colored circles represent the atoms and the cluster is colored with grey. The most important parameters that define this cluster are the height  $h$  and the radius  $r$  of the surface cross-section in MSCD, and the distance  $R$  (yellow arrow) in EDAC. The atoms represented as a full circle are the center of each logical layer, they can be selected as emitter atom, while the empty spheres are the scatterers.

*curved outgoing waves*, and recursively refines their expansion coefficients. The higher is the number of iteration, the more accurate is the calculation. In this way, the computation time scales with  $N^2$  and depends linearly on the maximum number of iterations.

In summary, whatever theoretical approach is used, before performing the actual MS calculations a certain number of non-structural parameters have to be accurately chosen. These include cluster shape and size, the RA matrix dimension in the MSCD package, or the maximum angular momentum for the spherical wave expansion and the order of iterations in EDAC. The largest value of these parameters depends on the available computational resources and working time that one have. Beside numerical parameters, also some environmental parameters are usually left as adjustable. They are the inner potential, the sample temperature, and the Debye temperature of the system and the extension of the electron cloud into the vacuum level.

All the simulations that will be described in the following chapters was run on a 96 core High-Performance Computing (HPC) cluster, managed with a batch-queuing system called Sun Grid Engine (SGE) on an Unix platform, and located at the Scientific Computing section at Elettra. A set of custom developed scripts was used to automatize the job submission and monitoring activities.

---

## References

- [1] Siegbahn, K., Gelius, U., Siegbahn, H. & Olso, E. Angular distribution of electrons in ESCA spectra from a single crystal. *Phys. Scr.* **1**, 272 (1970).
- [2] Kono, S., Fadley, C. S., Hall, N. F. T. & Hussain, Z. Azimuthal anisotropy in deep core-level x-ray photoemission from an adsorbed atom: Oxygen on copper(001). *Phys. Rev. Lett.* **41**, 117 (1978).
- [3] Woodruff, P. *et al.* Diffraction of photoelectrons emitted from core levels of Te and Na atoms adsorbed on Ni(001). *Phys. Rev. Lett.* **41**, 1130 (1978).
- [4] Friedman, D. J. & Fadley, C. S. Final-state effects in photoelectron diffraction. *J. Electron Spectrosc. Relat. Phenom.* **51**, 689 (1990).
- [5] Fadley, C. S. Diffraction and holography with photoelectrons and Auger electrons: Some new directions. *Surf. Sci. Rep.* **19**, 231 (1993).
- [6] Woodruff, P. Surface structural information from photoelectron diffraction. *J. Electron Spectrosc. Relat. Phenom.* **178**, 186 (2010).
- [7] Fischer, A., Fasel, R., Osterwalder, J., Kronzer, A. & Schlapbach, L. Mg on Pd(111): The formation of local order observed by photoelectron diffraction. *Phys. Rev. Lett.* **70**, 1493 (1993).
- [8] Fadley, C. S. X-ray photoelectron spectroscopy: Progress and perspectives. *J. Electron Spectrosc. Relat. Phenom.* **178**, 2 (2010).
- [9] Bransden, B. & Joachain, C. *Physics of Atoms and Molecules* (Pearson Education, 2007), second edn.
- [10] Brundle, C. & Baker, A. *Electron Spectroscopy: Theory, Techniques and Applications*, vol. 2 (Academic Press, 1978).
- [11] Damascelli, A., Hussain, Z. & Shen, Z. X. Angle-resolved photoemission studies of the cuprate superconductors. *Rev. Mod. Phys.* **75**, 473 (2003).
- [12] Citrin, P. H., Eisenberger, P. & Hamann, D. R. Phonon broadening of x-ray photoemission linewidths. *Phys. Rev. Lett.* **33**, 965 (1974).
- [13] Kaduwela, A. P., Friedman, D. J. & Fadley, C. S. Application of a novel multiple scattering approach to photoelectron diffraction and auger electron diffraction. *J. Electron Spectrosc. Relat. Phenom.* **57**, 223 (1991).
- [14] Mårtensson, N. & Nilsson, A. On the origin of core-level binding energy shifts. *J. Electron Spectrosc. Relat. Phenom.* **75**, 209 (1995).
- [15] Citrin, P. H. & Wertheim, G. K. Photoemission from surface-atom core levels, surface densities of states, and metal-atom clusters: A unified picture. *Phys. Rev. B* **27**, 3176 (1983).

- [16] Ganduglia-Pirovano, M. V., Natoli, V., Cohen, M. H., Kudrnovský, J. & Turek, I. Potential, core-level, and  $d$  band shifts at transition-metal surfaces. *Phys. Rev. B* **54**, 8892 (1996).
- [17] Lizzit, S. *et al.* Surface core-level shifts of clean and oxygen-covered Ru(0001). *Phys. Rev. B* **63**, 205419 (2001).
- [18] Rodriguez, J. A. & Goodman, D. W. The nature of the metal-metal bond in bimetallic surfaces. *Science* **257**, 897 (1992).
- [19] Hammer, B., Morikawa, Y. & Nørskov, J. K. CO chemisorption at metal surfaces and overlayers. *Phys. Rev. B* **63**, 205419 (1996).
- [20] Orders, P. J. & Fadley, C. S. Single-scattering cluster calculations and Fourier-transform analyses of normal photoelectron diffraction. *Phys. Rev. B* **27**, 781 (1983).
- [21] Xu, M. L., Barton, J. J. & Hove, M. A. V. Electron scattering by atomic chains: Multiple-scattering effects. *Phys. Rev. B* **39**, 8275 (1989).
- [22] Greber, T. *et al.* Auger electron and photoelectron angular distributions from surfaces: Importance of the electron source wave. *Phys. Rev. Lett.* **69**, 1947 (1992).
- [23] Rehr, J. J. & Albers, R. C. Scattering-matrix formulation of curved-wave multiple-scattering theory: Application to x-ray-absorption fine structure. *Phys. Rev. B* **41**, 8139 (1990).
- [24] Sagurton, M. *et al.* Spherical-wave effects in photoelectron diffraction. *Phys. Rev. B* **41**, 2207 (1986).
- [25] Messiah, A. *Quantum Mechanics*, vol. 2 (Dover publications, 1999).
- [26] Chen, Y. *et al.* Convergence and reliability of the Rehr-Albers formalism in multiple-scattering calculations of photoelectron diffraction. *Phys. Rev. B* **58**, 13121 (1998).
- [27] Iwai, H., Namba, H., Kido, Y., Taguchi, M. & Oiwa, R. Improvement of spectrometer energy resolution for high-resolution photoelectron spectroscopy. *J. Synchrotron Rad.* **5**, 1020 (1998).
- [28] Doniach, S. & Šunjić, M. Many-electron singularity in x-ray photoemission and x-ray line spectra from metals. *J. Phys. C: Solid State Phys.* **3**, 285 (1970).
- [29] Pendry, J. B. Reliability factors for LEED calculations. *J. Phys. C: Solid State Phys.* **13**, 937 (1980).
- [30] Chen, Y. & Van Hove, M. A. [http://www.ap.cityu.edu.hk/personal-website/Van-Hove\\_files/mscd/mscdpack.html](http://www.ap.cityu.edu.hk/personal-website/Van-Hove_files/mscd/mscdpack.html).
- [31] García de Abajo, F. J., Van Hove, M. A. & Fadley, C. S. <http://nanophotonics.csic.es/static/widgets/edac/manual/edac.html>.



## Chapter 3

# O-Rh-O trilayer on Rh(100)

### 3.1 Introduction

In this chapter I'm going to discuss the structural determination of the ultra-thin oxide film formed on Rh(100). The XPD data presented in this chapter were collected during my Master thesis work. In the first year of the PhD, a considerable amount of time was devoted to computer simulations aimed at achieving a consistent interpretation of this structure.

Low Miller index surfaces of Transition Metal (TM) single crystals are widely employed in heterogeneous catalysis, because they are characterized by a high density of active sites for the dissociation of reactant molecules, thus promoting chemical reactions. One of the most widely studied TM-supported reaction is the CO oxidation. However, studies in the O<sub>2</sub> pressure range of 10<sup>-6</sup> ÷ 10<sup>-1</sup> mbar have pointed out that the catalyst does not remain metallic at all pressures, but thin oxide films start forming on the surface. Even more interestingly, the formation of ultra-thin oxide films seems to be related to the observed changes in the oxidation reaction rate. Therefore, surface scientists started addressing the role played by these new surface phases in the whole process. Today, after a consistent research efforts, it is acknowledged that the formation of thin oxide films can strongly influence the surface reactivity at close-to-ambient pressures [1,2]. Moreover, as the substrate oxidation proceeds, the appearance of bulk-like oxide phases is observed to slow down the overall reaction rate [3]. These findings have further boosted the interest in the properties of these peculiar thin films [4].

These are the reasons why the accurate determination of the structure, the origin and the reactivity of the ultra-thin oxide films plays an important role in the “pressure gap” debate. Even though studies on the interaction between different molecules and TM single crystal surfaces have yielded a deep insight into their reaction mechanisms in UHV conditions, at ambient pressures the same chemical reactions can follow far more complex pathways. This is the key issue in the “pressure gap” problem [5]. Nevertheless, the oxidation process of the TM surfaces at high pressure involves a number of intermediate phases, whose

formation depends on the pressure and temperature conditions chosen for the reaction. A thorough understanding of the nature and growth modes of ultrathin films would be of key importance in trying to bridge the “pressure gap”. To this purpose, an accurate analysis of the reaction steps involved in going from UHV to realistic conditions is required. In addition, thin oxide films can also be interesting in industrially relevant fields, since the pressure conditions required for their growth and employment are close to ambient pressure [4].

Furthermore, similar quasi-2D oxide films have been detected on the surfaces of a large variety of materials, including TM single crystals with different crystallographic orientations, bimetallic alloys and nanoparticles. In particular, formation of the surface oxide film has been evidenced on different low-index Rh, Pt, Pd and Ag single crystals [6–8]. Recent experiments have shown evidence of a surface oxide also on PtRh alloys [9] and on Rh nanoparticles [10]. Besides the observation of these oxide films on a variety of different substrates and under diverse conditions, the reactivity of these oxide films are still under debate [5,11,12]. These remarkable findings have certainly suggested a new research direction for surface scientists.

At the moment, there are still a lot of open questions that needed to be answered. For example, it is yet unclear why the surface oxide phase is much more reactive than both the clean surface and the corresponding bulk oxides; and in some cases, the identification of the actual reactive phase is still under debate. Over *et al.* explained the enhanced CO oxidation rate observed on Ru(0001) upon RuO<sub>2</sub> film growth in terms of a Mars and van Krevelen (MvK) mechanism [2]. In this process, the oxide film actively participates in the reaction acting as an oxygen buffer rather than as a mere support. In a first stage, the oxide film interacts with the CO molecules by donating O atoms which react with CO forming CO<sub>2</sub> molecules, thus leaving the surface as the final reaction product. The under-coordinated oxide film then re-oxidizes by interaction with the O<sub>2</sub> reactant from the gas phase. However, later experimental evidences have cast doubt on the idea that the thin RuO<sub>2</sub> film could be the actual active phase occurring at ambient pressure [12]. In fact, high-pressure XPS measurements have shown no direct correlation existed between the amount of the oxide film and the CO<sub>2</sub> activity. At the same time, a not well-ordered oxide phase was found on Ru surface, which showed a reactivity comparable with that of the RuO<sub>2</sub> film [13]. Moreover, it has been proved that the RuO<sub>2</sub> surface was deactivated by strongly bound carbonate species at room temperature and ambient pressure, hence the model proposed by Over *et al.* could not be valid in these conditions [14].

More recently, another hypothesis on the origin of the oxide film-induced reactivity enhancement has been advanced [3]. In this work, the interface strain between the oxide film and the TM substrate has been indicated as responsible for the higher surface reactivity during CO oxidation. Indeed, as soon as the lattice strain is released during the phase transition from a surface oxide to a thicker bulk-like oxide, the reaction rate is observed to slow down. Besides these explanations, a possible role of localized defects on the oxide films can't be ruled

out yet [4].

Actually, the surface oxide on Rh(100) has already been observed and characterized with the combined use of LEED-IV, STM and SXRD techniques [15]. Our XPD structural determination has the ultimate goal of validating the previous findings, and gaining some new insights into the interface bonding mechanism, by means of a detailed comparison between the structure of the thin film and of its corresponding bulk phase.

## 3.2 Experimental setup

The Rh(100) surface was cleaned by Ar<sup>+</sup> ion bombardment cycles (at 2 KeV energy) followed by sample annealing up to 1400 K. Chemical treatments in an O<sub>2</sub> background pressure of  $5 \times 10^{-8}$  mbar followed by hydrogen titration, were employed to remove C contaminants. After this cleaning procedure, the LEED pattern of the sample surface appears sharp and exhibits a low-intensity background. The recipe used to grow the ultra-thin Rh oxide film is the same as in Ref. [15], which consists of exposing the heated sample surface ( $T = 700$  K) to O<sub>2</sub> at  $1 \times 10^{-5}$  mbar pressure for 10 minutes. The surface oxide-covered Rh surface displays a characteristic LEED pattern showing extra diffraction spots due to the  $c(8 \times 2)$  coincidence cell.

The XPD measurements were performed at both the Surface Science Laboratory and at the SuperESCA beamline. The availability of both a high photon energy conventional X-ray tube and of a tunable high flux synchrotron radiation source allowed us to collect a large amount of structural information on the system under investigation. In fact, the high excitation energy used at the Surface Science Laboratory allows to collect XPD data mainly in the forward scattering regime. By contrast, the XPD patterns acquired at the SuperESCA beamline at lower photon energies are characterized by a large enhancement of the back-scattered photoemission signal, thus yielding complementary geometrical details. In addition, an accurate deconvolution of both the Rh $3d_{5/2}$  and the O $1s$  core level spectra was made possible by the high resolution XPS (HRXPS) measurements. Each chemically shifted component shows indeed a distinct modulation pattern, reflecting a different local atomic environment.

The whole XPD data set includes both 1D and 2D angular scans. Photon energies in the range 590–750 eV for the O $1s$  core level, and 380–550 eV for the Rh $3d_{5/2}$  core level, respectively, were used at the SuperESCA beamline, whereas at the SSL the photoemission scans were acquired at an excitation energy of 1486.6 eV. For all the 2D XPD patterns, the effective experimental angular span ( $\Delta\theta, \Delta\varphi$ ) was ( $80^\circ, 92^\circ$ ), while the azimuthal scans at fixed  $\vartheta$  cover an  $\Delta\varphi$  of  $120^\circ$ . The overall experimental scans span over  $254000^\circ$  angular configurations.

The EDAC simulation code was used for the calculation of the theoretical XPD patterns. This simulation package is particularly suitable for MS calculations involving scattering events occurring at several atomic layers below the sample surface; in other words, when a very large scattering cluster is needed.

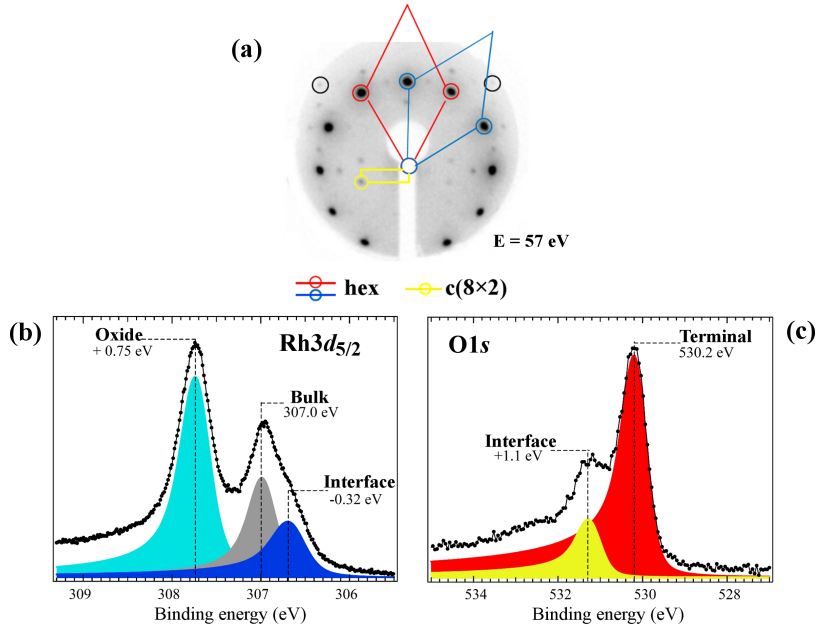


**Figure 3.1:** (a) LEED pattern of the surface after oxidation. The black circles indicate the  $(1 \times 1)$  geometry of the Rh substrate, the red and blue ones show the hexagonal symmetry of the trilayer and the coexistence of two domains rotated by  $30^\circ$  with respect to each other; the primitive cell of each of them is indicated in either blue or red. The  $c(8 \times 2)$  superlattice is indicated by a yellow rectangle. The HRXPS spectra of the  $\text{Rh}3d_{5/2}$  and  $\text{O}1s$  core levels were collected at  $h\nu$  650 eV and 400 eV, and are reported in panel (b) and (c), respectively.

This was indeed our case, in particular when the conventional X-ray source was used. The larger sampling depth, in fact, induces photoemission events from deeper bulk layers.

### 3.3 LEED and XPS data discussions

As I have mentioned before, the  $c(8 \times 2)$  oxide phase on  $\text{Rh}(100)$  had already been reported and investigated by Gustafson *et al.* [15]. Therefore, their previous results were taken as a reference and used as the starting point for our XPD analysis. A preliminary surface characterization has been carried out using LEED and HRXPS techniques. Besides the fact that these results yielded us a better understanding of the surface symmetry and of the nature of the non-equivalent spectral components, an accurate cross-check was very useful to make sure that the same surface oxide phase as the one documented in literature, had been obtained.

After oxygen exposure, the LEED pattern of the sample displays some distinctive intense spots disposed in a circle, as shown in fig. 3.1a. These spots are related to the hexagonal symmetry of the surface Rh oxide, and to the coexistence of two domains rotated by  $30^\circ$  with respect to each other; the primitive cell of each of them is indicated in either blue or red. The  $c(8 \times 2)$  superlattice

(indicated by the yellow rectangle in fig. 3.1a) arises from the superposition of the hexagonal O-Rh-O oxide thin film with the square Rh(100) substrate. Such rectangular superlattice also comes in 4 non-equivalent domains related to each other by rotations of multiples of  $90^\circ$ . This superlattice generates the  $(\frac{n}{8}, \frac{m}{2})$  fractional extra-spots in the LEED pattern, one of them is marked with the yellow circle. The O-Rh-O thin film is also called trilayer, because the surface oxide is composed by one Rh layer sandwiched between two O layers (above and below). Moreover, the same hexagonal in-plane symmetry characterizes these three layers, and the stacking of the O-Rh-O trilayer along the direction normal to the surface resembles that of an fcc lattice in the [111] direction. This is the reason why, even though three overlayers are present on the substrate, only one hexagonal periodicity appears in the LEED pattern. Conversely, atoms of the same species, but belonging to different layers, are clearly distinguishable in HRXPS measurements.

The photoemission spectra from the  $\text{Rh}3d_{5/2}$  and  $\text{O}1s$  core levels are reported in fig. 3.1b and in fig. 3.1c, respectively. In both graphs, the differently colored peaks represent the chemically shifted components as obtained from our fitting procedure, which makes use of Doniach-Šunjić functions convoluted with a Gaussian width. Moreover, each of these core level components is associated with a specific atomic layer. The  $\text{Rh}3d_{5/2}$  core level shows three components generated by Rh atoms located in oxide (cyan), interface (blue) and bulk (gray) layers. The BE shifts of the oxide and of the interface peaks ( $\Delta E = +0.75$  eV and  $-0.32$  eV, respectively) relative to the bulk peak (BE = 307.00 eV), are reported as well. Concerning the  $\text{O}1s$  core level, two features, generated by the topmost O layer (red) and by the interface layer above the Rh substrate (yellow), are displayed in fig. 3.1c. The two  $\text{O}1s$  core level components are separated by 1.10 eV. The number of components, and the extent of the BE shifts are all in good agreement with previous determinations [15]. It is also worth being noticed that the  $\text{Rh}3d_{5/2}$  spectrum exhibits an oxidized component whose intensity is much higher than that of the bulk and interface layer components. The spectrum was acquired at a low photon energy, so that the contribution from surface layers was enhanced with respect to that of the bulk. This allows us to increase our sensitivity to surface Rh layers, rather than to bulk Rh. Another interesting aspect of the XPS spectra of Rh surface oxide is the larger Gaussian width of the oxide peak (0.25 eV) compared to the metallic peaks (0.13–0.16 eV). Due to bonding with the O atoms, the oxidized Rh atoms show more localized electronic states with respect to the ones in the metallic bulk form. The ionic bonding between Rh and O strongly affects the local Rh-O and Rh-Rh atomic distances, and modifies the phonon modes and frequencies of the oxidized Rh layer [16]. Therefore, a more relevant broadening effect is expected for the Rh oxide than for the metallic Rh, thus leading to a larger Gaussian width of the spectral component. Moreover, another contribution to the spectral broadening of the oxidized component could originate from both the surface defects and the inhomogeneous distribution of non-equivalent atomic configurations.

### 3.4 XPD results

The theoretical model proposed by Gustafson *et al.* already shows a good agreement with our XPD experimental data. In fact, simulated XPD patterns using the DFT-derived structure model yield an R-factor of 0.21. Therefore, we carried out the subsequent structural relaxation starting from this structure. In this model, the O-Rh-O film consists of three slightly distorted hexagonal layers with two in-plane lattice constants of 3.09 Å and 3.07 Å along the [011] and [01 $\bar{1}$ ] lattice directions, respectively. The trilayer exhibits an fcc(111) stacking, and it overlaps with the Rh(100) substrate in such a way to form the larger c(8×2) superlattice. For the sake of simplicity, we labeled the terminal O layer, the oxide-Rh layer and the interface O layer with O<sub>2</sub>, Rh<sub>O</sub> and O<sub>1</sub>, respectively. At the oxide-metal interface, atoms of the O<sub>1</sub> layer adsorb on the Rh(100) surface shifting between on-top and bridge positions along the [01 $\bar{1}$ ] direction. In a preliminary XPD analysis, we tested all the other allowed adsorption sites, including also hollow and quasi-hollow sites, without altering the symmetry of the c(8×2) superlattice. It came out that the structure with no atoms adsorbed at the hollow sites is the one which yields the correct diffraction patterns. This result is surprising because, in the case of the atomic oxygen adsorption on Rh(100), it is well-known that the energetically most favorable adsorption site is the hollow one [17]. We will come back to this point in the section 5 of this chapter for a thorough discussion.

The experimental and simulated XPD patterns of both the O1s (left) and Rh3d<sub>5/2</sub> (right) core level, collected at different photon energies, are shown in fig. 3.2c. More precisely, each pattern describes the 2D intensity modulation of the individual XPS component, reported in the top graphs ((a) and (b)) (notice that the color scale of each XPD pattern has been chosen according to the color used for the corresponding XPS component in the top graph). Despite the higher intensity of the terminal O<sub>2</sub> component relative to the O<sub>1</sub> interface peak, the former exhibits a smaller modulation amplitude than the latter; similar behavior is encountered when comparing the modulation functions of the oxidized and interface Rh components. These differences in modulation amplitudes probably arise from an intrinsic geometrical effect. Photoelectrons emitted from the interface O<sub>1</sub> layer can be either scattered in the forward direction by atoms located in the Rh<sub>O</sub> and O<sub>2</sub> layers above, or scattered backwards by Rh atoms beneath the emitter layer. By contrast, photoelectrons originating from the terminal O<sub>2</sub> layer can be subjected only to back-scattering processes. Therefore, when collecting photoelectrons emitted from the O<sub>2</sub> layer, the intensity ratio between the directly emitted and the elastically scattered signal is much higher than that for the photoelectrons emitted from the O<sub>1</sub> layer. Furthermore, since the intensity modulation is produced by the interference between directly emitted and elastically scattered photoelectron wavefunctions, the larger the number of scattering events is, the higher the modulation amplitude of a particular photoelectron intensity will be. Similar arguments can be used to explain the differences between the modulation amplitude of the interface Rh

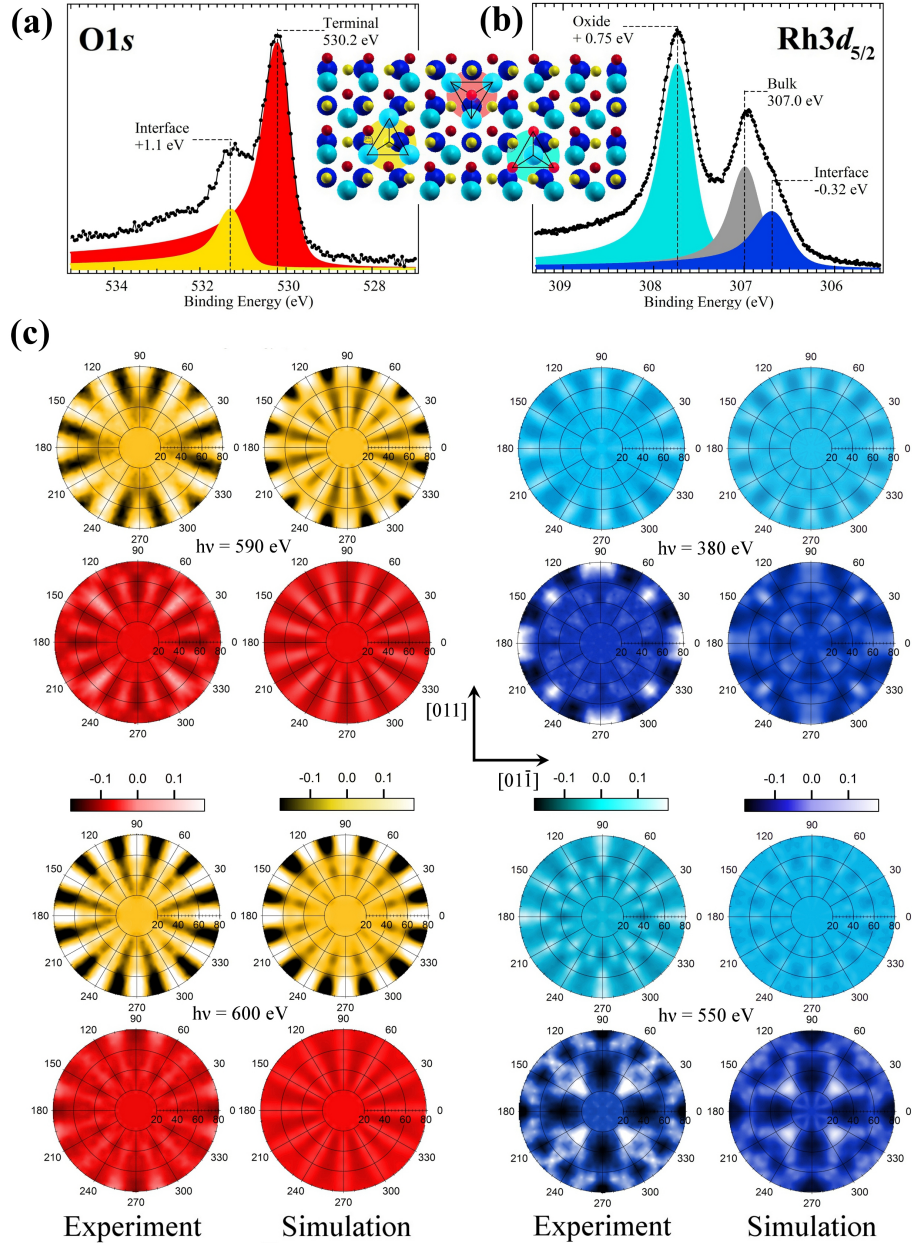


**Figure 3.2:** XPS spectra of the  $O1s$  (a), and  $Rh3d_{5/2}$  (b) core levels. For each XPS component, the corresponding experimental and simulated 2D modulation functions are reported in (c) and colored accordingly. The photon energies are also indicated besides the XPD patterns.

component and that of the oxidized Rh component.

The experimental XPD patterns reported in fig. 3.2 correspond to two distinct surface azimuthal periodicities, namely a  $90^\circ$  and a  $120^\circ$  rotational peri-

odicity. The diffraction patterns associated to interface Rh atoms reflect the square lattice symmetry of the Rh(100) substrate, hence they are characterized by a  $90^\circ$  periodicity. The XPD patterns of the oxide trilayer, on the other hand, exhibit a superposition of these two periodicities. In fact, the hexagonal symmetry of the trilayer would yield a  $120^\circ$  periodicity, but at some photon energies the contribution of the four rotational domains of the  $c(8\times 2)$  superlattice (which has a  $90^\circ$  periodicity) leads to the appearance of a seeming  $30^\circ$  periodicity.

The first step of our structural relaxation procedure consisted of optimizing the interlayer spacing within the trilayer and between the surface oxide and the Rh(100) substrate, which are indicated on the right side of fig. 3.3b. The distances yielded by our best fitting procedure are reported in the two bottom rows of tab. 3.1, and directly compared with the corresponding DFT and LEED-IV results reported in literature [15]. In a second step, a local structural relaxation was carried out to account for the individual positions of the atoms. This procedure allows to evidence possible interface layer rippling effects, which could be caused by the in-plane stress built up during the oxide trilayer growth. In order to accomplish an efficient R-factor minimization, it is advisable to employ the smallest possible set of independent structural parameters. Therefore, we grouped the Rh and O atoms close to the interface on the basis of symmetry criteria, and relaxed their positions along the  $z$  axis. Concerning the  $O_2$  and  $Rh_O$  layers, no local rippling effect is expected. This is because, differently from the  $O_1$  layer, atoms from the  $O_2$  and  $Rh_O$  layers are all found in identical threefold hollow sites, so that the lateral stress affecting these layers is much smaller than that accumulated in the interface layers.

	This work	Literature [15]	
	XPD	DFT	LEED-IV
$d(Rh_{S1}-O_1)$	$2.12 \pm 0.10$	1.88	$1.86 \pm 0.08$
$d(Rh_{S2}-O_1)$	$2.07 \pm 0.10$	1.89	$1.88 \pm 0.05$
$d(Rh_{S3}-O_1)$	$2.15 \pm 0.15$	1.92	$1.92 \pm 0.05$
$d(Rh_{S4}-O_1)$	$2.13 \pm 0.15$	1.94	$1.89 \pm 0.05$
$d(Rh_{S5}-O_1)$	$2.10 \pm 0.10$	1.89	$1.95 \pm 0.08$
$d(O_1-Rh_O)$	$0.95 \pm 0.02$	1.01	$1.03 \pm 0.02$
$d(Rh_O-O_2)$	$0.95 \pm 0.02$	0.92	$0.92 \pm 0.03$

**Table 3.1:** Out-of-plane interaction distances of the  $c(8\times 2)$  structure obtained from our XPD analysis, compared with the values obtained by LEED-IV and by DFT calculations. All values are in  $\text{\AA}$ .

The final structural results, obtained by implementing the steepest-descent algorithm for R-factor minimization, are reported in tab. 3.1. Compared to the DFT model, this structure yields a slightly better agreement with the experimental XPD data, with an R-factor of 0.19. For ease of data interpretation, inter-atomic distances are shown instead of the absolute  $z$  coordinates.

The most relevant result is the fact that, while the atoms of the  $O_1$  layer prefer to keep the same vertical position, buckling effects emerge for the non-

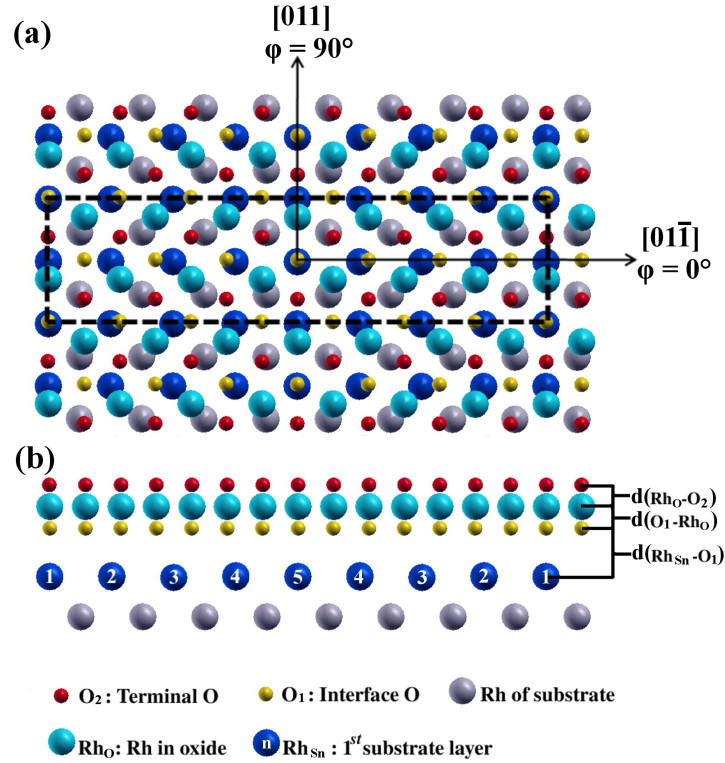


**Figure 3.3:** (a) Top view and (b) side view of the theoretical model obtained from XPD structural relaxation. The red ( $O_2$ ) and the yellow ( $O_1$ ) spheres represent the terminal and interface O atoms, respectively. The cyan atoms ( $Rh_O$ ) indicate the oxidized Rh layer. Interface Rh layer atoms are blue, while the gray atoms belong to the Rh(100) substrate. The colors of each atomic species are consistent with those used in fig. 3.1 for the chemically shifted XPS components.

equivalent Rh atoms of the first substrate layer. These atomic configurations are labeled with  $Rh_{S1}, \dots, Rh_{S5}$  in fig. 3.3, and the extent of the associated buckling is reported in tab. 3.1. Compared with the results of the LEED-IV and DFT analysis, the interlayer distances obtained in our work are on average  $0.2 \text{ \AA}$  larger. In fact, the shortest Rh-O distance at the metal-oxide interface according to the previous finding amounts to  $1.86 \pm 0.08 \text{ \AA}$ , and the average interlayer distance is  $1.90 \text{ \AA}$ . In our case, these values are  $2.10 \pm 0.10 \text{ \AA}$  and  $2.11 \text{ \AA}$ , respectively. However, considering that the Rh-O distances for bulk oxide phases found in literature range from  $1.96 \text{ \AA}$  to  $2.10 \text{ \AA}$  [18–20], our XPD result is still physically acceptable.

In order to demonstrate that this structure is actually the most reliable model, or equivalently, that our lowest R-factor is the absolute minimum in the R-factor hyperspace, we studied the evolution of the R-factor as a function of each single structural parameters. Each of the 8 curves reported in fig. 3.4 shows the dependence of the total R-factor on a single structural parameter. The

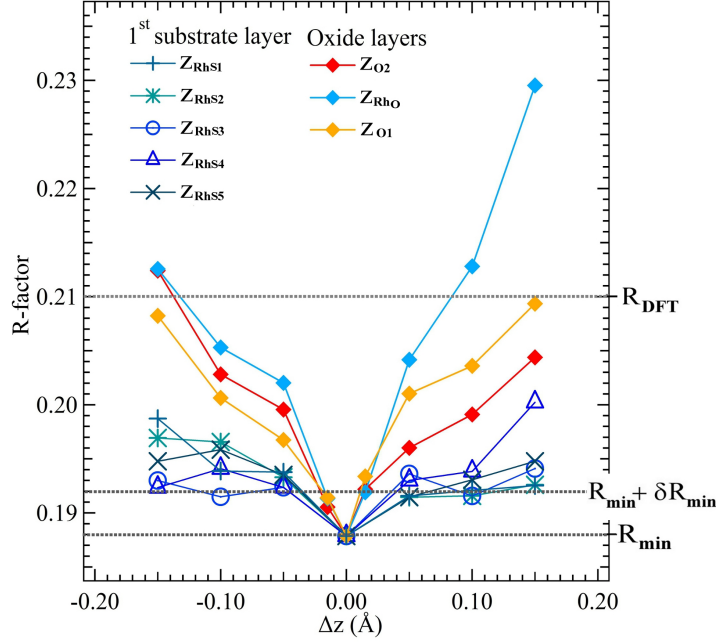


**Figure 3.4:** R-factor curves as a function of the independent structural parameters used in the R-factor minimization.

R-factors is reported on the vertical axis, and the  $\Delta z$  values reported on the horizontal axis indicate the variations of the individual geometrical parameters along the  $z$  direction. This graph clearly tells that the absolute minimum of in the R-factor space has been achieved. In addition, these plots allow us to estimate our sensitivity to the individual atomic positions. In fact, since all parameters are varied within the same interval of  $\Delta z$  values, the relevance of a particular parameter can be judged from the curvature of the associated R-factor plot. For example, the  $z$ -coordinate of a whole atomic layer has a much larger influence on the total R-factor than the  $z$ -coordinate of a subgroup of equivalent atoms (which in our case contains 1/5 ML atoms). Accordingly, the curves of the R-factor as a function of the heights of the oxide layers ( $O_2$ ,  $RhO$  and  $O_1$ ) vary more rapidly than those obtained as a function of single atom coordinates of the interface layer ( $Rh_{S1}$ ,  $\dots$ ,  $Rh_{S5}$ ). The values of the R-factor calculated for the structures modelled on the basis of DFT ( $R_{DFT}$ ) and XPD ( $R_{min}$ ) are reported on this graph as a horizontal dashed line. The quantity  $\delta R_{min}$  is the estimated variance of our  $R_{min}$ , and was derived by implementing the method proposed by Woodruff in ref. [21]. In short, this variance is an estimate of the error bar affecting our best R-factor, and is based on experimental factors like the total angular span of our data set, and the number of independent parameters in all our XPD patterns. It sets an upper limit to the accuracy of our calculated R-factor values: two R-factors differing by an amount smaller than  $\delta R_{min}$  are considered as indistinguishable in our XPD analysis. On the other hand, the estimated variance of our R-factor determines also the experimental

uncertainties associated to the structural parameters, which are reported in tab. 3.1. In sight of these considerations, in fact, it is clear from fig. 3.4 why the curves of the R-factor as a function of the interlayer distances are affected by smaller error bars than those of the R-factor calculated as a function of the first substrate layer rippling: the radius of curvature of the former is smaller than that of the latter.

### 3.5 Discussion on the interface structure

As already mentioned before, the purpose of this section is to achieve a deeper understanding of the matching mechanism between the trilayer film and the Rh(100) substrate. The dissociative chemisorption of  $O_2$  on Rh(100) surface has been widely studied in literature [22]. It is well-known that atomic O tends to adsorb in threefold hollow sites at high coverage and avoids the on-top configuration [23]. In the present case, instead, the interface O atoms preferentially adsorb in either on-top or bridge lattice sites. Interestingly, similar interface adsorption mechanisms have been found for trilayer oxide films grown on Rh(111) and on Ir(111) [24,25]. In order to explain this peculiar behavior, we investigated the interface layer structure in close relationship with the local atomic arrangement of the bulk  $RhO_2$  phase.

Rh oxidation at ambient pressure can produce two kinds of bulk Rh oxide, namely  $RhO_2$  (rutile structure) and the  $Rh_2O_3$  (corundum structure) [18,26], and we chose the  $RhO_2$  bulk phase to make a comparison with our oxide trilayer. This choice was mainly dictated by two reasons. First, the  $RhO_2$  phase shows the same O coordination per Rh atom as in the O-Rh-O films. In addition, theoretical studies have evidenced similar electronic density of states for both the ultra-thin oxide film and the  $RhO_2$  structure, while the  $Rh_3O_2$  bulk phase shows a different electron density distribution [20].

The lattice structure of bulk phase  $RhO_2$  is schematically represented in fig. 3.5a. Bulk  $RhO_2$  crystallizes in the rutile structure, described by a tetragonal lattice with a basis formed by both Rh and O atoms [27]. This structure can also be considered as a lattice of O atoms (the red and yellow atoms) stacked in hexagonal layers, in such a way to form octahedral interstitial sites in the middle. Half of the octahedral sites are occupied by Rh atoms, which are locally coordinated to 6 oxygen atoms. The black lines in fig. 3.5 delimit one of the octahedrons. Each ligand (O) atom is coordinated in a planar trigonal geometry to three Rh nearest neighbors, as indicated by the red triangles in fig. 3.5. Owing to the significant charge transfer from Rh to O, the interaction between the metal and the O atoms has a strong ionic character. In addition, the electron-electron repulsion contributes to keep the ligands at the largest possible distance from each other [27]. The O atoms occupy the vertices of an octahedron around a Rh atom; at the same time each O atom is trigonally coordinated to three Rh atoms. Concerning the nature of the chemical bonding, the  $sp^2$  hybridized molecular orbitals of O form 3 planar  $\sigma$ -bonds with the Rh atoms. Therefore, in contrast to the strong  $d-d$  orbital repulsions in the ligand field, the bulk

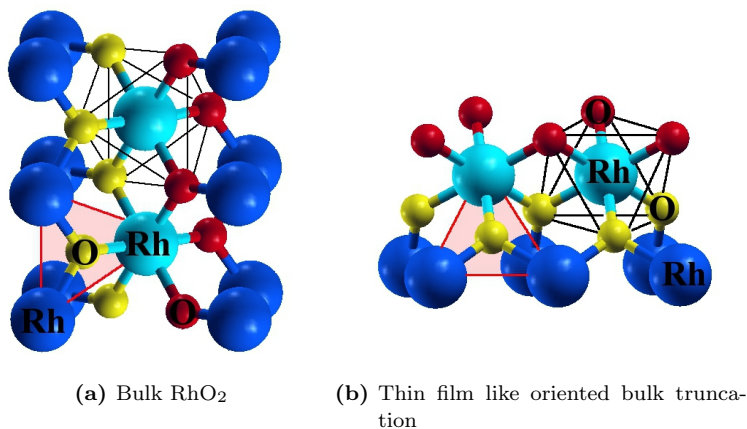


**Figure 3.5:** Structural comparison between the bulk phase RhO<sub>2</sub> and ultra-thin RhO<sub>2</sub> film supported on Rh(100).

RhO<sub>2</sub> phase is stabilized by the highly orientated  $\sigma$ -bonds between O and Rh atoms [28]. The structure in fig. 3.5b is obtained by eliminating one of the outer Rh layers from the structure in fig. 3.5a and by rotating the latter by 90°. In this way, such a truncated structure of bulk RhO<sub>2</sub> display an atomic arrangement very similar to the O-Rh-O trilayer supported on Rh(100). The red and yellow spheres represent the terminal and interface O atoms arranged in a hexagonal in-plane symmetry, while the Rh atoms (cyan spheres) are placed in the threefold fcc interstitial sites of the O layers. The blue Rh atoms are arranged in a square lattice like the first layer atoms of Rh(100). Owing to this close resemblance between the local structures of the bulk RhO<sub>2</sub> phase and of our RhO<sub>2</sub> thin film on Rh(100), similar Rh-O coordination mechanisms can be expected for these two systems. In fact, both the octahedral and trigonal complexes can be evidenced in the bulk-truncated structure in fig. 3.5b.

Since we are interested in the origin of the on-top and bridge oxygen adsorption sites observed at the interface between the trilayer and Rh(100), let's have a closer look at the bulk-truncated model in fig. 3.5b. Each interface O atom (yellow) is bound to either one or two Rh atoms (cyan) of the oxide phase. As it can be easily noticed, the yellow interface O atoms are also bonded to either one or two substrate Rh atoms (blue), and these two configurations can be compared to on-top or bridge adsorption sites, respectively. In addition, in order to keep a trigonal local geometry, like in the bulk phase, only these two adsorption sites are allowed for interface O atoms. By contrast, the fourfold and threefold hollow sites would violate the trigonal geometry required by the O  $sp^2$  hybridized orbitals. However, the lattice constants of the oxide film and of the bulk phase are different, and the triangles formed by Rh atoms around the interface O atoms are distorted by lattice stress. Consequently, the observed increase of the oxide-substrate distance, and the Rh surface layer rippling, can be considered as an attempt to restore a local geometry with both trigonal and

planar symmetry.

### 3.6 Conclusions

In this chapter the structural determination of a ultra-thin oxide film grown on Rh(100) has been discussed. The final model structure elaborated by means of XPD analysis is in good agreement with the previous results based on the combined use of DFT, LEED-IV, SXRD and STM techniques. In this way, we have independently cross-validated the trilayer model for the surface ultra-thin oxide on Rh(100).

Besides the atomic structure at the oxide-metal interface, we also highlighted the importance of a thorough understanding of the interaction mechanism between the oxide film and the substrate. In particular, we have noticed that the adsorption of atomic O at the interface with the Rh substrate follows an unusual geometry: on-top and bridge positions are preferred to the hollow sites, though the latter are energetically more favorable in the case of atomic O chemisorption. In addition, the same behavior has been observed also for the similar ultra-thin films formed on Rh(111) and Ir(111). Therefore, the reasons for this peculiar interface matching mechanism have to be found exclusively in the intrinsic geometrical structure of the thin film. An accurate comparison was carried out between the O-Rh bonding mechanism on the oxide-metal interface and in bulk  $\text{RhO}_2$ . In this way, we discovered a close affinity between the local coordination of the O atoms in the bulk and the film phases. In both cases, indeed, the O atoms show a strong tendency to occupy trigonal sites formed by 3 nearest neighbor Rh atoms, and this coordination number leads to adsorption in bridge or on-top sites, rather than in hollow sites. Furthermore, we argued the interface rippling effect and the relatively large film-substrate distance as a consequence of the lattice strain induced by the structural differences of the oxide film with respect to the bulk phase.

---

## References

- [1] Gustafson, J. *et al.* Sensitivity of catalysis to surface structure: the example of CO oxidation on Rh under realistic conditions. *Phys. Rev. B* **78**, 045423 (2008).
- [2] Over, H. *et al.* Atomic-scale structure and catalytic reactivity of the RuO<sub>2</sub>(110) surface. *Science* **287**, 1474 (2000).
- [3] Flege, J. I. & Sutter, P. *In situ* structural imaging of CO oxidation catalysis on oxidized Rh(111). *Phys. Rev. B* **78**, 153402 (2008).
- [4] Gustafson, J. *et al.* Structure and catalytic reactivity of Rh oxides. *Catal. Today* **145**, 227 (2009).
- [5] Rupprechter, G. & Weilach, C. Mind the gap! Spectroscopy of catalytically active phases. *Nano Today* **2**, 20 (2007).
- [6] Lundgren, E. *et al.* Surface oxides on close-packed surfaces of late transition metals. *J. Phys.: Condens. Matter* **18**, R481 (2006).
- [7] Chen, M. *et al.* Highly active surfaces for CO oxidation on Rh, Pd, and Pt. *Surf. Sci.* **601**, 5326 (2007).
- [8] Reichelt, R. *et al.* Low energy electron diffraction and low energy electron microscopy microspot I/V analysis of the (4×4)O structure on Ag(111): surface oxide or reconstruction? *J. Chem. Phys.* **127**, 134706 (2007).
- [9] Westerström, R. *et al.* Structure and reactivity of a model catalyst alloy under realistic conditions. *J. Phys.: Condens. Matter* **20**, 184018 (2008).
- [10] Mittendorfer, F., Seriani, N., Dubay, O. & Kresse, G. Morphology of mesoscopic Rh and Pd nanoparticles under oxidizing conditions. *Phys. Rev. B* **76**, 233413 (2007).
- [11] Over, H., Muhler, M. & Seitsonen, A. Comment on “CO oxidation on ruthenium: the nature of the active catalytic surface” by D.W. Goodman, C.H.F. Peden, M.S. Chen. *Surf. Sci.* **601**, 5659 (2007).
- [12] Goodman, D. W., Peden, C. H. F. & Chen, M. CO oxidation on ruthenium: the nature of the active catalytic surface. *Surf. Sci.* **601**, L124 (2007).
- [13] Blume, R. *et al.* Catalytically active states of Ru(0001) catalyst in CO oxidation reaction. *J. Catal.* **239**, 354 (2006).
- [14] Rössler, M., Günther, S. & Wintterlin, J. Scanning tunneling microscopy of the RuO<sub>2</sub>(110) surface at ambient oxygen pressure. *J. Chem. Phys. C* **111**, 2242 (2007).
- [15] Gustafson, J., Mikkelsen, A., Borg, M., Andersen, J. N. & Lundgren, E. Structure of a thin oxide film on Rh(100). *Phys. Rev. B* **71**, 115442 (2005).

- [16] Bancroft, G. M. *et al.* Toward a comprehensive understanding of solid-state core-level XPS linewidths: experimental and theoretical studies on the Si 2*p* and O1*s* linewidths in silicates. *Phys. Rev. B* **80**, 075405 (2009).
- [17] Bianchettin, L. *et al.* Surface core level shift: high sensitive probe to oxygen-induced reconstruction of Rh(100). *J. Phys. Chem. C* **113**, 13192 (2009).
- [18] Coey, J. M. D. The crystal structure of Rh<sub>2</sub>O<sub>3</sub>. *Acta Cryst.* **B26**, 1876 (1970).
- [19] Wong, K. C., Liu, W. & Mitchell, K. A. R. LEED crystallographic analysis for the Rh(111)-(2×1)-O surface. *Surf. Sci.* **360**, 137 (1996).
- [20] Mittendorfer, F. Low-dimensional surface oxides in the oxidation of Rh particles. *J. Phys.: Condens. Matter* **22**, 393001 (2010).
- [21] Woodruff, D. Adsorbate structure determination using photoelectron diffraction: methods and applications. *Surf. Sci. Rep.* **62**, 1 (2007).
- [22] Comelli, G., Dhanak, V., Kiskinova, M., Prince, K. & Rosei, R. Oxygen and nitrogen interaction with rhodium single crystal surfaces. *Surf. Sci. Rep.* **32**, 165 (1998).
- [23] Baraldi, A. *et al.* Spectroscopic link between adsorption site occupation and local surface chemical reactivity. *Phys. Rev. Lett* **93**, 046101 (2004).
- [24] Gustafson, J. *et al.* Self-limited growth of a thin oxide layer on Rh(111). *Phys. Rev. Lett.* **92**, 126102 (2004).
- [25] He, Y. B. *et al.* Oxidation of Ir(111): from O-Ir-O trilayer to bulk oxide formation. *J. Phys. Chem. C* **112**, 11946 (2008).
- [26] Grillo, M. Electronic control of the stability of rutile- versus corundum-type structures of ruthenium and rhodium oxides. *Comp. Mater. Sci.* **33**, 83 (2005).
- [27] Sorantin, P. I. & Schwarz, K. Chemical bonding in rutile-type compounds. *Inorg. Chem.* **31**, 567 (1992).
- [28] Demazeau, G., Matar, S. F. & Pöttgen, R. Chemical bonding in metallic rutile-type oxides *TO*<sub>2</sub> (*T* = Ru, Rh, Pd, Pt). *Z. Naturforsch* **62b**, 949 (2007).



## Chapter 4

# Ni oxide nanostructures on Rh(111)

### 4.1 Introduction

In this chapter I am going to discuss the different low-dimensional Ni oxide phases grown on the Rh(111) surface. This project was carried out in close collaboration with the Surface Science group of the Institute for Experimental Physics of Karl-Franzens Universität (Graz, Austria). Starting from their previous STM and HREELS analysis of the Ni oxide phases, our combined LEED, XPS and XPD investigations successfully determined both the structure and the chemical states of the most relevant oxide films observed in this experiment. The goal of this extensive study is to characterize the structure of the different 1D and 2D Ni oxide phases formed on Rh(111) under different oxidation conditions, and to gain some insight into the effect of the interface interactions on the formation of the oxide films.

The interest of the scientific community on oxide films has been stimulated by the increasing demand of novel low-dimensional materials with tailored properties for various applications in technologically relevant fields [1–3]. In general, oxide nano-structures are stabilized by the growth on a suitable metal support. In this way, they can be easily prepared with high accuracy and characterized by surface-sensitive probes. However, metal supports can interact with surface oxides by inducing an interface epitaxial strain or an electronic state coupling [4], thus significantly affecting the properties of the oxide films [5]. Moreover, at low film thickness, the epitaxial Ni layers are observed to form different oxide phases with a different oxygen stoichiometry. Each of these low-dimensional oxide structure is expected to exhibit distinct chemical and physical properties [6]. The thorough investigation of these oxide films has indeed the ultimate aim of developing a procedure to fabricate specific nano-oxide phases with the desired catalytic and conductive properties.

Compared with the  $\text{RhO}_2$  surface oxide, the 3d-TM oxides ( $\text{MnO}$ ,  $\text{CoO}$ ,  $\text{FeO}$ ,  $\text{NiO}$  and  $\text{CuO}$ ) have been more widely studied in solid state physics due to their outstanding electronic and magnetic properties. In particular,  $\text{NiO}$  historically represents the model test bench for the theoretical description and the experimental characterization of these first-row TM monoxides. For more than 60 years, great research efforts have been put into unravelling the electronic structure of this strongly correlated system. Although many of its properties have been experimentally revealed, the interpretation of their electronic structure is still a tough issue from the theoretical point of view [7,8].  $\text{NiO}$  has the crystal structure of rocksalt with a local octahedral coordination ( $\text{NiO}_6$ ), and is a high-spin antiferromagnetic insulator [9]. The actual bottleneck in the understanding of the intrinsic complexity of  $\text{NiO}$  is represented by its insulating character. In fact, while the classical band theories, which do not include correlation effects between  $d$ -electrons, predict a metallic band structure of  $\text{NiO}$ , experimental evidence has been proved of the existence of an insulating gap [10].

Throughout the years, many theoretical approaches have been proposed in order to account for electron correlations. The oldest one is the Mott-Hubbard model, according to which  $\text{NiO}$  is classified as a *Mott-Hubbard insulator* [11]. The band gap is estimated from the difference between the *electron hopping integral*, which accounts for the  $d$ -band formation from the overlap of delocalized electronic states, and the *on-site Coulomb repulsion*, which instead contributes to localize and narrow the  $d$ -bands, thus inducing a band gap opening. In this model the highest occupied  $d$ -band is called Upper Hubbard Band (UHB), while the lowest unoccupied  $d$ -band is called Lower Hubbard Band (LUB), and the  $\text{NiO}$  band gap is given by the separation between the UHB and the LHB. However, the Mott-Hubbard model neglects the  $\text{O}2p$ - $\text{Ni}3d$  orbital hybridization induced by the chemical bond. The contribution of the  $\text{O}2p$  electrons involved in the  $\text{Ni-O}$  covalent bonding can actually modify the  $d$ - $d$  insulating gap by shifting the  $\text{O}2p$  band in between the UHB and the LUB. In order to compensate for this inadequacy, a new theoretical model was introduced by Zaanen, Sawatzky and Allen [12], in which the  $\text{NiO}$  is treated as a *Charge-Transfer (CT) insulator*. In this model, electron hopping is allowed also between the  $\text{Ni}$  and  $\text{O}$  atoms of the same  $\text{NiO}_6$  lattice unit, thus leading to the formation of the molecular  $p$ - $d$  hybrid band [8].

Although these widely acknowledged works have significantly contributed to a deeper phenomenological understanding of the  $\text{NiO}$  electronic structure, there are still many discrepancies between the experimental photoemission spectra and the corresponding theoretical predictions. For example, most theoretical methods underestimate the extent of the  $\text{NiO}$  band gap [7]. A satisfactory description of the photoemission spectra, which correctly reproduces the spectral weights of the  $d$ - and  $p$ -type contributions to the VB, has still to be provided [13]. In addition, there are also debates on whether  $\text{NiO}$  is a Mott-Hubbard or charge-transfer insulator, or both [7,8].

While the bulk phase late TM oxides have attracted considerable interest

due to the peculiar insulating character described before, at the 2D limit, the artificial ultra-thin oxide films seem to represent a class of innovative materials which exhibit even more amazing properties. As a consequence of the anisotropic spatial confinement acting on the thin films, the effect of interface interactions can strongly influence the final properties of the low-dimensional systems. Interface mechanisms including lattice matching/mismatching, bond distortions and layer buckling produced both by the strong atomic interactions and lattice stress forces, can play a predominant role in tailoring the available energy and spin states of the interacting electrons. This is the reason why the ultra-thin oxide films of TMs are believed to be suitable candidates for the fabrication of next-generation semiconductors and magnets. In fact, given the small film thickness and strong  $d$ -electron correlation effects, the insulator-to-semiconductor transition can be more easily achieved with respect to the bulk oxide case. Besides, as will be discussed later, at the limit of a few ML thickness, the surface phases exposed by the oxide film can also be polarity-selective. Depending on the stacking sequence of the metal-oxygen layers, electrostatic forces can build up, which can control the stability of the film, as well as the total spin polarization. Indeed this phenomenon is at the basis of the formation of differently oriented NiO films reported in this chapter. Furthermore, the study of the electron spin interactions in these thin oxide films has paved the way for engineering of the *half-metals*, a kind of new material in which the conduction is carried out only by electrons of only one spin orientation. A large part of the known half-metals are doped thin oxide films, which have also potential applications on magnetoresistance-base devices thanks to the possibility to switch their magnetization due to the small film thickness and the strong electron correlations.

This chapter is divided into four main sections. The experimental details will be first described in section 4.2. An overview of all the surface phases observed during the oxidation of the Ni adlayers at a Ni coverage between 1 and 5 ML will be presented in section 4.3. For each value of the Ni film thickness, and depending on the O<sub>2</sub> exposure, either the O chemisorbed phase or the Ni oxide phases are showed up in a distinct manner. The different stages of oxidation were recorded and analysed by means of LEED and XPS. In addition, the origin of the different XPS components of the Ni2*p* core level spectrum, in both the metallic and oxide phases, will be discussed as well. Two of the most relevant structures will be addressed by our XPD structural analysis. The first one originates from O chemisorption on 5 ML Ni adlayers, and will be described in section 4.4. Besides the O adsorption sites, the strain relaxation mechanism at the Ni-Rh interface will also be discussed. The second phase consists of a new 2D Ni oxide structure observed at 1 ML Ni coverage, and will be described in section 4.5. This Ni oxide phase does not exist in nature, but can be stably formed only on Rh(111) by oxidation of the Ni monolayer. In order to efficiently model its atomic structure, a custom method for the R-factor minimization was implemented, which makes use of the basic concepts of the Genetic Algorithms (GAs).

## 4.2 Experimental setup

This XPD experiment was entirely performed at the Surface Science Laboratory. In this laboratory, the UHV chamber is equipped with a monochromatic Al  $K_\alpha$  X-ray source (1486.6 eV photon energy) and a manipulator especially designed for XPD measurements, whose motion is computer-controlled. For Ni deposition, a commercial Omicron EFM3 rod evaporator was mounted on the chamber. It was then carefully outgassed in such a way to ensure the purity of the evaporated atomic beam. The evaporator was also equipped with a beam shutter and a flux-monitor which allowed us to attain a selected deposition rate. Furthermore, to ensure a better control on the evaporation rate, a Quartz Microbalance was introduced in order to calibrate the evaporation flux prior to every Ni deposition. In this way we kept an average Ni deposition rate of 0.15 ML/min.

The Rh(111) single crystal was used for the Ni adlayer supported growth. This is a convenient choice, because the in-plane lattice constants of Rh(111) and Ni(111) are very similar, namely 2.69 Å and 2.49 Å, respectively. Hence, large domains of well-ordered hexagonal Ni overlayers can be grown on this substrate. Moreover, as will be discussed in section 4.4, such a small lattice mismatch (7%) favors the strain relaxation within the Ni adlayers. The preparation of the clean Rh(111) surface follows a similar procedure to that described for Rh(100) in the previous chapter. In brief, the sample surface undergoes a series of sputtering and annealing cycles up to 1400 K, followed by oxidation and reduction treatments in  $O_2$  and  $H_2$  background to remove residual contaminants.

All the surface phases described in section 4.3 were prepared following the same procedure, but changing the Ni coverage and the  $O_2$  pressure used for the oxidation at every new experiment. In a first stage, the metal Ni adlayer was epitaxially grown on the clean Rh(111) substrate, whose temperature was held at about 420 K. Keeping the surface heated enhances the Ni adatom mobility, thus promoting their arrangement into ordered layers. Since 420 K is much lower than the Ni segregation temperature on Rh(111) (600 K), both surface alloying and Ni segregation can be safely ruled out at this temperature. Once a Ni thin film with the desired thickness had been obtained, it was then exposed to an  $O_2$  flux at a pressure ranging between  $5 \times 10^{-8}$  and  $1 \times 10^{-6}$  mbar.

## 4.3 Phase study of the oxidation of ultra-thin Ni films

The different surface phases we observed upon oxidation of the epitaxial Ni ultra-thin films were investigated by using a combination of LEED, STM and XPS techniques. This allowed us to extract information on complementary aspects of the system under study, such as the surface symmetry and the lattice periodicity in both the real (STM) and reciprocal (LEED) space, and on the local chemical

environment of the core level electrons (XPS). The STM data presented in this work were acquired by the Surface Science group of the Karl-Franzens Universität at Graz, and provided useful insights into the surface topography of the different oxide films grown on Rh(111). The 1D and 2D NiO thin films described in the following will be divided into two groups according to the Ni coverage  $\theta_{\text{Ni}}$ .

### 4.3.1 Quasi 2D Ni oxides at $\theta_{\text{Ni}} \leq 1$ ML

In this set of experiments 1 ML Ni was deposited on Rh(111), and the substrate was subsequently exposed to an increasing  $\text{O}_2$  flux. In this way two new surface phases, the  $p(6 \times 1)$ -NiO and the  $(2\sqrt{3} \times 2)$ rect-NiO, were observed at an oxygen pressure of  $5 \times 10^{-8}$  (15 L) and  $1 \times 10^{-6}$  (300 L) mbar, respectively. In addition, the coexistence of both oxide structures was evidenced at an intermediate pressure of about  $5 \times 10^{-7}$  mbar (150 L), which probably indicates the occurrence of a surface phase transition.

The  $p(6 \times 1)$  structure is the oxide phase observed at the lowest Ni coverage. It is characterized by a series of equally spaced 1D protrusions. These ordered rows are clearly visible in the STM image of fig. 4.1a, where the  $p(6 \times 1)$  unit cell has also been highlighted. A series of STM scans over larger surface areas also evidenced the coexistence of two domains, in each of which the NiO rows are oriented parallel to either one of the two Rh(111) in-plane crystal axes. The LEED pattern of the  $p(6 \times 1)$ -NiO phase is reported in fig. 4.1b, in which the periodicity of the extra spots is visible along both the crystallographic directions of the Rh substrate, thus indicating the existence of the two domains mentioned above.

The  $\text{O}1s$  (red) and  $\text{Ni}2p$  (green) core level photoemission spectra corresponding to the  $p(6 \times 1)$ -NiO phase are reported in the central row of the graph in fig. 4.1e. Both the spin-orbit splitted sublevels of the  $\text{Ni}2p$  level are visible. On top of this graph the corresponding  $\text{Ni}2p$  spectrum of the 1 ML epitaxial Ni film prior to oxidation is reported for comparison. The  $\text{O}1s$  core level spectrum shows a very broad peak, and our spectral resolution was not high enough to allow us to resolve possible multiple components. Concerning the  $\text{Ni}2p$  core level spectrum, the main peak is shifted by 0.4 eV to higher binding energy with respect to the same feature in the corresponding spectrum of the metallic Ni film. The most relevant difference, however, is the apparent absence of the satellite peak on the high BE side of the main component ( $\Delta E \sim 5.8$  eV) of both the spin-orbit sublevels, which is instead visible in the spectrum of non-oxidized Ni. While the origin of the satellite peak in the metallic Ni phase is well-documented in literature [14,15], as will be described below, the reasons of this change in the spectrum of the  $p(6 \times 1)$ -NiO phase are still unclear. Nevertheless, since strong final state effects induced by  $d$ -electron correlation are observed in both metallic Ni and bulk NiO, large changes in the photoemission spectra can be reasonably expected also upon oxidation.

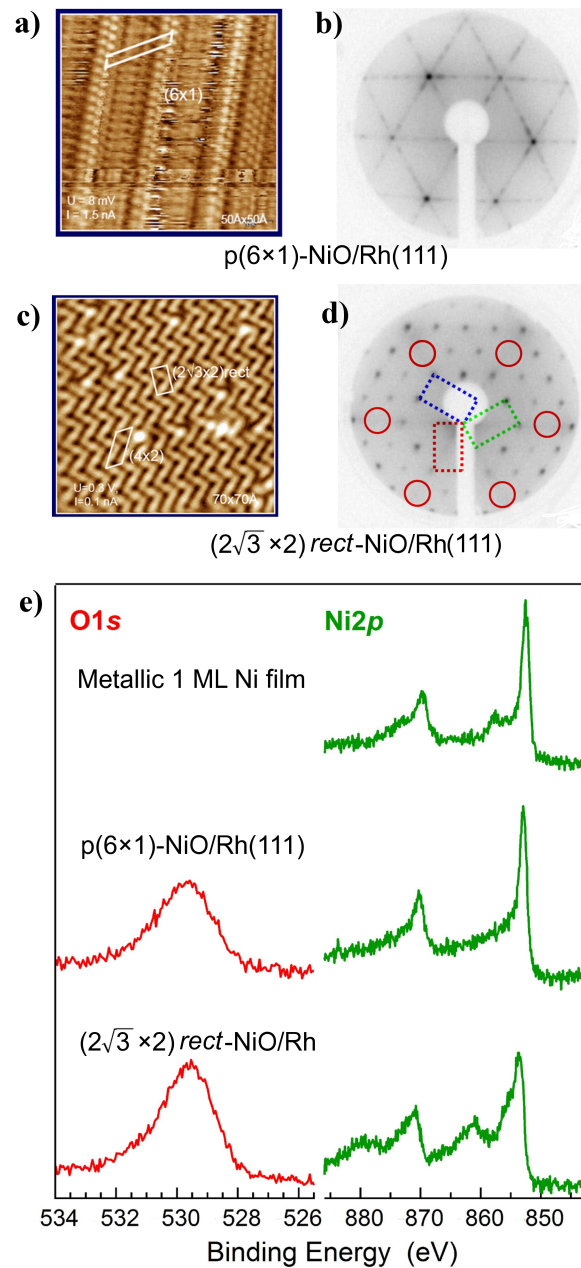


**Figure 4.1:** The two low-dimensional Ni oxides, namely the  $p(6 \times 1)$  and the  $(2\sqrt{3} \times 2)$ -*rect* phases, observed after oxidation of 1 ML Ni at different  $\text{O}_2$  pressure. a)–b) STM image ( $U = 8 \text{ mV}$ ,  $I = 1.5 \text{ nA}$ ) and LEED pattern ( $E = 150 \text{ eV}$ ) of the  $p(6 \times 1)$  phase. c)–d) STM image ( $U = 300 \text{ mV}$ ,  $I = 0.1 \text{ nA}$ ) and LEED pattern ( $E = 59 \text{ eV}$ ) of the  $(2\sqrt{3} \times 2)$ -*rect* structure. The three inequivalent domains, related by a  $120^\circ$ -rotation to each other, are also indicated in d). In panel e) the XPS spectra of the  $\text{O}1s$  and  $\text{Ni}2p$  core levels are reported together with the Ni spectrum prior to oxidation.

When a photoemission event occurs in a metal, in the present case Ni, both the main peak and the satellite structure in the photoemission spectrum are affected by final state effects. After the emission of a photoelectron from the  $2p$  core level, the core-hole creates a potential well which shifts the  $4s$  band and a branch of the  $3d$  band below the FL. This can result in two different final states, depending on which of these two bands is filled with a valence electron. The final state with electronic configuration  $c^{-1}3d^{10}4s^1$  originates the main peak, while the final state with electronic configuration  $c^{-1}3d^94s^2$  gives rise to the observed satellite component. In this notation,  $c^{-1}$  represents the core-hole left in the Ni  $2p$  subshell. As a consequence, the primary and the satellite peaks are associated to two distinct final states, and their integrated intensities are proportional to the probability of filling either the  $3d$  or the  $4s$  band. The 5.8 eV BE shift between these two components, on the other hand, can be ascribed to the larger core-hole screening effect produced by the  $3d$  band compared to that of the  $4s$  band. In fact, the photoelectrons originating from the channel in which a VB electron fills the  $4s$  band in the final state, come out with a smaller kinetic energy (and thus have a larger BE) because of the smaller screening effect on the nuclear charge. On the contrary, the photoelectrons contributing to the main peak are subjected to a more screened Coulomb potential from the nucleus, and are thus characterized by a smaller BE [14].

As discussed at the beginning of this chapter, the covalent Ni–O bond is stabilized by the hybridization between the  $O2p$  and  $Ni3d$  orbitals. This is the reason why the valence band of NiO exhibits completely different characteristics from those of metallic Ni. It follows that also the electron density of states at the FL in the oxide phase is significantly different from that of the corresponding metallic phase. This probably explains the absence of the satellite structure in the  $Ni2p$  spectrum of the  $p(6\times 1)$  phase.

The subsequent exposure of 1 ML thick Ni layer to higher  $O_2$  pressure leads to the formation of a new 2D NiO film, which is named after its complex  $(2\sqrt{3}\times 2)$ -*rect* surface symmetry. The overlap between this thin oxide film and the Rh substrate gives rise to the formation a superlattice with a rectangular unit cell (hence *rect*). The LEED pattern of this surface is reported in fig. 4.1d, where several extra diffraction spots are visible due to the presence of three rotationally non-equivalent lattice domains (indicated by the differently colored dashed rectangles). Furthermore, it can be easily noticed that this LEED pattern is characterized by some missing spots (marked by red circles) along the crystal axes of the Rh(111) substrate. Missing diffraction spots are typically found in the presence of glide symmetry elements in a surface structure. Indeed, this turned out to be the case also for the Ni oxide phase, as proved by the STM surface topographic images shown in the same figure. In fact, the NiO lattice forms a series of zig-zag rows along just one border of the  $(2\sqrt{3}\times 2)$ -*rect* cell. As it can be observed in the bottom graph of fig. 4.1e, the  $Ni2p$  spectrum of the oxide is almost completely different from that of metallic Ni, and many new spectral components are visible. Interestingly, even though the Ni coverage is very low in the present case, the XPS spectrum is very similar to that of

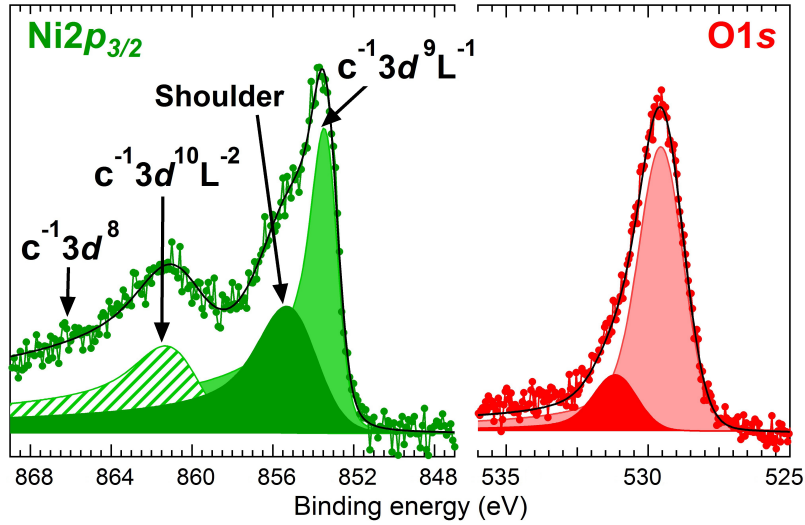


**Figure 4.2:** The XPS  $\text{Ni}2p_{3/2}$  and  $\text{O}1s$  core level spectra of the 2D NiO acquired at 1486.6 eV photon energy. The different components obtained from the spectral deconvolution are shown superimposed.

bulk NiO. In order to get a better understanding of the spectral components originated by this system, let's take a closer look at the  $\text{Ni}2p_{3/2}$  core level component, which is displayed on the left side of fig. 4.2. The corresponding  $\text{O}1s$  core level spectrum, together with its deconvolution into the individual core level components, is shown on the right side of the same figure. In comparison with the  $\text{O}1s$  spectrum measured under the O chemisorption regime, which presents a single peak as will be described in section 4.4, the core level spectrum associated to the quasi-2D oxide film needs to be deconvoluted with two components with a BE separation of 1.6 eV. As will become clearer in section 4.5, these chemically shifted components can be attributed to two geometrically non-equivalent O species.

The complexity of the strongly correlated NiO system becomes evident when looking at the left graph of fig. 4.2, in which at least 4 spectral components can be identified in the  $\text{Ni}2p_{3/2}$  core level spectrum. This is why, although the debate on the origin of this spectrum has gone on for decades, a universally accepted theoretical model which accounts both for the origin of the NiO XPS components and for their line-shapes is still missing. NiO is known as a charge transfer oxide whose ground state is strongly influenced by the hybridization between the  $3d^8$  and the  $2p$  state of the O ligand [16,17]. Moreover, it is generally assumed that its initial ground state is defined as a combination of  $3d^8$ ,  $3d^9L^{-1}$  and  $3d^{10}L^{-2}$  states, where  $L^{-n}$  represents the donor ligand. The different terms lead to a Ni final state in which zero, one or two electrons, respectively, are transferred from the ligand band [17,18]. Accordingly, the possible final states of the interacting electrons system (i.e the system formed by the core-hole plus a quasiparticle) generated by photoemission from the  $\text{Ni}2p$

subshell, are the  $c^{-1}3d^8$ ,  $c^{-1}3d^9L^{-1}$  and  $c^{-1}3d^{10}L^{-2}$  states, where  $c^{-1}$  represents the core-hole creation as before. The deconvolution of the XPS spectrum into the different final state contributions is shown on the left side of fig. 4.2, where the different components have been labelled accordingly. (The  $c^{-1}3d^8$  component has not been included in the deconvolution because it appears as a very broad feature which could not be well localized with our energy resolution.) Due to the strong correlation among  $d$ -electrons, final state effects lead to a dramatic modification of the electronic state energies. In fact, the creation of a  $2p$  core-hole at a Ni atom is always accompanied by a strong Coulomb repulsion with the holes in the localized  $3d$  orbitals, which increases the total energy of the system. The main effect of charge transfer to the  $3d$  orbitals is a screening of this Coulomb repulsion, with a subsequent reduction of the corresponding final state energy. This is the reason why the unscreened  $c^{-1}3d^8$  state is found at higher BE with respect to the states characterized by a charge transfer from a ligand atom to the  $3d$  orbitals. Nevertheless, the  $c^{-1}3d^9L^{-1}$  final state has a lower BE than the  $c^{-1}3d^{10}L^{-2}$  state, owing both to the smaller  $d$ - $d$  electron repulsion and to the lower energy cost of transferring 1 instead of 2 electrons from the ligand to the  $d$  shell [19].

While the electronic structure of these components has been theoretically and experimentally solved, the origin of the “shoulder” at 1.6 eV higher BE with respect to the main component (dark green peak in fig 4.2), is still controversial [20–23]. The most widely accepted interpretation attributes this shoulder to an additional *non-local screening* process from the neighboring octahedral  $NiO_6$  clusters. In this model, the main component is originated by a charge transfer from one of the nearest neighbor O atoms to the Ni site, which leads to a screening of the above-mentioned Coulomb repulsion (*local screening* effect). By contrast, the shoulder at higher BE is ascribed to a *non-local screening* mechanism, in which the extra-electron is transferred from a second-nearest neighbor O atom, thus raising the energy cost of the process (hence this state has a higher BE). Finally, the  $c^{-1}3d^{10}L^{-2}$  component in this picture is generated by the screening effect produced by a double CT from next-to-nearest neighbor ligands, while the larger Gaussian width of this satellite peak is explained with the formation of oxygen bands [16]. Actually, the non-local screening is not the only mechanism responsible for the shoulder on the high BE side of the main component. In fact, both theoretical and experimental evidence has been proved that a large contribution comes also from surface effects. Due to the reduced local atomic coordination to the nearest neighbors at the surface, distinct screening mechanisms (from those observed in the bulk) can be expected. In fact, theoretical simulations of the XPS spectrum have shown that the high BE shoulder of the  $c^{-1}3d^9L^{-1}$  component receives a larger contribution from the surface-like  $NiO_5$  clusters than from the bulk-like  $NiO_6$  clusters [20]. In addition, photoemission measurements have revealed an unambiguous dependence of the intensity of both the main component and its high BE shoulder on the photoemission angle [21]. In summary, two main effects contribute to the appearance of the high BE shoulder of the main  $Ni2p$  core level component: the first is the non-local screening of the  $c^{-1}3d^9L^{-1}$  final state, the second is the

contribution from surface states.

### 4.3.2 Oxidation of $\theta_{\text{Ni}} \geq 2$ ML Ni films

In this subsection I'm going to discuss the ordered phases formed upon oxidation of epitaxial Ni films with a thickness ranging between 2 and 5 ML. The exposure of these Ni films to an  $\text{O}_2$  pressure of  $5 \times 10^{-8}$  mbar (15 L), leads in all cases to the formation of an ordered  $p(2 \times 2)\text{-O}$  phase, which is clearly visible in the LEED patterns of panels b) and c) of fig. 4.3. In panel a) is reported an STM image of the  $(2 \times 2)\text{-O}$  phase formed on a 3 ML thick Ni(111)-like film, which is characterized by large domains. Actually, the  $p(2 \times 2)\text{-O}$  structures shown in the two LEED patterns are slightly different. In fact, depending on  $\theta_{\text{Ni}}$ , the lateral lattice parameter of the Ni overlayers changes. This is a well-known phenomenon observable during epitaxial film growth: if the difference between the lattice constants of the substrate and the adatoms in the corresponding bulk phase is small, at low coverage the adatoms tend to form a quasi-pseudomorphic adlayer with the same lattice constant of the substrate. It is called quasi-pseudomorphic because its formation is strongly affected by lattice strain effects arising during the Ni layer growth, which can induce adatom clustering, misfit dislocations and interface reconstructions [24–27]. In fact, the submonolayer Ni deposition on Rh(111) has been observed to induce either film dislocations or the formation of triangular clusters rather than of homogeneous Ni monolayers [28]. In spite of structural defects, when the Ni coverage increases, the epitaxial Ni films can grow to form large, uniform islands, which is indeed what we observed in our case. Moreover, as will be explained in section 4.4, a stress relaxation can take place once a critical thickness has been reached, thus leading to the formation of a bulk-like Ni(111) film [29]. The two  $p(2 \times 2)\text{-O}$  phases observed at a  $\theta_{\text{Ni}}$  of 3 and 5 ML, in fact, form upon O chemisorption on two Ni films having the lattice parameter of Rh(111) and of Ni(111), respectively. This is proved by the fact that, while in the LEED pattern shown in b) we can only recognize the  $(1 \times 1)$  periodicity of the Rh substrate (black) and the  $(2 \times 2)$  periodicity of the O phase (blue), in (c) some low intensity extra-spots (red) can be observed outside the circle formed by the spots of the  $(1 \times 1)$  Rh lattice; these spots reflect the symmetry of the Ni(111) lattice. In addition, the distances of the fractional  $(\pm \frac{m}{2}, \pm \frac{n}{2})$  spots from the  $0^{\text{th}}$  order spot are different in panels b) and c), thus indicating a different lattice parameter of the Ni film beneath. When a higher  $\text{O}_2$  pressure is used for Ni oxidation, namely  $5 \times 10^{-7}$  mbar, two NiO phases show up at a  $\theta_{\text{Ni}}$  between 2 and 5 ML. In particular, at a Ni coverage lower than 5 ML, the surface displays the geometry of the [100]-terminated Ni oxide phase, superimposed to the periodicity of the  $(2 \times 2)\text{-O}$  phase. In fact, the LEED pattern in fig. 4.3e clearly exhibits diffraction spots reflecting the symmetries of both the  $(2 \times 2)\text{-O}$  phase (blue) and the NiO(100) lattice (cyan). The latter, in addition, comes in three rotationally non-equivalent domains, as indicated by the three cyan squares. While the [100]-terminated NiO can be easily obtained by oxidation of Ni films with a thickness between 2 and 5 ML, the close-packed NiO structure was observed only at 5 ML Ni coverage. Furthermore, despite their low

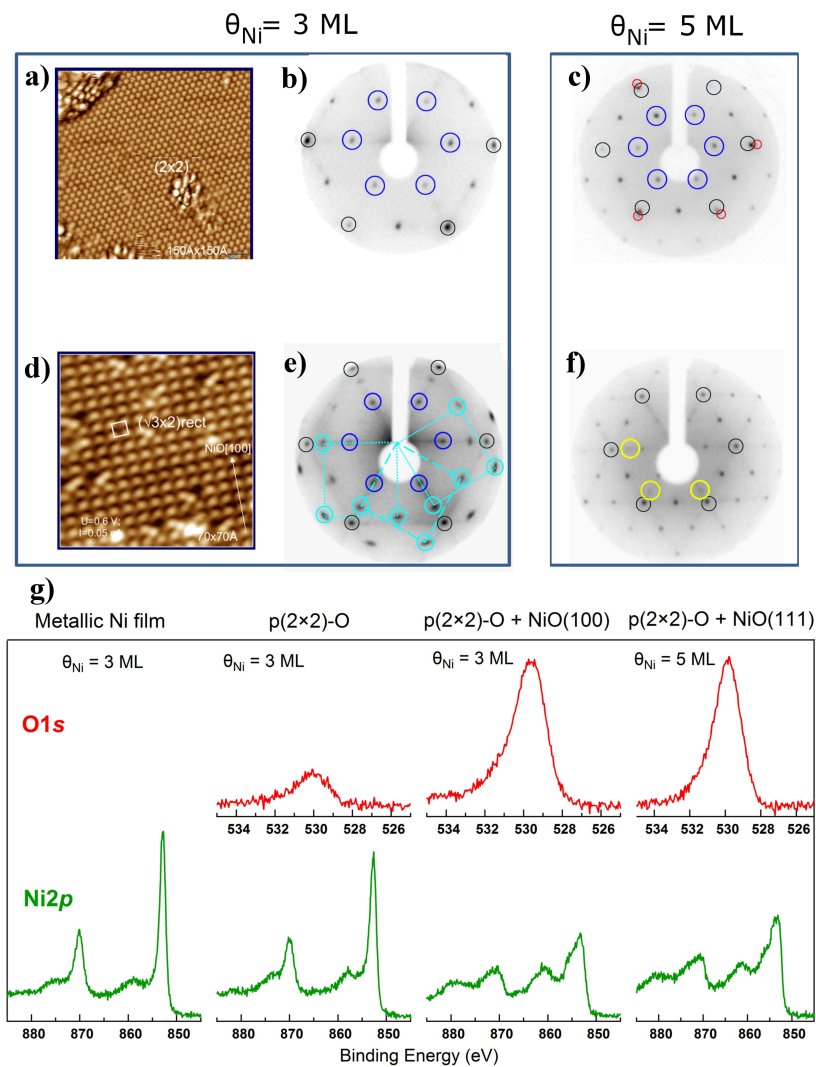


**Figure 4.3:** a) and b) show the STM image ( $U = 200$  mV,  $I = 0.2$  nA) and the LEED pattern ( $E = 59$  eV) of the  $p(2 \times 2)-O$  phase (blue circles) formed after the oxidation of a 3 ML thick Ni film c) LEED pattern corresponding to the  $p(2 \times 2)-O$  phase (blue) formed on a 5 ML thick Ni film, where the red circles highlight the diffraction spots from Ni(111) overlayers. Panels d) and e) display an STM image ( $U = 0.6$  V,  $I = 0.05$  nA) and a LEED pattern ( $E = 59$  eV) of the NiO(100) phase (cyan) at  $\theta_{Ni} = 3$  ML. In the latter, the  $p(2 \times 2)$  phase is also visible, and the squares indicate three rotationally non-equivalent domains. The LEED pattern in f) is characterized by the appearance of the NiO(111) phase (yellow) at  $\theta_{Ni} = 5$  ML. The  $O1s$  and  $Ni2p$  core level components of these three phases are reported in g), where the metallic Ni spectrum is reported as a reference.

intensity, the extra-spots highlighted in yellow in fig. 4.3f can be ascribed to the formation of a new oxide phase. This surface oxide probably corresponds only to the initial stage of the NiO(111) growth on Rh(111). Also the coexistence of both the oxide phases could not be ruled out. Since the NiO(111) lattice has the same in-plane symmetry as the Rh(111) substrate, one would expect a lower energy barrier for the formation of this phase than for the growth of NiO(100). However, the observation of the (100)-oriented NiO phase before the formation of the NiO(111) layer is well documented in the case of bulk Ni oxidation [30,31]. Two explanations have been proposed for this behavior. The first one attributes the easier formation of NiO(100) observed upon oxidation to the smaller lattice strain affecting this phase with respect to the NiO(111) phase. This hypothesis is suggested by the smaller lattice constant difference between NiO(100) and Ni(111) (0.34 Å) compared to the one between NiO(111) and Ni(111) (0.51 Å). The second possible explanation is related to the lower formation energy of the NiO(100) phase relative to NiO(111). In fact, the rocksalt structure of bulk NiO is characterized by alternating cationic and anionic atomic layers stacked along the [111] direction. Hence, repulsive electrostatic forces are expected to arise between adjacent atomic planes, which would reduce the stability of this phase with respect to the non-polar NiO(100) (which instead has both cations and anions within a lattice plane). This is further supported by the experimental observation of the  $(2\times 2)$  surface reconstruction of NiO(111), due to the energetic instability of the polar phase [31].

The XPS spectra measured for the three ordered surface phases described above are displayed in fig. 4.3g, where the O1s core level spectra are reported in the top row, while the Ni2p core level spectra are shown in the bottom row. After the deposition of 3 ML Ni, the Ni2p core level spectrum exhibits the features of metallic Ni, with the characteristic satellite structure on the high BE side of the main component, as visible in fig. 4.3 on the left. The line-shape and BEs of the Ni2p core level components are unchanged after O chemisorption and the subsequent formation of the  $p(2\times 2)$ -O phase. The formation of NiO, on the other hand, leads to a dramatic change of both the O1s and the Ni2p core level spectra. In fact, a significant increase of the photoemission intensity from the oxygen core levels can be clearly noticed, which is a clear sign of the appearance of the oxide phase. Furthermore, the increased intensity of the O1s core level signal most probably indicates the presence of subsurface O species, which is directly related to the surface metal-to-oxide phase transition. Concerning the Ni2p core level, the characteristic spectra of oxidized Ni are reported on the bottom right of fig. 4.3g. An interpretation of their multiple components and complex line-shapes has already been discussed in the previous section.

#### 4.4 Structure of the $p(2\times 2)$ -O phase $\theta_{\text{Ni}} = 5$ ML

Among the  $p(2\times 2)$ -O phases observed at different Ni coverage values, we chose to investigate the structure formed by the chemisorption of 0.25 ML O on Ni

overlayers with a thickness of 5 ML. We chose it because, as already mentioned, in our Ni/Rh bimetallic system 5 ML corresponds to the critical coverage at which the Ni film becomes sufficiently thick to allow strain relaxation. This process consists of a gradual modification of the Ni lattice parameter when moving from the interface layer to the surface. In fact, as already discussed before, the topmost Ni layer is observed to display the same lattice constant of the corresponding bulk phase ( $a_{\text{Ni}} = 2.46 \text{ \AA}$ ), owing to the relaxation of the tensile strain generated by the lattice misfit at the interface. On the other hand, due to its quasi-pseudomorphic structure, the Ni layer found at the interface assumes the lattice constant of Rh(111) ( $a_{\text{Ni}} = 2.69 \text{ \AA}$ ). This is indeed one of the factors that determine the stability of the Ni film on the Rh substrate. In order to work out the structure of the  $p(2 \times 2)\text{-O}$  phase, two main aspects were considered: the O-induced Ni surface layer buckling and the mechanism with which lateral strain is released in going from the interface to the film surface.

#### 4.4.1 XPD data and simulation details

A set of XPD data of this structure was collected for both the  $\text{Ni}2p_{3/2}$  and  $\text{Rh}3d_{5/2}$  core levels. The  $\text{Rh}3d_{5/2}$  core level spectrum shows barely metallic features with no extra-components or BE shifts. The main characteristics of the corresponding XPD pattern are similar to those found in the XPD pattern of bulk Rh(111), just with a wider broadening of the diffraction features [32]. The three-fold azimuthal symmetry with the same symmetry axes can be clearly recognised in both the experimental XPD patterns shown in fig. 4.4. This observation further corroborates our previous conclusion that Ni overlayers have a similar lattice parameters to that of Rh(111). By comparison with other XPD patterns acquired in the forward scattering geometry under similar experimental conditions, the smaller modulation amplitude and the angular broadening of these two experimental patterns suggest that the Ni adlayer is affected by structural inhomogeneities, such as lateral relaxation effects, point defects, dislocations, and a strain-induced buckling. These effects could significantly reduce the coherent interference of the photoelectrons, thus suppressing the corresponding signal intensity modulations. Owing to the very low O coverage associated to this phase, and to the small photoionization cross-section of the  $\text{O}1s$  core level at a photon energy of 1486.6 eV, our sensitivity to the O atoms was very low. This is why we did not acquire the XPD data of the  $\text{O}1s$  core level.

On the basis of the LEED and STM results discussed before, an atomic cluster formed by 5 Ni layers with fcc(111) stacking was chosen for the simulation of the theoretical XPD patterns. Atomic O chemisorption on Ni(111) has been widely studied in literature. It has generally been found that O atoms adsorb preferentially in the three-fold hollow sites, thus inducing a local reconstruction of the Ni surface layer [33,34]. Therefore, in the preliminary, unrelaxed structure the O atoms were fixed in hollow sites. A schematic representation of our structural model is displayed in fig. 4.5, in which the small red spheres represent the O adatoms, while the green and the blue ones indicate the atoms of the Ni and Rh layers, respectively. The underlying structural parameters of this system

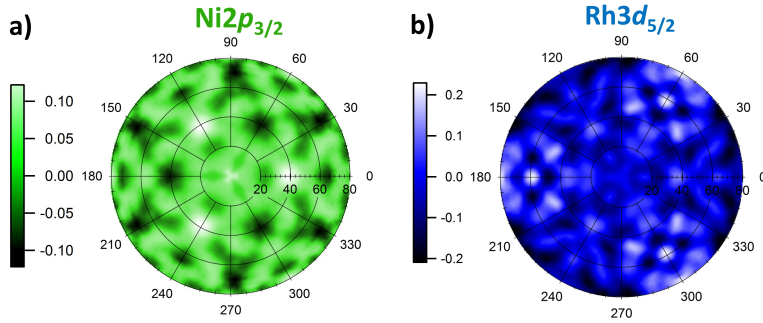


**Figure 4.4:** Experimental XPD patterns of the  $\text{Ni}2p_{3/2}$  (a) and of the  $\text{Rh}3d_{5/2}$  (b) core levels.

are indicated in panel b), and all of them are referred to the Ni adlayers. The parameters  $\mathbf{a}_{\text{Ni}1} \dots \mathbf{a}_{\text{Ni}5}$  express the values of the in-plane Ni lattice constants, where Ni5 indicates the interface layer and Ni1 refers to the terminal Ni layer. The interlayer distances within the Ni film are simply indicated by  $\mathbf{d}_{\text{Ni}n-\text{Ni}n+1}$ .

A tricky point for the theoretical simulations was the choice of the lateral size of the simulation cluster. The strain relaxation is reflected in a gradual variation of the in-plane lattice constant from  $\mathbf{a}_{\text{Ni}}$  to  $\mathbf{a}_{\text{Rh}}$ . Therefore, each Ni layer is expected to have a different in-plane lattice parameter, and this determines the incommensurability of the Ni film with respect to the Rh substrate. Consequently, our simulation cluster should be in principle infinitely large in order to include all the non-equivalent Ni and Rh atoms, which is obviously impossible. After a series of tests performed on atomic slabs with dimensions up to  $(24 \times 24)$ -Rh(111) unit cells, we found out that a sufficiently accurate structural model could be obtained by approximating the actual structure with a smaller periodic lattice made of  $(13 \times 13)$ -Ni(111) unit cells. Four bulk Rh layers formed by  $(12 \times 12)$ -Rh(111) unit cells were included in the simulation cluster. In this way, our simulations were performed on a very large atomic cluster, made of 845 Ni atoms, 36 O atoms, and 576 Rh substrate atoms. The  $\text{Rh}3d_{5/2}$  XPD pattern was not included in the subsequent structural optimisation because it would have been overly demanding in terms of computational resources. However, once the best structural model had been obtained, on the basis of the  $\text{Ni}2p_{3/2}$  diffraction pattern only, we simulated the corresponding theoretical Rh pattern for a final check.

The subsequent structural relaxation procedure was carried out following two main directions. The first one is related to the determination of the O-induced rippling effect of the surface Ni layer (Ni1). The second one concerns instead the identification of the strain relaxation mechanism across the Ni adlayers.

#### 4.4.2 O-induced Ni surface buckling

Owing to the high Ni-O interaction strength in the  $p(2 \times 2)$ -O phase formed on bulk Ni(111), this crystal surface is known to undergo an oxygen-induced

reconstruction. In fact, the bonds between the three Ni atoms (dark green in fig. 4.5) and the central O atom to which they are directly coordinated are laterally stretched and twisted (as indicated by the arrows in panel (c)), and the Ni atoms around the central O site are correspondingly buckled upwards [33,34].

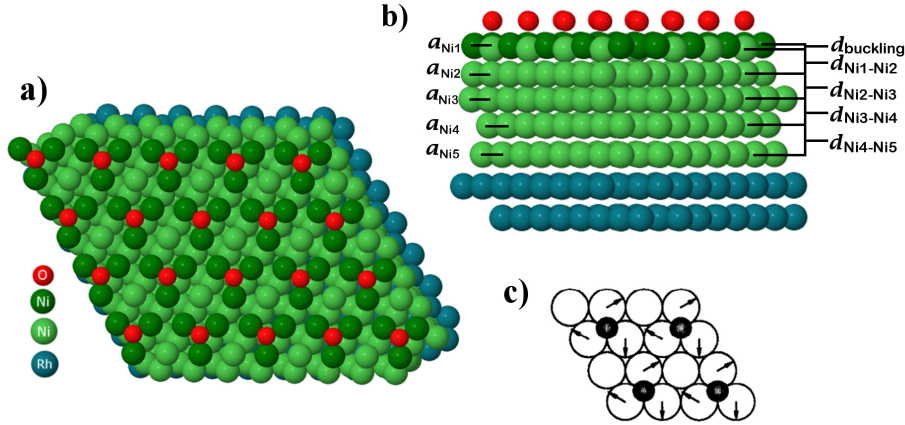


**Figure 4.5:** A top (a) and side (b) view of the structural model for the 5 ML  $p(2\times 2)$ -O phase. (c) Schematic representation of the Ni(111) bulk phase formed by O adsorption [33].

However, the  $p(2\times 2)$ -O phase formed on an epitaxial Ni thin film is slightly different from that observed in the bulk case. In fact, while a surface buckling was also evidenced by our XPD analysis of the  $\text{Ni}2p_{3/2}$  core level modulation function, the twisted in-plane lattice expansion was absent in the Ni(111) thin film surface. This XPD result is additionally corroborated by the fact that the simulations performed on a structural model including both effects (the Ni layer buckling and the lateral expansion) yielded a larger R-factor (0.40) than the simulations carried out by taking into account only the out-of-plane buckling (0.36). Anyway, both these model reconstructions showed a better agreement with the experimental XPD data with respect to the unreconstructed flat Ni surface (which yields an R-factor of 0.41). In addition, the Ni thin film displayed an outward displacement of  $0.23 \pm 0.15 \text{ \AA}$ . Though it is larger than the value found for the corresponding bulk phase ( $0.12 \text{ \AA}$ ) [33], still can be considered acceptable when our experimental error bar is considered. This surface buckling is clearly visible in our final structural model shown in fig. 4.5a,b.

Although we have not yet optimized the Ni film lattice parameters, we have unequivocally proved the presence of a surface rippling effect, similar to that observed for the corresponding bulk reconstruction. It is difficult to explain why the thin film surface reconstruction is different from the bulk counterpart. However, this structure is certainly affected by the lattice strain experienced by all the Ni adlayers underneath the topmost layer.

In-plane lattice constants		Out-of-plane distances	
$\mathbf{a}_{\text{Ni}1}$	2.49 (fixed)	$\mathbf{d}_{\text{buckling}}$	$0.23 \pm 0.15$
$\mathbf{a}_{\text{Ni}2}$	$2.51 \pm 0.02$	$\mathbf{d}_{\text{Ni}1n-\text{Ni}2}$	$1.70 \pm 0.20$
$\mathbf{a}_{\text{Ni}3}$	$2.54 \pm 0.03$	$\mathbf{d}_{\text{Ni}2-\text{Ni}3}$	$1.70 \pm 0.20$
$\mathbf{a}_{\text{Ni}4}$	$2.57 \pm 0.03$	$\mathbf{d}_{\text{Ni}3-\text{Ni}4}$	$1.80 \pm 0.30$
$\mathbf{a}_{\text{Ni}5}$	2.69 (fixed)	$\mathbf{d}_{\text{Ni}4-\text{Ni}5}$	$2.00 \pm 0.50$

**Table 4.1:** XPD result for the in-plane lattice constants and interlayer distances of the p(2×2) phase formed on the 5 ML Ni film. All the values are in Å.

### 4.4.3 Strain relaxation mechanism

Once we had proved the arising of an O-induced film surface rippling, we carried out a rigorous structural relaxation taking into account all the interlayer distances of the Ni film ( $\mathbf{d}_{\text{Ni}n-\text{Ni}n+1}$ ), including the surface buckling and the lattice constants of the intermediate Ni layers ( $\mathbf{a}_{\text{Ni}2}, \mathbf{a}_{\text{Ni}3}, \mathbf{a}_{\text{Ni}4}$ ). At this stage, the values of  $\mathbf{a}_{\text{Ni}1}$  and  $\mathbf{a}_{\text{Ni}5}$  were kept fixed to  $\mathbf{a}_{\text{Ni}}$  and  $\mathbf{a}_{\text{Rh}}$ , respectively. The final result of our R-factor minimization process is reported in tab. 4.1, which shows a best R-factor of 0.23.

Besides the large surface buckling, we also found a significant compression of the top three layers in comparison with the interlayer distance of the Ni(111) bulk phase (2.01 Å). The large error bars affecting these values reflect our limited sensitivity to the vertical positions of these Ni layers, which is probably caused also by an inhomogeneous film growth (Ni films with different thickness could exist) and by the presence of domain boundary dislocations. On the contrary, thanks to the large atomic clusters used in our simulations, we are very sensitive to variations of the in-plane distances, whose estimated values are correspondingly affected by much smaller error bars. In this case, in fact, even a tiny lateral lattice displacement at the origin of the cluster (e.g. 0.01 Å) can lead to a large shift (up to 0.22 Å) of all the atoms away from the origin. This displacement can therefore result in a variety of non-equivalent new local configurations, which is reflected in a significant modification of the experimental XPD patterns. Since XPD is basically a local probe technique, all these local effects can be adequately taken into account in the analysis. Therefore, the accurate determination of the lattice constants allowed us to identify the mechanism with which the tensile strain accumulated in the Ni lattice is released along the direction normal to the surface: the in-plane lattice parameter of the Ni film is exponentially reduced in going from the interface region to the film surface.

In order to cross-check the correctness of our results, a quantitative comparison between the exponential decay mode and other two possible strain relaxation mechanisms is reported in fig. 4.6a)–e). The three different behaviors are schematically represented in panel b). On the  $x$ -axis is reported the Ni–Rh distance of each Ni adlayer from the substrate, where the lattice parameter of the bottom layer has been fixed to 2.69 Å, while that of the topmost layer has a value of 2.49 Å. The black-dotted curve, labelled “constant”, describes a 5 ML

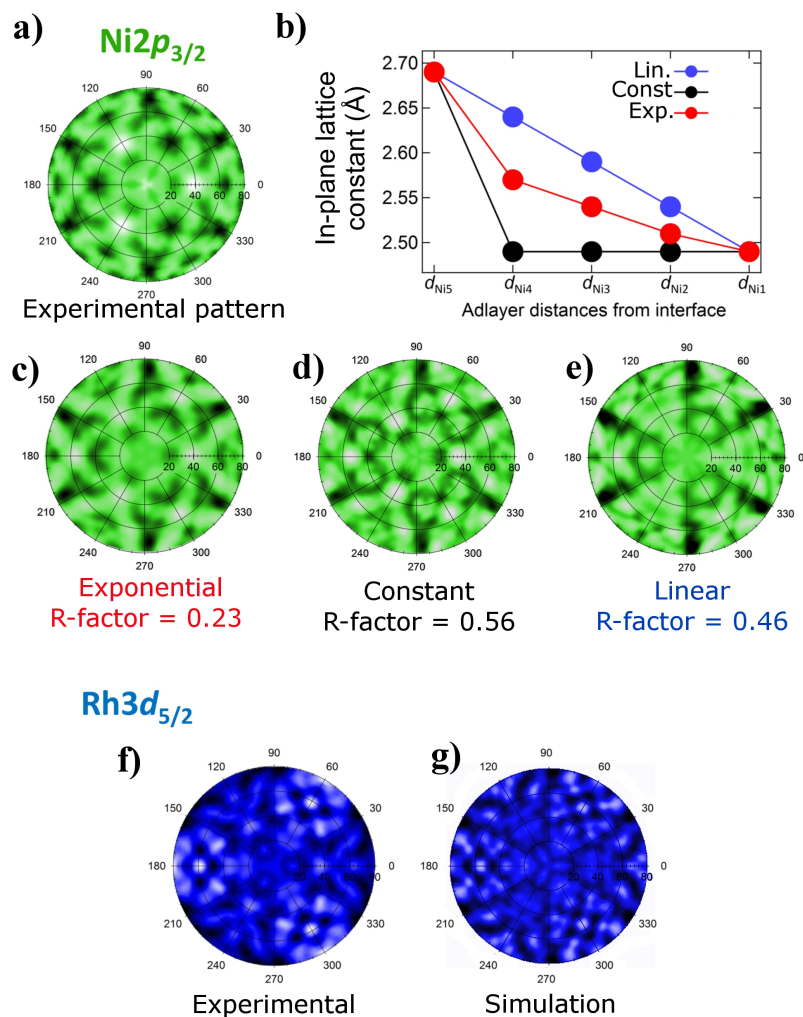


**Figure 4.6:** Comparison of the a) experimental XPD pattern of the Ni2p<sub>3/2</sub> core level and those simulated ones c)–e) obtained for the different strain relaxation modes reported in the plot in panel b). For each of them the corresponding R-factor is indicated. Experimental f) and simulated g) XPD patterns of the Rh3d<sub>5/2</sub> core level. The simulation was carried out on the basis of the structural model obtained from our XPD analysis.

thick Ni film, for which the same lattice parameter of 2.46 Å is found in all layers, except for the interface layer, which has the same lattice constant of Rh(111). Simulations based on this structural model produced the XPD pattern shown in panel d) yielding an R-factor of 0.56. A second strain relaxation mechanism involves a reduction of the lattice constants following the straight blue line in the same graph, and indicated as “linear” mode. The corresponding simulated XPD pattern is shown in e), and returned an R-factor of 0.46. Clearly, both the constant and the linear decay modes can be ruled out due to their much larger R-factor. Finally, also the experimental and the simulated XPD patterns of the

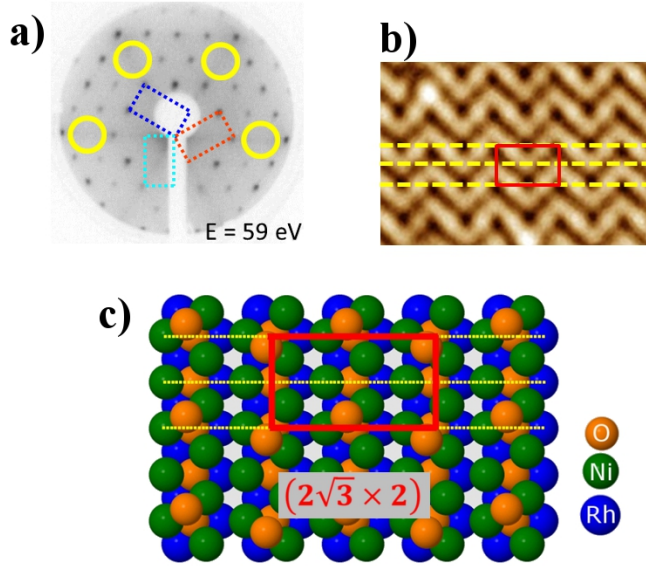


**Figure 4.7:** LEED pattern (a) and STM image (b) of the 2D NiO film formed on Rh(111). c) The preliminary structural model we used as a starting point for our XPD analysis. The orange, green and blue spheres represent O, Ni and Rh atoms, respectively.

Rh $3d_{5/2}$  core level are shown in fig. 4.6f)–g) for a qualitative comparison. It can be noticed that both the patterns show the same main features, but in the experimental one they appear broader. Such a difference is probably originated by the disordering effects caused by the presence of Ni islands with different size and orientations, which are visible in the experimental XPD features, but not all of them could be taken into account in the simulations.

## 4.5 The 2D $(2\sqrt{3} \times 2)$ rect-NiO phase

Among the different surface phases observed in this experiment, one of the most interesting phases was the two-dimensional  $2\sqrt{3} \times 2$ -rect Ni oxide already mentioned in section 4.3. In this section I will report both on the results of our XPD investigations and on the strategy we adopted for seeking of the best structural model for this 2D oxide film.

Since this thin oxide film does not form in nature, there is no comparable bulk phase which could suggest us an initial guess for the structural modelling. Therefore, a suitable model had to be built from scratch on the basis of the results of complementary techniques: LEED, XPS and STM. The starting point for our subsequent XPD structural determination was provided by the draft model reported in fig. 4.7c, which includes all the structural information collected in our preliminary analysis. More specifically, we derived the symmetry and the size of the oxide film unit cell from the LEED pattern and from the

STM image shown in this figure. As it is indicated by the red rectangle, the superlattice generated by the overlap between the oxide and the substrate has a rectangular unit cell whose lattice vectors are respectively  $2\sqrt{3}$  and 2 times larger than the Rh lattice constant. This symmetry is also proved by the presence of a set of LEED extra spots with the same periodicity, as shown in panel (a) (the spots are located at the vertices of the rectangles around the  $0^t h$ -order diffraction spot), and by the observation of the same rectangular cell in the STM image of panel (b). In this tentative structural model, the NiO film is formed by an hexagonal Ni layer bonded to O atoms both above and below. The presence of two geometrically non-equivalent O species accounts for the appearance of two distinct components in the O1s core level spectrum shown in fig. 4.2. From a comparison between the integrated areas of the calculated O1s core level spectra of the p(2×2)-O phase and of the oxide, we estimated that the O coverage in this oxide film amounts to 0.75 ML. Considering that the Ni coverage is 1 ML, the Ni:O intensity ratio in the thin film should be 4:3. Therefore, 8 inequivalent Ni atoms and 6 O atoms (4 at the interface and 2 at the surface) were included in the unit cell of the system. In addition, our initial model took into account also the glide symmetry arising from the bright zig-zag features observed in the STM image, which leads to missing spot in the LEED pattern. The yellow dotted lines indicate the glide planes, which are disposed along a single lattice direction of the  $2\sqrt{3} \times 2$ -rect phase. The interface O atoms occupy half of the three-fold hollow sites of the Rh substrate, whereas the terminal O species are found in alternate bridge interstitial sites of the Ni layer, thus generating the observed glide symmetry.

At the high photon energy we used, the Rh atoms of the substrate don't affect significantly with the forward-scattering events involved in the photoemission from the O1s and the Ni2p<sub>3/2</sub> core levels. Therefore, the role of the substrate was neglected in our simulations. Finally, the EDAC code was used in the XPD theoretical calculations, and a custom computational method for data analysis was developed, which will be described in the following.

#### 4.5.1 The *ad hoc* computational method used in XPD

Although our initial structure had been designed in such a way to account for the symmetry and periodicity of the superlattice modelled on the basis of the LEED and STM measurements, we had no clue of the correct inter-atomic or interlayer distances. Therefore, in the initial model we forced the Ni-O distances to be equal to those of bulk NiO, and the value of each structural parameter was allowed to vary within a range given by  $\pm 15\%$  of its starting value. This made the steepest descent algorithm less suited for a direct application in the R-factor minimization process. This algorithm, in fact, would offer a very efficient approach to R-factor minimization only if our initial guess were already close enough to the *global minimum*. This was e.g. the case of both the ultra thin RhO<sub>2</sub> phase, where the initial structure could be predicted on the basis of previous experimental and theoretical findings, and of the p(2×2)-O/Ni(111)/Rh(111) phase, in which we had the bulk structure parameters as a

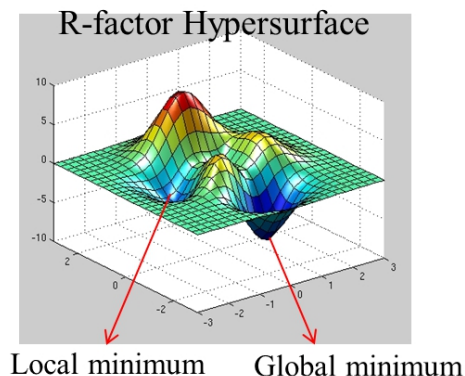


**Figure 4.8:** An example of 2D R-factor hyperspace where a local minimum has been indicated, together with the global minimum. The color scale reflects the value of the R-factor.

reference.

Our R-factor minimization process basically involves a search of the absolute minimum in a multidimensional hyperspace, whose dimensionality is determined by the number of structural variables. Besides the global minimum, the R-factor hyperspace is typically characterized by many local minima. Fig. 4.8 shows a two-dimensional hyperspace in which the global minimum is shown together with a local minimum. The main drawback of the steepest descent method is given by the fact that the algorithm stops as soon as it localizes the minimum closest to the starting point, even if it is just a local minimum. Once a minimum in the hyperspace has been reached, it is not possible to get out of it by using this algorithm. Therefore, local minima behave as traps for a R-factor minimization process based on steepest descent.

In order to avoid this problem, a different computational method is required. To this purpose, we developed a custom approach based on the Genetic Algorithms (GAs), whose great advantage is that it allows hopping between different positions within the R-factor space during the minimization procedure. In this way, even though we may come across a local minimum, there is still a chance to get out of it and to proceed the search from a different configuration [35]. However, the application of GAs to XPD analysis has only recently been proposed, and only in a few cases it has proved successful [36,37]. The main difficulty arises from the lack of a standard procedure applicable to all systems, since the algorithm provides just some general criteria that need to be implemented case by case. Hence, an *ad hoc* method had to be created and tailored for our system. In the following paragraph, I will briefly describe the basic concepts of the GAs we exploited to develop our custom method for XPD analysis. Our method, moreover, combines the strong points of both the Genetic and the Steepest descent algorithms. In fact, while GAs are best suited for seeking a global minimum, they are less efficient in reaching the lowest value of the R-factor once we are in close proximity of the global minimum. This is the reason why the

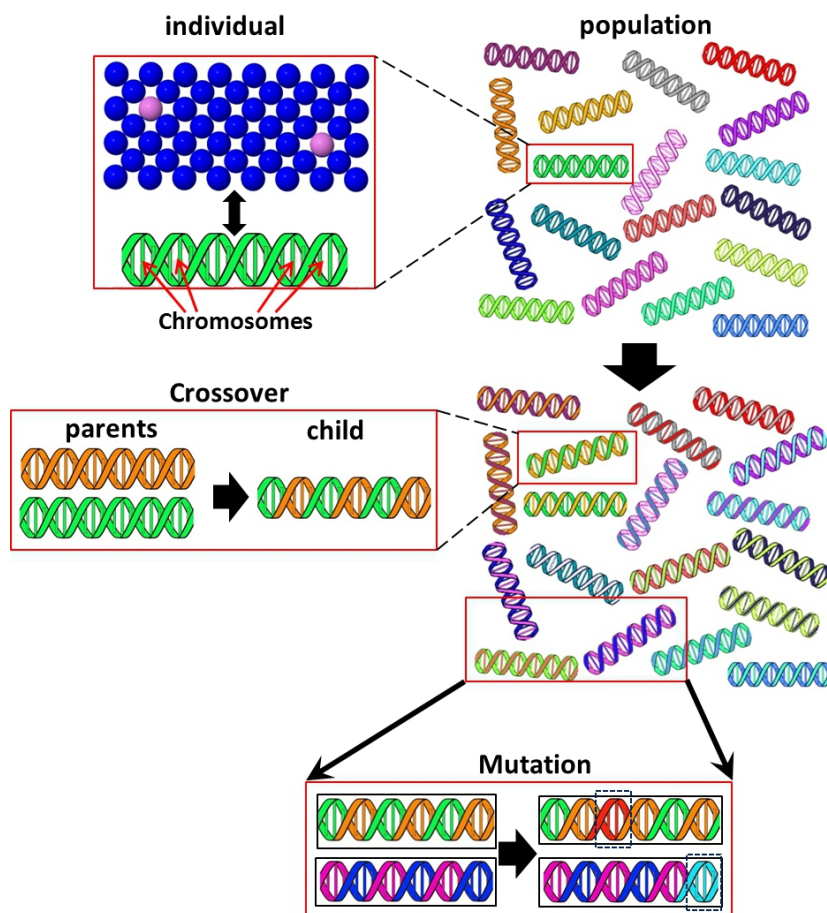


**Figure 4.9:** A pictorial representation of the fundamental quantities and operations involved in Genetic Algorithms. As shown on the top, an individual is univocally defined by its chromosomes, and each set of individuals forms a population. In the center is shown a crossover, which mixes the parents' chromosomes and generates the child's gene pool. On the bottom, two individuals undergo a mutation, which is marked by the appearance of new colors representing new chromosomes.

steepest descent algorithm was locally applied to improve each step of the GA procedure.

GAs form a class of global search methods based on the concept of the evolution of the species. In the same way as living creatures change their characteristics over time to better adapt to the external environment, in our XPD analysis each structural configuration is considered as an *individual*, which is completely defined by a basis set of structural parameters, corresponding to the *chromosomes*. The chromosomes contain all the genetic information pertaining to an individual, and their mutation is responsible for the evolution of that individual. In this picture, the fitness of an individual is evaluated on the basis of its R-factor. Instead of evaluating one configuration at a time, GAs work with *population* of individuals, and search the best one by sorting out different trial

solutions at once. During the GA-based procedure, the individuals are created and modified in such a way to sample the whole parameter hyperspace, which in the present case means exploring the R-factor hyperspace in a quest of the global minimum. The evolution process is carried out iteratively, by applying specific evolutionary operators at each loop. There are three fundamental operators in the GAs, namely *crossover*, *mutation* and *elitism*.

Figure 4.9 gives a schematic representation of the basic concepts of population, crossover and mutation described here. The individuals are represented by chromosomes of different colors, each of which corresponds to a specific configuration present in the initial population. One of the most important operations in GAs is the crossover. Two individuals are chosen from the initial population, and their chromosomes are randomly selected for the creation of a new individual, the child, which inherits the characteristics of both its parents. This is graphically described in the second row of fig. 4.9, where the children of the new generation receive the chromosomes from both their parents (hence they are bicolored). The parents' selection for the crossover is performed as follows. Given an initial population, we calculate the R-factor associated to each individual, then sort out all the individuals and pair them up in couples according to their R-factors. A low R-factor individual will be paired with another low R-factor individual, and similarly the high R-factor individuals will be grouped in couples among them. This selection criterion helps us create new configurations by mixing good genes and avoiding introducing faulty genes in the offspring. After the crossover, the mutation operator is applied to the new generation of children. Once a child is randomly selected, some of its chromosomes are replaced with new elements; which are randomly chosen from a previously defined interval of allowed values according to the specific chromosome. The range of variation for a given structural parameter (i.e. a chromosome) is defined by the largest change allowed for that parameter. This operation is represented on the bottom of fig. 4.9, where each of the mutated individuals contains a new chromosome, symbolized by a third color. During the evolution of a species, mutations plays an important role in introducing new structural characteristics, so that the overall set of the tested configurations will not be restricted by the initial choice. The last operation performed at the end of each GA loop is called elitism, which consists in the actual selection of the species. In this step, the R-factors of the new individuals are recalculated, and the individuals showing the highest R-factors will not survive until the next generation. In addition, they are replaced by the lowest R-factor individual, which represents the best fitting candidate at the present. At this point, our new population has evolved, mutated, and a large part of it has survived to the next generation, for which the same procedure will be applied. This process is iterated until the global minimum is achieved, which is reflected in the fact that the lowest R-factor remains unchanged for more than a certain number of steps, as suggested by ref. [35].

An efficient representation of the GA iterations is given in fig. 4.10, where a schematic flow chart illustrates the sequence of GA operations. As it is reported in this diagram, a rough steepest descent-based local minimization process is

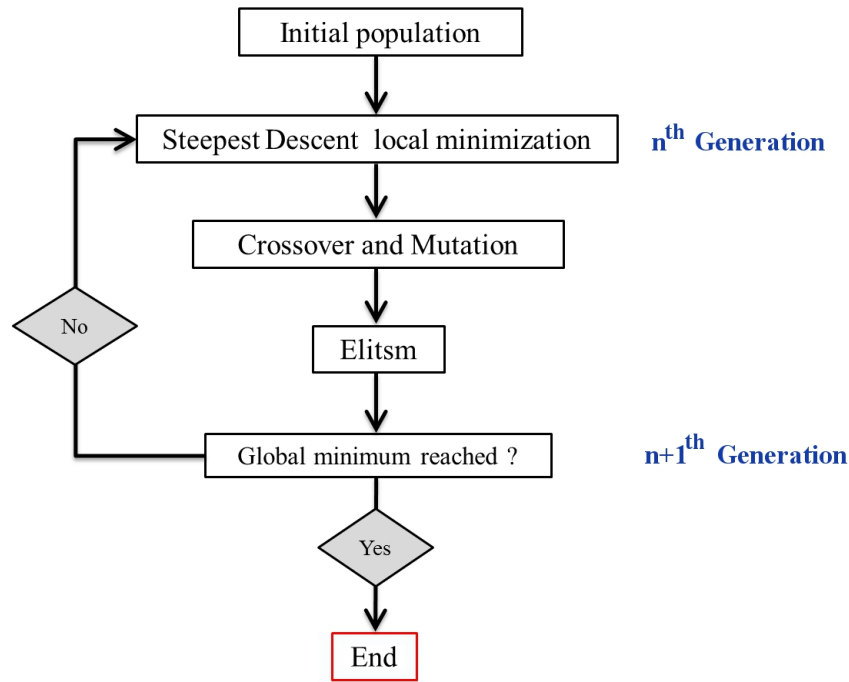


**Figure 4.10:** A flow chart showing our XPD analysis procedure in which the GA operations are combined with local minimization based on steepest descent algorithm.

performed prior to the crossover. This is a strategic choice, which brings all the configurations a step closer to their respective nearest minimum. Hence they become parents with a more successful gene pool before the crossover, in such a way that unnecessary calculations on recessive configurations can be avoided. Finally, once the global minimum has been achieved by means of GA loops, a more accurate steepest descent procedure is applied in order to get down to the bottom of the global minimum dip.

#### 4.5.2 Structure determination of the $(2\sqrt{3} \times 2)$ -*rect* phase

After a series of preliminary trials and considerable computational efforts aimed at automating as much as possible the GA operations and the R-factor calculation, the new XPD analysis method was successfully applied to the structural determination of the  $(2\sqrt{3} \times 2)$ -*rect* superlattice. To this purpose, we identified 12 structural parameters which could unequivocally define every single possible configuration of the oxide film, thus playing the role of the chromosomes of the NiO structure. These parameters are defined in such a way that, whatever large their range of variation is (as long as they keep physically meaningful values), the size of the unit cell and the symmetry of the superlattice previously described will always be preserved. Our tests proved that 26 is the smallest reasonable number of individuals a population of configurations should contain. Each chromosome was allowed to vary within a fixed range of values, and our

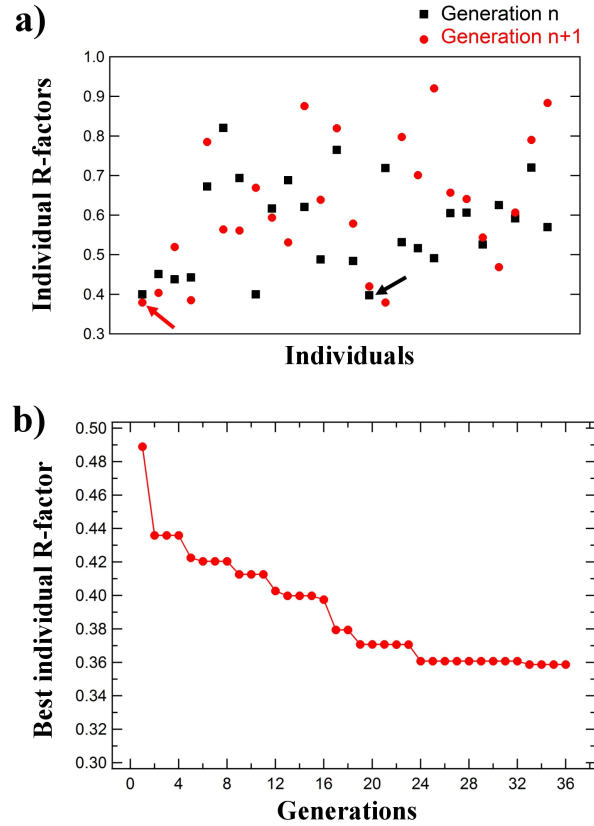


**Figure 4.11:** a) The R-factor distribution of the 26 individuals forming our population of configurations at generation  $n$  (black) and at generation  $n+1$  (red). The arrows indicate the best individuals with the lowest R-factor. b) The decrease in the R-factor of the best individual is shown as a function of the iteration number.

initial population was formed by individuals obtained by randomly varying the 12 chromosomes describing the structure shown in fig. 4.7c.

The results of this new approach are reported in fig. 4.11. Panel a) of this figure reports on the R-factor distributions of the 26 individuals of two successive generations, in which the  $(n+1)^{th}$  generation was obtained from the  $n^{th}$  one by applying a rough local minimization procedure, followed by crossover, mutation and elitism. The two arrows indicate the two best individuals of each population, and the lowest R-factor obtained for the  $(n+1)^{th}$  generation (indicated by the red arrow) is indeed smaller than that found for the  $n^{th}$  generation (indicated by the black arrow). Thus, our population is self-consistently improved at every evolution step, until it finally approached the global minimum. Though the individuals of the  $(n+1)^{th}$  generation have inherited their parents' genes, they are genetically distinguishable from their parents due to the chromosome mixing. This explains why individuals belonging to two different generations show distinct R-factors. The only exception in this case was given by the individual with the lowest R-factor in the  $n^{th}$  generation, which has been cloned during the elitism operation

into the  $(n + 1)^{th}$  generation.

The evolution of the R-factor of the best individual at each iteration is reported in fig. 4.11b as a function of the generation number. A clearly decreasing trend of the minimum R-factor is visible from the plot, and it gradually slows down as we approach the global minimum in the R-factor hyperspace. Starting from our initial population, our search ended after 36 evolution steps, once no further decrease in the R-factor was observed. In 36 GA steps, we evaluated a total of 936 structural configurations, which were randomly chosen in such a way to sample the whole parameter space. This procedure led us close to the global minimum in the end. At this point, a steepest descent local structural refinement was performed starting from the best configuration achieved by GA-based method. This further improved the R-factor, owing to the smaller parameter adjustments involved in the steepest descent minimization with respect to the previous procedure. In fact, the sensitivity of the GA approach to the structural parameters is limited by the size of the random steps chosen, which should be not too small in order to cover the whole parameter space.

The simulated XPD patterns of both the O1s core level associated to the interface O layer and of the Ni2p<sub>3/2</sub> core level, as obtained by retaining the best fitting individual, are reported in fig. 4.12(a), together with the corresponding experimental ones. In panel (b) is also illustrated a comparison between the initial and the final structural model. A significant R-factor improvement was achieved by using our combined GA and steepest descent algorithm. In fact, while the initial structure results in a R-factor of 0.49, the best individual shows a value of 0.31. The blue triangles help to understand the local geometrical rearrangement that yielded the best agreement. The two pairs of triangles in the initial guess structure and in the final best structure have clearly distinct shapes, the former is close to an equilateral triangle, while the latter has one angle much narrower than the others. This is generated mainly by two types of local structural modifications. The first consists of an inward bond contraction of the two Ni atoms coordinated to the terminal O layer; at the same time, these Ni atoms are also lifted upwards due to the Ni-O bonding. The Ni layer buckling can be clearly observed in the side view of fig. 4.12b, as indicated by the cyan rectangles: the two Ni atoms bond to the same terminal O atom above reduce their in-plane distance, and are raised relative to the rest of the Ni lattice. The second structural rearrangement arises from the in-plane displacement of the terminal O atoms from a perfect bridge site to a site halfway between bridge and hollow.

One of the driving forces which lead to such a local structural rearrangement is certainly the strong Ni-O bonding. Instead of the 2D NiO film proposed in the initial structure, the final NiO layer resembles a series of quasi-1D NiO rows, owing to the shrinking of the Ni atoms close to the O atoms. This new arrangement is characterized by NiO rows orthogonal to the glide planes, as visible in the optimum structural model of fig. 4.12b. On the other hand, the lateral displacement of the terminal O atoms is probably due to the Coulomb repulsion between the two O atoms above and beneath the buckled Ni pair. This

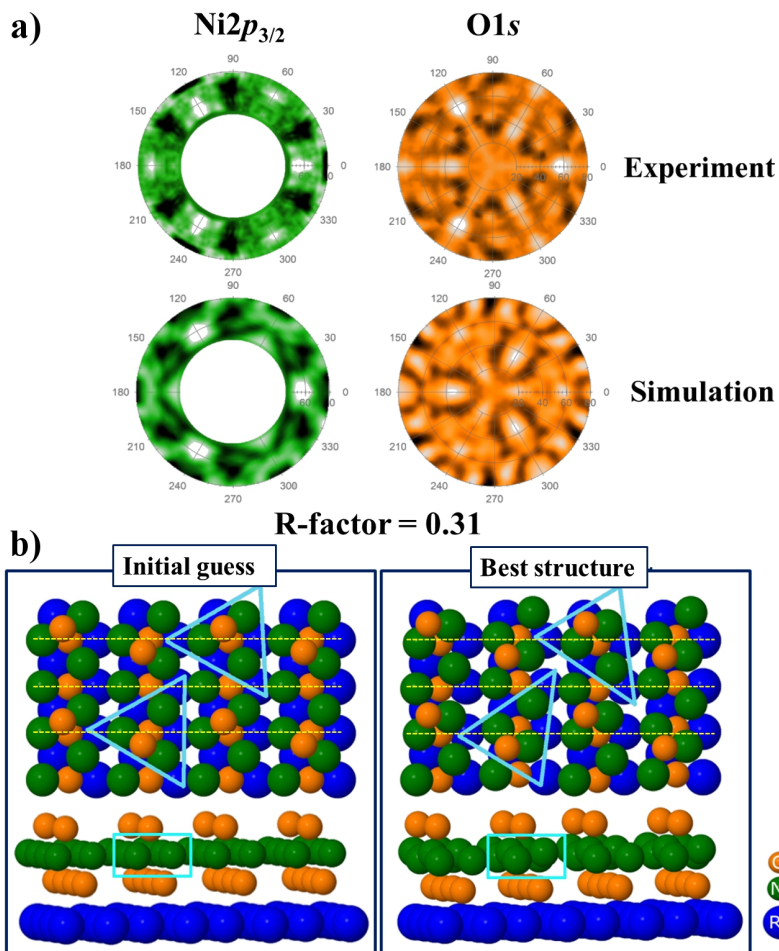


**Figure 4.12:** (a) The experimental and best simulated XPD patterns of the O1s and Ni2p<sub>3/2</sub> core levels are reported together with the total R-factor, which amounts to 0.31. (b) 3D models of the supported NiO thin film before (left) and after (right) structural relaxation. The colored rectangles and triangles highlight the principal differences between the two models.

interpretation is supported by the fact that a more homogeneous distribution of the O–O distances is visible in the final structure compared to the initial guess model. As a final cross-check, we observed that the Ni–O bond lengths obtained from our XPD analysis range from 1.98 to 2.34 Å, which perfectly match the Ni–O distances commonly found in literature for various Ni–O based compounds (1.78–2.55 Å) [38–40].

## 4.6 Conclusions

This chapter reports on a thorough characterization of the low-dimensional structures obtained from the post-oxidation of ultra-thin Ni films supported on Rh(111). Epitaxial Ni overlayers were grown at different film thickness. Distinctive 1D and 2D NiO films were detected to form at monolayer and sub-monolayer Ni coverage, namely the  $p(6\times 1)$  and the  $(2\sqrt{3}\times 2)$ -*rect* oxide phases. At a higher film thickness, in the range 2–5 ML, ordered hexagonal Ni(111)-like overlayers were observed to form, on which a  $p(2\times 2)$ -O phase was seen to grow upon oxygen chemisorption. The analysis of the LEED patterns of the surfaces allowed us to find out that 5 ML is the critical Ni coverage at which the Ni adlayers completely release the lattice strain built up during film growth. This conclusion was born out by the observation of the  $(1\times 1)$  diffraction spots generated by both the bulk-like Ni(111) and by the Rh(111) lattice periodicities. Starting from these qualitative results, the lattice strain relaxation mechanism was determined by means of XPD analysis. We proved that the Ni film releases its lattice strain by gradually reducing its lattice parameter in moving from the interface to the film surface following an exponential trend.

After a preliminary analysis based on LEED, STM and XPS measurements, we focused our XPD structural investigations on the  $(2\sqrt{3}\times 2)$ -*rect* phase, which is an actual 2D oxide. In this respect, an *ad hoc* method for XPD analysis was implemented, which combines the strong points of both the steepest descent algorithm and the genetic algorithms. This novel approach to the R-factor minimization proved particularly suitable for the investigations of complex structures. For example, the supported 2D NiO thin films surely represent one of such complex systems, whose R-factor hyperspace is indeed characterized by the presence of many local minima. By using this custom method, the structural determination of the  $(2\sqrt{3}\times 2)$ -*rect* phase was successfully carried out.

In addition, a consistent interpretation of both the metallic and oxidized Ni2*p* core level XPS spectra has been provided throughout this chapter, which has once more revealed the extreme complexity of the electronic structure of both the bare transition metal and of the charge-transfer Ni oxide.

---

## References

- [1] Chambers, S. A. *et al.* Ferromagnetism in oxide semiconductors. *Mat. Today* **9**, 28 (2006).
- [2] Müller, V. *et al.* Antimony doped tin oxide nanoparticles and their assembly in mesostructured film. *Phys. Status Solidi C* **8**, 1759 (2011).
- [3] Seo, S. *et al.* Reproducible resistance switching in polycrystalline NiO films. *Appl. Phys. Lett.* **85**, 5655 (2004).
- [4] Gorbenko, O. Y., Samoilenkov, S. V., Graboy, I. E. & Kaul, A. R. Epitaxial stabilization of oxides in thin films. *Chem. Matter.* **14**, 4026 (2002).
- [5] Netzer, F. P. “Small and beautiful”-the novel structures and phases of nano-oxides. *Surf. Sci.* **604**, 485 (2010).
- [6] Henrich, V. E. & Cox, P. A. *The Surface Science of Metal Oxides*, vol. 1 (Cambridge University Press, 1994).
- [7] Schuler, T. M. *et al.* Character of the insulating state in NiO: a mixture of charge-transfer and Mott-Hubbard character. *Phys. Rev. B* **71**, 115113 (2005).
- [8] Kuneš, J., Anisimov, V. I., Skornyakov, S. L., Lukoyanov, A. V. & Vollhardt, D. NiO: correlated band structure of a charge-transfer insulator. *Phys. Rev. Lett.* **99**, 156404 (2007).
- [9] Alberts, L. & Lee, E. W. Magnetostriction in antiferromagnetic nickel oxide. *Proc. Phys. Soc.* **78**, 728 (1961).
- [10] Hüfner, S., Steiner, P., Sander, I., Reinert, F. & Schmitt, H. The electronic structure of NiO investigated by photoemission spectroscopy. *Solid State Commun.* **80**, 869 (1991).
- [11] Mott, N. F. The basis of the electron theory of metals, with special reference to the transition metals. *Proc. Phys. Soc. A* **62**, 416 (1949).
- [12] Zaanen, J., Sawatzky, G. A. & Allen, J. W. Band gaps and electronic structure of transition-metal compounds. *Phys. Rev. Lett.* **55**, 418 (1985).
- [13] Savrasov, S. Y. & Kotliar, G. Linear response calculations of lattice dynamics in strongly correlated systems. *Phys. Rev. Lett.* **90**, 056401 (2003).
- [14] Nestbitt, H. W., Legrand, D. & Bancroft, G. M. Interpretation of Ni2p XPS spectra of Ni conductors and Ni insulators. *Phys. Chem. Minerals* **27**, 357 (2000).
- [15] Richardson, D. & Hisscott, L. A. Many-electron structure in the XPS spectra of some transition metals and alloys. *J. Phys. F: Metal Phys.* **6**, L127 (1976).

- [16] van Veenendaal, M. A. & Sawatzky, G. A. Nonlocal screening effects in  $2p$  X-ray photoemission spectroscopy core-level line shapes of transition metal compounds. *Phys. Rev. Lett.* **70**, 2459 (1993).
- [17] Biju, V. & Khadar, M. A. Electronic structure of nanostructured nickel oxide using Ni  $2p$  XPS analysis. *J. Nanopart. Res.* **4**, 247 (1993).
- [18] Preda, I. *et al.* Interface effects in the Ni  $2p$  x-ray photoelectron spectra of NiO thin films grown on oxide substrate. *Phys. Rev. B* **77**, 075411 (2008).
- [19] Alders, D., Voogt, F. C., Hibma, T. & Sawatzky, G. A. Nonlocal screening effects in  $2p$  x-ray photoemission spectroscopy of NiO (100). *Phys. Rev. B* **54**, 7716 (1996).
- [20] Soriano, L., Preda, I., Gutiérrez, A. & Palacín, S. Surface effects in the Ni  $2p$  x-ray photoemission spectra of NiO. *Phys. Rev. B* **75**, 233417 (2007).
- [21] Sangaletti, L., Depero, L. E. & Parmigiani, F. On the non-local screening mechanisms in the  $2p$  photoelectron spectra of NiO and  $\text{La}_2\text{NiO}_4$ . *Solid State Commun.* **7**, 421 (1997).
- [22] Taguchi, M. *et al.* Revisiting the valence-band and core-level photoemission spectra of NiO. *Phys. Rev. Lett.* **100**, 206401 (2008).
- [23] Bala, J., Oleś, A. M. & Zaanen, J. Zhang-Rice localization, quasiparticle dispersions, and the photoemission of NiO. *Phys. Rev. Lett.* **72**, 2600 (1994).
- [24] Günther, C., Vrijmoeth, J., Hwang, R. Q. & Behm, R. J. Strain relaxation in hexagonally close-packed metal-metal interfaces. *Phys. Rev. Lett.* **74**, 754 (1995).
- [25] Schmid, A. K., Bartelt, N. C., Hamilton, J. C., Carter, C. B. & Hwang, R. Q. Brownian motion of dislocations in thin films. *Phys. Rev. Lett.* **78**, 3507 (1997).
- [26] Zajonz, H., Baddorf, A. P., Gibbs, D. & Zehner, D. M. Structure of pseudomorphic and reconstructed thin Cu films on Ru(0001). *Phys. Rev. B* **62**, 10436 (2000).
- [27] Günther, S., Kopatzki, E., Bartelt, M. C., Evans, J. W. & Behm, R. J. Anisotropy in nucleation and growth of two-dimensional islands during homoepitaxy on “hex” reconstructed Au(100). *Phys. Rev. Lett.* **73**, 553 (1994).
- [28] Manai, G., Radican, K., Delogu, F. & Shvets, I. V. Room-temperature self-assembly of equilateral triangular clusters via Friedel oscillations. *Phys. Rev. Lett.* **101**, 165701 (2008).
- [29] Brune, H., Bromann, K., Roder, H. & Kern, K. Effect of strain on surface diffusion and nucleation. *Phys. Rev. B* **52**, R14380 (1995).

- 
- [30] Hildebrandt, S. *et al.* Real time scanning tunneling microscopy study of the initial stages of oxidation of Ni(111) between 400 and 470 K. *J. Vac. Sci. Technol. A* **18**, 1010 (2000).
- [31] Barbier, A. *et al.* Atomic structure of the polar NiO(111)- $p(2\times 2)$  surface. *Phys. Rev. Lett.* **84**, 2897 (2000).
- [32] Greber, T., Wider, J., Wetli, E. & Osterwalder, J. X-ray photoelectron diffraction in the backscattering geometry: a key to adsorption sites and bond lengths at surfaces. *Phys. Rev. Lett.* **81**, 1654 (1998).
- [33] Vu Grimsby, D. T., Wu, Y. K. & Mitchell, K. A. R. A LEED analysis for the Ni(111)- $(2\times 2)$ -O surface structure: evidence for oxygen-induced relaxations of both vertical and lateral types in the close packed surface layer of nickel. *Surf. Sci.* **232**, 51 (1990).
- [34] Davila, M. *et al.* A scanned-energy mode photoelectron diffraction study of the structure of Ni(111) $(2\times 2)$ -O. *Surf. Sci.* **232**, 51 (1990).
- [35] Viana, M. L., Díez Muiño, R., Soares, E. A., Van Hove, M. A. & de Carvalho, V. E. Global search in photoelectron diffraction structure determination using genetic algorithms. *J. Phys.: Condens. Matter* **19**, 446002 (2007).
- [36] Viana, M. *et al.* Scaling behavior of genetic algorithms applied to surface structural determination by LEED. *Surf. Sci.* **602**, 3395 (2008).
- [37] Martínez-Blanco, J., Joco, V., Quiròs, C., Segovia, P. & Michel, E. G. Surface x-ray diffraction analysis using a genetic algorithm: the case of Sn/Cu(100)- $(3\sqrt{2}\times\sqrt{2})r45^\circ$ . *J. Phys.: Condens. Matter* **21**, 134011 (2009).
- [38] Siegler, M. A., Parkin, S., Selegue, J. P. & Brock, C. P. The elusive  $[\text{Ni}(\text{H}_2\text{O}_2)_{15}\text{-crown-5}]^{2+}$  cation and related co-crystals of nickel(II) hydrates and 15-crown-5. *Acta Cryst.* **B64**, 725 (2008).
- [39] Chang, C.-L. *et al.* Compositional tuning of ultrathin surface oxides on metal and alloy substrates using photons: dynamic simulations and experiments. *Phys. Rev. B* **81**, 085406 (2010).
- [40] Caputi, L. S., Jiang, S. L., Amoddeo, A. & Tucci, R. Coxygen-nickel bond length in Ni(111)- $p(2\times 2)$ O determined by electron-energy-loss fine-structure spectroscopy. *Phys. Rev. B* **41**, 8513 (1990).

## Chapter 5

# Mn<sub>3</sub>O<sub>4</sub> oxide film on stepped Pd(1 1 17)

### 5.1 Introduction

As already mentioned in the previous chapter, manganese oxide belongs to a class of TM oxides characterized by an extraordinarily complex electronic structure owing to *d*-electron correlations and charge transfer effects. The bulk MnO and NiO phases, indeed, exhibit many similar properties. For instance, both the oxides have been widely studied for their insulating character, which is generally explained in terms of the Mott-Hubbard and the charge transfer theoretical models. In fact, the same interpretation of the final state effects discussed in the previous chapter in the case of NiO, is often proposed also to describe the satellite structures observed in the Mn $2p_{3/2}$  core level spectrum of the MnO [1]. After the creation of a core hole in a metal atom, the charge transfer from a ligand atom to the unoccupied *d*-orbital of the metal lowers the total energy of the system, thus changing the relative BEs of the final states. In particular, the distribution of the final state energies is determined by the balance between the charge transfer energy and the intra-atomic Coulomb repulsions. MnO shows a charge transfer energy comparable to the repulsion energies, thus it represents a borderline case between Mott-Hubbard- and CT-type insulators [2]. On the other hand, NiO is found to have a smaller CT energy than MnO, thus showing a prevalent CT character. This is one of the arguments used to explain the weaker covalent character of the Mn $3d$ -O $2p$  bond in MnO compared to NiO [3].

When the dimensionality is reduced, greater differences between these two TM oxides are expected. One of the most intriguing properties that distinguishes MnO from NiO thin films is certainly the magnetic ordering of the oxide layer. In chapter 4 I reported on the preference of the NiO thin film to expose the antiferromagnetic (AFM) (100)-oriented surface, rather than the ferromagnetic (FM) NiO(111) facet. The (100) surface of 3D MnO also shows an AFM character, but in the 2D limit, a Mn<sub>3</sub>O<sub>4</sub> ultra-thin film supported on

Pd(100) is observed to display a FM spin alignment [4]. This clearly indicates the presence of complex magnetic correlations between the spin states of MnO, in addition to the many-body interactions involving its electronic states. Furthermore, investigations of the ultra-thin Mn oxides grown on Pd(100) pointed out a tight interplay among the lattice strain, the magnetic ordering and the Mn3d–O2p hybridization [4]. Since the lattice constant of MnO(100) is  $\sim 14\%$  larger than that of Pd(100), a significant lattice mismatch between the Mn<sub>3</sub>O<sub>4</sub> layer and Pd(100) is expected. It follows that a (100)-oriented MnO layer cannot entirely release the stress built up in the lattice-matching process. This is the reason why Mn<sub>3</sub>O<sub>4</sub> is found to show a peculiar surface reconstruction driven by Mn-vacancies. In addition, the oxide films are observed to form ordered islands of limited size surrounded by rough edges, thus indicating a relaxation of the residual strain at the boundaries. On the basis of theoretical calculations and experimental evidences, it has been suggested that the on site FM spin alignment is a consequence of this strain-induced reconstruction [5].

The present experiment focuses on the growth of the same kind of Mn oxide film, but this time on a vicinal surface of Pd(100), namely the Pd(1 1 17) facet. Ideally, this surface displays a series of regular (100)-oriented terraces separated by monoatomic steps, hence it is also called stepped Pd(100) surface. However, the surfaces of actual samples are characterized by a wide distribution of the terrace widths and by irregular step edges. Surprisingly, a previous STM analysis of the oxide film-covered Pd(1 1 17) surface revealed a large-scale uniformity of step morphology and highly regular terrace widths. After the growth of a Mn<sub>3</sub>O<sub>4</sub> film, the surface presented much more regular step edges and larger terraces, thus reshaping the Pd(1 1 17) surface into a (1 1 21) periodically stepped surface with terraces of almost the same width [6]. In fig. 5.1 are reported the STM images of the clean Pd surface (a) and of the same surface after the oxide growth (b). The authors suggested that the lattice strain and the lateral confinement occurring during the lattice matching process could play an important role in the determination of the final surface structure. However, no detailed structural models were proposed to describe the local geometries of the oxide film. Our combined STM, DFT and XPD investigation of this Mn oxide surface was aimed at understanding the local geometry of Mn<sub>3</sub>O<sub>4</sub> on the (100)-oriented Pd terraces in relation to the analogous oxide phase found on the flat Pd(100) surface. Due to the presence of step edges, the oxide film is expected to experience a larger lattice stress when grown on vicinal surfaces. Therefore, we were interested in understanding if the structure of the oxide films formed on the terraces of Pd(1 1 17) (i.e. vicinal of Pd(100)) and on Pd(100) were comparable.

The present work was carried out in collaboration with S. Surnev<sup>1</sup>, F. P. Netzer<sup>1</sup>, F. Allegretti<sup>2</sup> and C. Franchini<sup>3,4</sup>, who have additionally supported us with the STM study and the DFT theoretical calculations. My contribution to

<sup>1</sup>Institut für Experimentalphysik, Karl-Franzens-Universität, Graz, Austria.

<sup>2</sup>Technische Universität München, München, Deutschland.

<sup>3</sup>Fakultät für Physik, Universität Wien, Wien, Austria.

<sup>4</sup>Center for Computational Materials Science, Wien, Austria

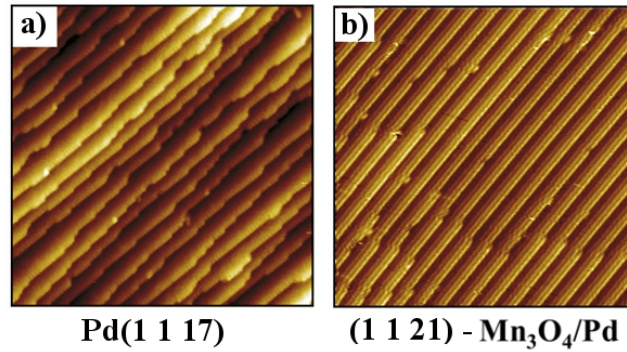


**Figure 5.1:** a) STM image of the clean Pd(1 1 17) stepped surface showing a wide distribution of terrace widths. b) STM image of the Pd surface after the oxide film growth. The effects of both terrace faceting and step edge sharpening are visible [6].

this work is mainly related to the analysis of the XPD data and the subsequent structural determination.

## 5.2 Experimental and computational details

Our angle scanned XPD data were collected at the SuperESCA beamline using the snapshot mode, which allows a fast data acquisition of the photoemission spectra. The Pd sample surface was cleaned by repeated cycles of sputtering and annealing up to 873 K, followed by additional annealing cycles up to 773 K in  $\text{O}_2$  background. After a final annealing up to a temperature close to 1000 K, the sample showed sharp LEED spots corresponding to the clean Pd(1 1 17) surface. The subsequent sample preparation was similar to that followed for Ni oxides, and consisted of 0.75 ML Mn atom deposition (using an Omicron EFM3 Evaporator) at a sample temperature below 300 K, followed by post-oxidation at 670 K, at an  $\text{O}_2$  pressure of  $5 \times 10^{-8}$  mbar. The photoemission signal from the  $\text{O}1s$  core level was observed to overlap with an extra peak, which probably was a satellite structure of the Mn oxide. This would make the subsequent spectral deconvolution more difficult. Therefore, we preferred to collect the XPD modulation functions from the  $\text{O}2s$  core level, which showed a single spectral component and led the same structural information as those from the  $\text{O}1s$  core level. The diffraction patterns were collected at three excitation energies: 140, 170 and 240 eV. For each pattern the polar angles span over  $77^\circ$  and the measured azimuthal angles range from  $0^\circ$  to  $170^\circ$ . Given the low photon energy used and the limited lateral extension of the surface oxide owing to the small terrace width, the MSCD simulation code was employed to perform the multiple scattering calculations. In fact, if the atomic clusters are small enough, the MSCD package has the advantage of providing more accurate MS calculations at very low kinetic energies with respect to the EDAC code. The atomic clusters used for these calculations consisted on the average of 100 atoms,

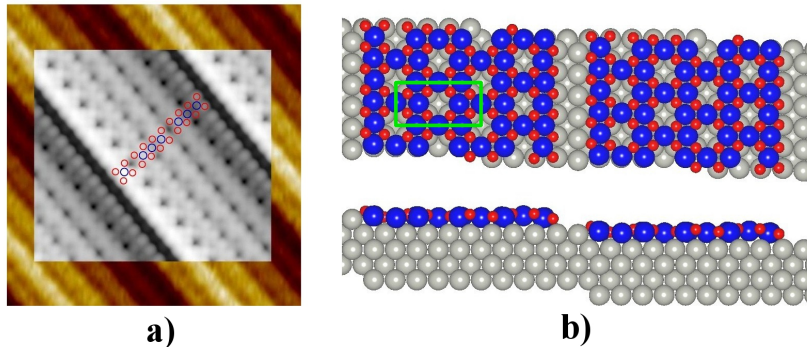


**Figure 5.2:** a) Experimental and simulated STM images of the oxide-covered Pd(1 1 17) surface. b) The theoretical model calculated by DFT, in which the green rectangle indicates the unit cell of the superlattice.

including the first two Pd layers and the oxide layer. The deeper Pd layers were neglected because, given the relatively low IMFP of the photoelectrons, only the Pd atoms of the first two layers could significantly scatter the photoemission signal from the oxide film.

### 5.3 DFT structural model

Density functional theory calculations performed by our co-workers shed light on the possible structure of the ultra-thin Mn oxide film. The structural model predicted by DFT is shown in fig. 5.2b, where the Pd substrate is represented by the light gray spheres, while the blue and red ones indicate the Mn and O species, respectively. In this model, the Mn oxide layers are distributed only on the terraces and locally present the same structure of the Mn<sub>3</sub>O<sub>4</sub> layer on Pd(100) described in Ref. [4]. In fact, DFT results suggested that this 2D oxide film should be a (100)-oriented MnO film but decorated by Mn vacancies, which yield the superlattice its characteristic  $c(4 \times 2)$  symmetry (marked by the green rectangle in fig. 5.2b). Moreover, strain-induced lateral relaxation and out-of-plane buckling effects were also observed. Due the large lateral stress accumulated at the step edges, the borders of the oxide films are strongly restructured. This is clearly visible for the two MnO rows beneath the step edges in the side view of the structure of fig. 5.2b. In fig. 5.2a, a comparison between the experimental and the simulated STM images is shown. A good agreement between the acquired STM image and the simulated result can be noticed. In the simulated image the positions of both the Mn and O atoms are marked, and the dark spots correspond to the Mn vacancies.

STM is a powerful technique for determining the surface morphology and buckling effects with a high spatial resolution. However, it has a quite limited sensitivity to the interface geometry between the oxide and the substrate. In fact, the STM measurements could confirm the relaxed Mn<sub>3</sub>O<sub>4</sub> structure and the rhombic distribution of the vacancies, but they could not unequivocally

establish whether the surface is characterized by Mn or O vacancies, nor identify the adsorption sites of the oxide layer. Therefore, some further investigation of the interface morphology was needed. Our XPD analysis helped us get a deeper insight into the structure of the interface region.

## 5.4 Structural determination of the thin oxide film by means of XPD

Besides checking the correctness of the DFT model, our XPD analysis had the target of determining the local interface relaxation of the oxide film relative to the Pd substrate. In this respect, different structural aspects were addressed, including the nature of the vacancies (either Mn or O), the adsorption configuration of the overlayer on the substrate and, of course, the actual extent of the local relaxation around the vacancies.

As already mentioned at the beginning, a large strain effect is expected at step edges, which could considerably modify the local structure of the thin film. The presence of rough borders poses a problem for XPD measurements, because it can reduce the coherence of the interference patterns generated by the photoelectrons. Moreover, the MSCD code requires a periodic atomic cluster for MS calculations, but a simulation cluster limited only to one terrace could not satisfy this periodicity requirement. For these reasons, we decided to use an atomic cluster made of a Mn<sub>3</sub>O<sub>4</sub> layer on a flat Pd(100) substrate. In this way, although we neglected step edge effects, we were still very sensitive to the interface relaxations occurring on the terraces.

Taking the structure of Mn<sub>3</sub>O<sub>4</sub>/Pd(100) as a reference, we initially assumed that the oxide film presented Mn vacancies. Starting from a perfectly square in-plane symmetry, the (x, y, z) coordinates of all the inequivalent O and Mn atoms were independently optimized. The structure yielding the lowest R-factor is reported in fig. 5.3a (top view) and 5.3b (side view). Interestingly, the stressed Mn<sub>3</sub>O<sub>4</sub> layer supported on a terrace showed the same in-plane relaxation as that found by the DFT calculations. The green rectangle in fig. 5.3a indicates the c(4×2) coincidence cell, where the blue and red spheres represent Mn and O atoms, respectively. The Mn atoms can be of two types, labelled Mn1 and Mn2, respectively. The former indicate the Mn atoms belonging to the horizontal Mn rows with missing atoms, the latter instead are the Mn atoms found in the rows without Mn vacancies. The vacancy-induced structural relaxation can be understood by separately considering the displacement of the O and Mn atoms. In a Mn<sub>3</sub>O<sub>4</sub> oxide film, each O atom is bound to 3 nearest neighbor Mn atoms instead of 4. As a consequence, the individual Mn–O bonds are stronger. In particular, all the O atoms are shifted towards the Mn2 rows which have a higher Mn density. The arrow on the left side of fig. 5.3a indicates the drift of the O atoms from the Mn1 rows along the vertical axis, labelled as  $\delta y_{\text{O}}$ . The value of this vertical displacement is  $0.17 \pm 0.10$  Å. Such a strong surface modification is driven by the increased Mn–O bonding strength, which,

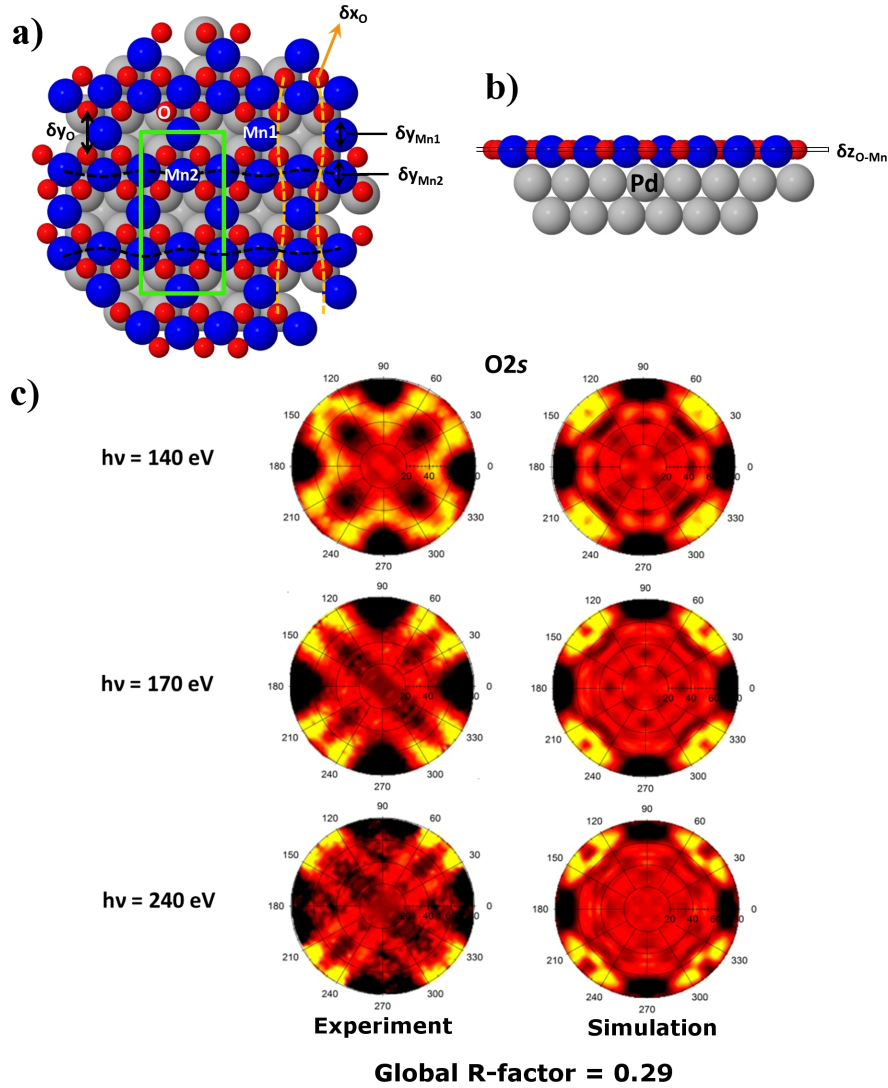


**Figure 5.3:** Top (a) and side (b) view of the structural model proposed by our XPD analysis. The  $c(4 \times 2)$  cell is colored with green and the different relaxation modes of both the Mn and O atoms are illustrated by the dashed lines. c) A comparison between the measured and the simulated XPD patterns of the  $O2s$  core level at three photon energies, the total R-factor is 0.29.

at the same time, is responsible for the large-scale zig-zag modulation of the O atoms around the vertical axis (marked by the dashed orange line and labelled as  $\delta x_O$ ). The maximum amplitude of this periodic modulation is estimated to be  $0.19 \pm 0.10$  Å. The structural complexity of this Mn oxide film is further increased by the zig-zag displacements of the Mn2 atoms along the horizontal direction, as highlighted by the dashed black curve. This is a consequence of the lateral compression caused by the O atoms which get closer to the Mn2 atomic rows. In fact, one can easily notice that the Mn2 atoms move always towards

the Mn vacancies, where the O density is lower. This model is additionally supported by the identical value obtained for the O displacements,  $\delta y_{\text{O}}$ , and for the amplitude of the Mn2 zig-zag modulation  $\delta y_{\text{Mn2}}$ . The Mn1 atoms, on the other hand, basically don't display any lateral displacement.

During our XPD analysis of the Mn<sub>3</sub>O<sub>4</sub> film local structure, particular attention was devoted to understanding if the Mn1 atoms show any lateral displacement along y direction. Because previous DFT calculations had pointed out a direct relationship between the lateral positions of the Mn1 atoms and the magnetic ordering of the whole oxide film. In fact, *ab initio* studies on Mn<sub>3</sub>O<sub>4</sub>/Pd(100) proved that a ferromagnetic spin state would favor the configuration with all the Mn1 atoms located at identical four-fold hollow sites relative to the Pd(100) substrate; whereas an antiferromagnetic ordering would induce a 0.07 Å lateral displacement of Mn1 atoms along y axis [4]. Our XPD based structural relaxation showed that all the Mn1 atoms are centered at the hollow sites, in particular,  $\delta y_{\text{Mn1}} = 0.00 \pm 0.05$  Å is smaller than 0.07 Å. Therefore, this experimental evidence further confirmed the FM ordering of the Mn oxide film predicted by the DFT calculations.

Another important result achieved by our XPD analysis was the evaluation of the large vertical separation between the Mn and O atoms, indicated as  $\delta z_{\text{O-Mn}}$  in fig. 5.3b. Previous DFT and STM studies estimated a Mn–O distance along the surface normal as large as 0.2 Å, which is very close to the experimental value obtained for the Mn<sub>3</sub>O<sub>4</sub>/Pd(100) system (0.23 Å [4]). This considerable metal-oxygen out-of-plane displacement seems to be a specific characteristic of the ultra-thin manganese oxide. In fact, very similar oxide phases have been detected on Pd(100) upon oxidation of sub-monolayer Co and Ni layers, which give rise to the same c(4×2) superlattices showing the same metal vacancies. However, structural investigations of both the Ni<sub>3</sub>O<sub>4</sub> and the Co<sub>3</sub>O<sub>4</sub> films found a negligible difference between the vertical position of the oxygen and of the metal atoms [7–9]. Our XPD results, on the other hand, yielding a Mn–O vertical distance of  $0.13 \pm 0.05$  Å, unequivocally confirmed the large upward shift of the O atoms with respect to the Mn lattice.

In fig. 5.3c are reported the experimental XPD patterns collected at different photon energies, and the best fitting simulated patterns are correspondingly shown in the right column. The minimum R-factor we obtained is 0.29. Most of the intense modulation features located at large polar angles in the experimental patterns are correctly reproduced by our simulations. Among all the possible structures, we proved that the configuration shown in fig. 5.3a corresponds to the global minimum of our R-factor hyperspace. In fact, no further improvement of the R-factor was attained by varying one structural parameter at time. A considerable problem of the experimental patterns is related to the lack of a perfect fourfold symmetry, as it could be expected for a quasi-square lattice. In fact, two rotational domains of the c(4×2) phase are found on the Pd(100) surface, rotated by 90° with respect to each other. For some reason, presumably due to the different extent of the lattice strain induced at step edges by the two domains, the majority of the Mn<sub>3</sub>O<sub>4</sub> films grown on the Pd(1 1 17) ter-

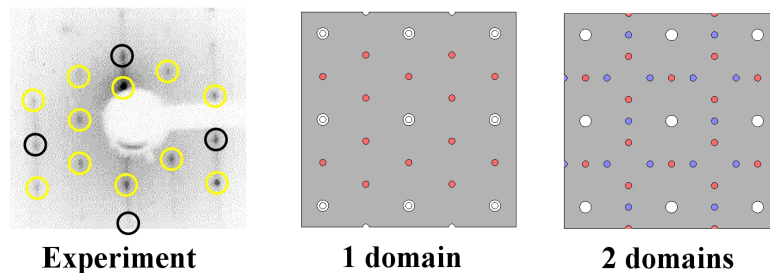


**Figure 5.4:** Comparison between the experimental LEED pattern and the simulated patterns obtained by including one and two domains of the  $c(4 \times 2)$  phase.

faces expose the same domain. This is confirmed by a comparison of the LEED patterns shown in fig. 5.4. The diffraction spots ascribed to the oxide film are marked by yellow circles in the experimental pattern. Two simulated LEED patterns are reported on the right, which were calculated by including one and two domains, respectively (the domains are differently colored). Only the spots belonging to one domain (red) can be found in the experimental pattern, while the other pattern, originated by the rotated domain (blue), is missing. Therefore, the existence of only one orientation for the oxide film can reasonably explain the twofold symmetry of our XPD patterns. It is worth noticing that these two domains are actually very similar. The geometrical differences arise exclusively from the local relaxations which partly break the fourfold symmetry.

In our best fitting structural model, the O atoms were placed on top of the Pd substrate, according to the theoretical predictions. Anyway, we also tested other two possible configurations. In the first one, the Mn atoms were all placed on top of the Pd atoms, which yielded an R-factor of  $0.32 \pm 0.01$ . In the second structure, instead, both the O and Mn species were found in bridges sites, which resulted in an R-factor of  $0.30 \pm 0.01$ . Although these two R-factors differ from the lowest one ( $0.29 \pm 0.01$ ) just by a small amount, we could still conclude that the configuration with the Mn atoms on top was not the correct one, while we were not sensitive enough to safely rule out the bridge geometry.

The last check we made was considering the configuration with O vacancies in lieu of Mn vacancies. Since the vacancies arise as a consequence of lattice strain, and the stress to which the oxide film is subjected may be different on a flat or a stepped Pd substrate, the formation of O vacancies is still possible. Moreover, given the O atoms are the emitters in our XPD patterns, any variation in their number or position would dramatically modify the results of the MS simulations. In fact, as shown in fig. 5.5, the theoretical 2D modulation functions change completely in passing from a  $\text{Mn}_3\text{O}_4$  to a  $\text{Mn}_4\text{O}_3$  thin film. It becomes immediately evident that, in the structure characterized by O vacancies, the most intense diffraction features are located in out-of-phase angular positions relative to the experimental ones. This clearly ruled out the  $\text{Mn}_4\text{O}_3$  configuration. In fact, it gave an R-factor of 1.35, which means that the sim-

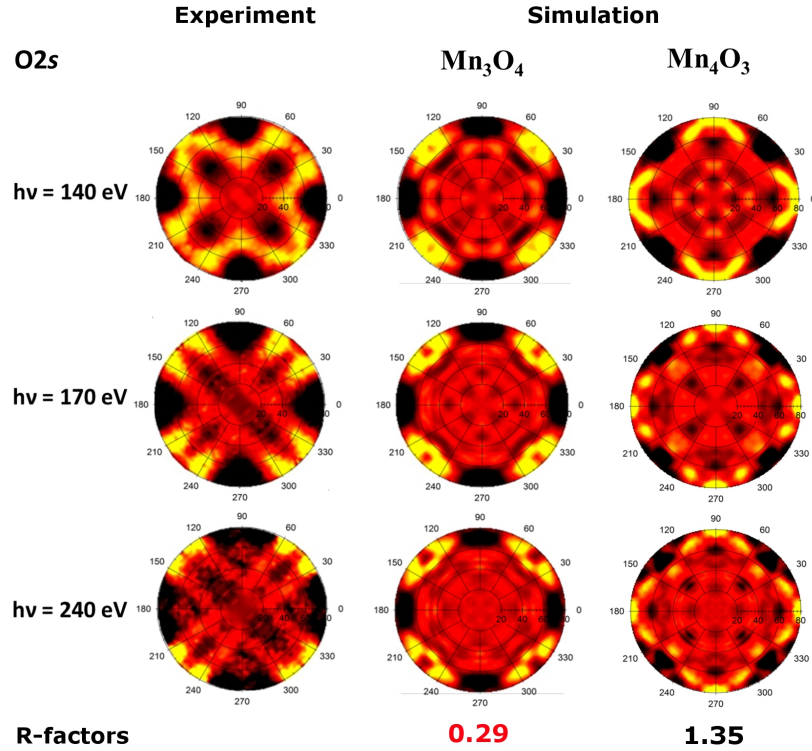


**Figure 5.5:** A check of the actual atomic species forming the vacancies in the  $c(4 \times 2)$  lattice. In the left column are reported the experimental  $\text{O}2s$  XPD patterns, while in the two columns on the right are shown the simulations for the  $\text{Mn}_3\text{O}_4$  and the  $\text{Mn}_4\text{O}_3$  structures. The corresponding R-factors are also indicated.

ulated patterns are either uncorrelated (1) or anti-phase correlated (2) to the experimental ones. At this point, we can allege that the  $\text{Mn}_3\text{O}_4$  model yields in all respects the correct structure.

## 5.5 Conclusions

In this chapter we have investigated the structure of an epitaxial  $\text{Mn}_3\text{O}_4$  film grown on the terraces of a vicinal surface of Pd(100), namely the Pd(1 1 17) surface. The formation of this ultra-thin Mn oxide leads to the observed  $c(4 \times 2)$  phase on both the flat and the stepped Pd surfaces, and our combined XPD, STM and DFT investigation clearly demonstrated that the same relaxed structure is found in both cases.

The most important aspect of this low dimensional oxide is the close relationship between the lattice strain effects and its structural, electronic and magnetic properties. On Pd(1 1 17), the formation of the  $\text{Mn}_3\text{O}_4$  layer is observed to induce ordering and faceting effects of the step terraces, which display a (1 1 21) periodicity. A significant contribution to this uniform reshaping of the

terraces comes from the step edge strain. Owing to the large difference between the lattice parameters of the oxide film and the substrate, Mn vacancies form in order to allow a commensurate lattice matching. The lattice strain is then released by structural relaxations both perpendicular and parallel to the oxide plane. Our XPD analysis provided a structural model which definitely validated the DFT and STM results. In addition, the absence of a lateral displacement of the Mn1 atoms further confirmed the ferromagnetic spin alignment of the  $\text{Mn}_3\text{O}_4$  film, already predicted by the DFT calculations.

## References

- [1] Bagus, P. S. & Ilton, E. S. Effects of covalency on the *p*-shell photoemission of transition metals: MnO. *Phys. Rev. B* **73**, 155110 (2006).
- [2] van Elp, J., Potze, R. H., Eskes, H., Berger, R. & Sawatzky, G. A. Electronic structure of MnO. *Phys. Rev. B* **44**, 1530 (1991).
- [3] Fujimori, A. *et al.* Electronic structure of MnO. *Phys. Rev. B* **42**, 7580 (1990).
- [4] Franchini, C. *et al.* Interplay between magnetic, electronic, and vibrational effects in monolayer Mn<sub>3</sub>O<sub>4</sub> grown on Pd(100). *J. Chem. Phys.* **130**, 124707 (2009).
- [5] Franchini, C. *et al.* Structural and vibrational properties of two-dimensional Mn<sub>x</sub>O<sub>y</sub> layers on Pd(100): Experiments and density functional theory calculation. *Phys. Rev. B* **79**, 035420 (2009).
- [6] Li, F., Allegretti, F., Surnev, S. & Netzer, F. P. Atomic engineering of oxide nanostructure superlattices. *Surf. Sci.* **604**, L43 (2010).
- [7] Allegretti, F. *et al.* Strained c(4×2) CoO(100)-like monolayer on Pd(100): experiment and theory. *Surf. Sci.* **604**, 528 (2010).
- [8] Agnoli, S. *et al.* Experimental and theoretical study of a surface stabilized monolayer phase of nickel oxide on Pd(100). *J. Phys. Chem. B* **109**, 17197 (2005).
- [9] Ferrari, A. M., Ferrero, M. & Pisani, C. An ab initio periodic study of NiO supported at the Pd(100) surface. Part 2: The nonstoichiometric Ni<sub>3</sub>O<sub>4</sub> phase. *J. Phys. Chem. B* **110**, 7918 (2006).



## Chapter 6

# Surfactant Pb monolayer on Ag(100)

### 6.1 Introduction

Ultra-thin metal films with few atomic layers thickness have been successfully grown on different kinds of substrate for various purposes. In particular, ultra-thin Pb films have attracted considerable attention in the scientific community for their manifold attractive characteristics, both from the point of view of the technological applications [1–3] and of the theoretical description of interesting solid state phenomena [4,5].

Ultra-thin metal films represent an ideal support for atomic adsorption and cluster growth, e.g. in the fabrication of electrical contacts and in the development of new catalysts. For all these applications, a high film quality represents a fundamental requirement. It has been recently found that, covering the (111) surface of an fcc substrate with a uniform Pb layer prior to metal atom deposition will promote their layer-by-layer growth. In this growth mode, a new atomic layer starts to form only once the one beneath is complete, thus inhibiting multiple island nucleation or multilayer growth [6]. This kind of film is also called *surfactant layer*, owing to the fact that Pb is not miscible with the substrate. Surfactant Pb layers have been observed to modify the adatom diffusion mechanism, by enhancing inter-layer diffusion on the terraces, and reducing the intra-layer hopping. Metallic films with the best structural quality have been indeed obtained when the substrate is fully covered with a lead monolayer [7].

From the electronic structure point of view, recent studies on Pb films have seemingly proved evidence of superconducting properties even at few monolayers coverage. In fact, it has been shown that at a Pb film thickness smaller than 2 ML superconducting gaps can locally open. These discoveries have been the object of a great interest because they represent the first 2D superconducting material ever have been observed until now [2,3]. Moreover, the authors identified different surface phases formed during low coverage Pb adsorption

on Si(111), each of which is characterized by a different critical temperature and whose growth is confined to a specific surface region. This may pave the way towards film interface engineering aimed at controlling the superconductive transition temperature. Of course, further experimental evidence is required to validate these preliminary results, but they clearly pointed out the key role of ultra-thin films, as well as the importance of interface structures and interactions in determining the magnetic ordering at the critical temperature.

Low coverage Pb deposition on Ag surfaces is another interesting topic in relation to the Rashba-type spin-splitting observed in surface alloys and in Pb monolayer films. The Rashba-Bychkov model [8] is widely applied in the description of a particular class of surface electronic states where, owing to the breaking of the structural inversion symmetry along surface normal, a perpendicular electric field is generated, which acts by lifting the electron spin degeneracy. In fact, spin-splitting and energetically shifted surface bands have been revealed by using Angle Resolved PhotoEmission Spectroscopies (ARPES) from various surfaces [9,10]. However, such a vertical electric field is not the only reason that induces spin-splitting. A thorough knowledge of the structural details of such systems is required in order to correctly understand the mechanism of spin degeneracy removal. Surface corrugation, relaxation and spin-orbit interactions are also important factors to be considered in the interpretation of the splitted band dispersions and of the energy shift [11,12]. In particular, given the comparable atomic size and spin-orbit coupling strength of the deposited heavy metal atoms (Pb, Bi, Sb) and of the Ag substrate, the in-plane lattice potential gradient, which removes the spin degeneracy, must be derived from the structural differences. Indeed, direct relationship can be established between the size of the surface alloy buckling and the momentum offset between the splitted bands (for details see Ref. [11] and references therein). In addition, Dil *et al.* [1] reported a Rashba-type splitting also for the Quantum Well states of Pb films. They further proposed that the Rashba effect depends on the interface structure rather than on the film thickness, and suggested the possibility to investigate the correlation between Rashba splitting and the superconductivity by means of structural analysis of interfaces.

All the previously cited works on Pb deposition on Ag surfaces mainly regard the (111)-oriented Ag surface [11,13]. To our best knowledge, no studies on the surface phases, or on the band dispersion of ultra-thin Pb films on the Ag(100) surface have been reported so far. The goal of the present work is to investigate the surface phases formed on Ag(100) after Pb deposition, and, to provide a thorough interpretation of the interface phenomena by means of a combined geometrical and valence band structural description. We identified a new commensurate phase after nearly 1 ML Pb deposition<sup>1</sup>, and analyzed its atomic structure using XPD, while its bonding properties were investigated using ARPES. In the following sections, I will first provide some experimental

---

<sup>1</sup>Actually, there is a previous work which reports on similar results [14], but that surface had not been prepared under UHV conditions, and only a few structural details are provided.

details, and then report on both XPD and ARPES results. Finally, conclusive discussions will connect structural aspects with the information on the electronic band structure yielded by ARPES.

This experiment is a joint project carried out in collaboration with the Laboratoire de Spectroscopie Electronique (LSE) of the *Institute of Condensed Matter Physics (ICMP)* of *Ecole Polytechnique Fédérale de Lausanne (EPFL)*, in Lausanne, Switzerland. The XPD and ARPES data presented here were collected both at the LSE Laboratory of ICMP and at the VUV photoemission beamline of Elettra. A description of this experimental station has already been given in section 2.2.4.

## 6.2 Experimental details

The Ag(100) single crystal was cleaned by repeated sputtering and annealing cycles. The cleaning treatment consists of 30 minutes  $\text{Ar}^+$  sputtering at 1 keV ion energy at room temperature, followed by 25 minutes annealing to 800 K. This procedure was sufficient to clean and reorder the sample surface. Before Pb deposition, the sample surface quality and cleanness were always tested by checking if a sharp  $(1 \times 1)$  LEED pattern was visible.

Pb was evaporated at 300 K using a homemade Knudsen cell operating at a 0.15 ML/min atomic flux. When the lead inside the crucible is heated up to its sublimation temperature, the out-coming Pb atoms are collimated towards the specimen. In order to ensure a fine control on the amount of Pb atoms evaporated on the sample surface, a movable shield is placed between the evaporator and the sample. After Pb deposition, the sample surface shows a characteristic LEED pattern indicating a  $c(6 \times 2)$  long-range ordered phase, which is highly reproducible at the same coverage. This ordered phase covers homogeneously the entire sample surface. We did not observe any other ordered surface structure at lower or higher Pb coverage. The Pb monolayer is thermally stable at temperatures below 600 K (annealing up to 600 K results in a much broader LEED pattern, due to Pb desorption), and indeed both the XPD and ARPES maps were acquired at room temperature. Once the Pb layer is formed on the Ag surface, it seems to be inert towards the residual gases in the UHV chamber (the background pressure was  $1 \times 10^{-10}$  mbar). Therefore, long measurements could be performed before re-preparing the sample.

## 6.3 Qualitative analysis of the $c(6 \times 2)$ -Pb phase

After 1 ML Pb deposition, the sample shows more than one single lattice symmetry on the surface. As it is clear from the LEED images in fig. 6.1, there are sets of diffraction spots originating from 3 lattices of distinct symmetry and periodicity. The black circles mark the  $(1 \times 1)$  spots of the underlying Ag(100) square lattice. In the image acquired at 128 eV electron energy (panel b), a series of spots arranged in a circle are clearly visible. They do not follow any

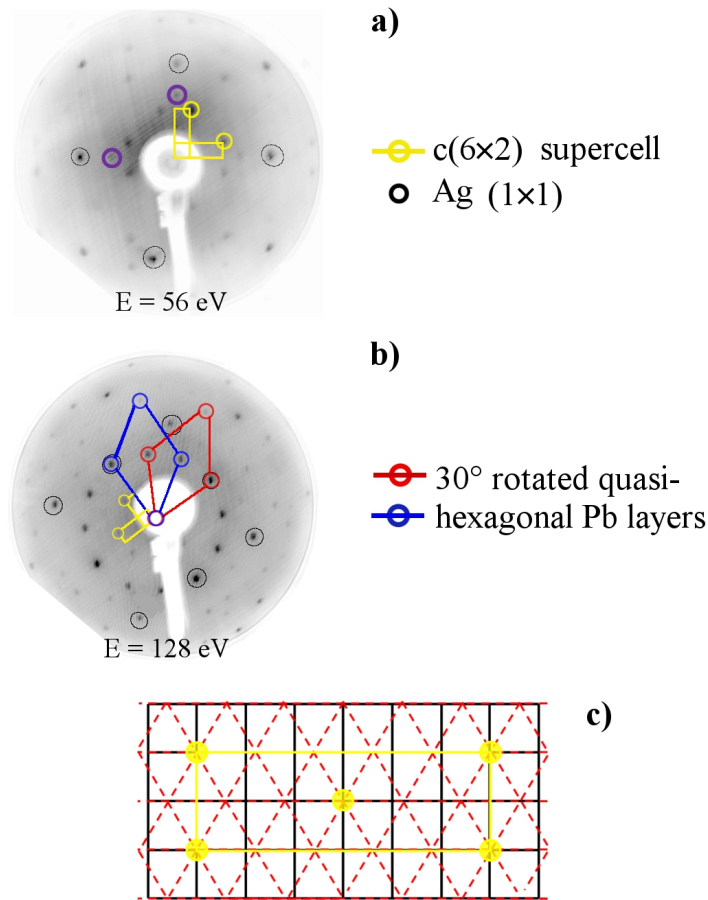


**Figure 6.1:** a) and b): LEED patterns of the surface after 1 ML Pb deposition at two different electron energies. The  $c(6\times 2)$  supercell is highlighted in yellow; the reciprocal lattices of the quasi-hexagonal Pb layers are colored red and blue. The picture in panel c) schematically shows the origin of the coincidence cell (yellow) between one Pb layer (red) and the Ag substrate (black).

periodicity which can be obtained from the primitive vectors of the  $\text{Ag}(100)$  lattice; instead, they belong to the hexagonal Pb overlayers with in-plane  $60^\circ$  rotational symmetry. Moreover, two domains of the Pb layer rotated by  $30^\circ$  are present on the silver surface, and they are highlighted with red and blue colors in fig. 6.1b. Both Pb lattices are commensurate with the substrate. Their matching gives rise to a larger coincidence cell, namely a centered rectangular cell with sides 6 and 2 times longer than the lattice parameter of  $\text{Ag}(100)$ . This cell is hence called  $c(6\times 2)$  unit cell, and is evidenced in the image in fig. 6.1a. This rectangular superlattice is also characterized by two domains owing to the presence of the two rotated Pb layers. Moreover, the extra spots highlighted with purple rings arise from the  $(3\times 1)$  sub-periodicity associated to the  $c(6\times 2)$  cell. The sketch in fig. 6.1c schematically explains how the matching between the Pb layer and the substrate gives rise to the rectangular coincidence cell.

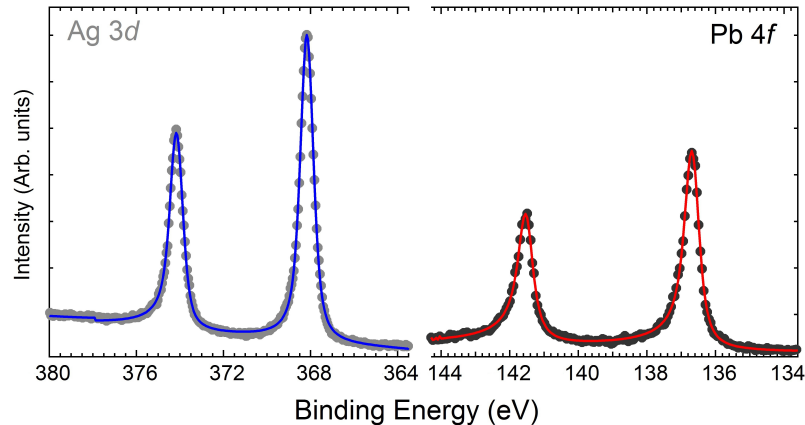


**Figure 6.2:** Photoemission spectra of  $\text{Ag}3d$  (left,  $h\nu = 500$  eV) and  $\text{Pb}4f$  (right,  $h\nu = 280$  eV) core levels, in which both the spin-orbit splitted components are present. The dots correspond to the raw experimental data, while the solid lines are the theoretical Doniach-Šunjić curves.

Rather unexpectedly, the Pb layer exhibits the features of a hexagonal close-packed lattice instead of following the square symmetry of the substrate. In fact, earlier studies on similar systems, namely  $\text{Pb}/\text{Cu}(100)$  [15] and  $\text{Bi}/\text{Ag}(100)$  [16], showed a preference of heavy metal layers to form pseudo-square lattices rather than hexagonal ones.

In figure 6.2, the XPS spectra of the  $\text{Ag}3d$  and  $\text{Pb}4f$  core levels are presented. Apparently, both the core levels can be fitted with a single spin-orbit splitted component, and an acceptable agreement (good enough for the successive XPD analysis) is found between the experimental data and the theoretical spectra. Actually, one may expect to observe different chemically shifted components, especially for the  $\text{Pb}4f$  core level, due to all the possible geometrically inequivalent configurations of the Pb atoms on the substrate. However, our experimental energy resolution was not high enough to allow their deconvolution; therefore, a large singly peaked Doniach-Šunjić function was used for XPD data fitting. During XPD measurements, photoemission spectra were collected only at the energy intervals of the higher intensity spin-orbit sublevels,  $\text{Ag}3d_{5/2}$  and  $\text{Pb}4f_{7/2}$ , respectively.

## 6.4 XPD results

XPD data were acquired for the  $\text{Ag}3d_{5/2}$  and  $\text{Pb}4f_{7/2}$  core levels. Interestingly, for both spectral components the periodicity of the intensity modulation perfectly reflects the in-plane lattice symmetry. The azimuthal scans (peak intensity vs  $\varphi$ ) in fig. 6.3a unequivocally show a  $90^\circ$  periodicity reflecting the square symmetry of the  $\text{Ag}(100)$  surface. In fig. 6.3b, the azimuthal intensity modulation of the Pb state exhibits the  $30^\circ$  periodicity which originates from the two rotational domains of the hexagonal Pb layer. All these scans are dis-

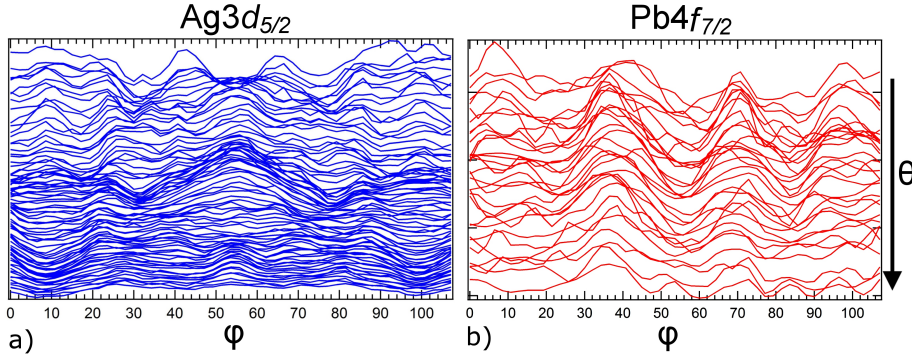


**Figure 6.3:** Intensity modulations of a)  $\text{Ag}3d_{5/2}$  ( $h\nu = 500$  eV), and b)  $\text{Pb}4f_{7/2}$  ( $h\nu = 240$  eV) core levels as a function of the azimuthal angle  $\varphi$  (horizontal axis,  $\Delta\varphi = 110^\circ$ ) at different polar angles  $\vartheta$ , ranging between  $29^\circ$  and  $59^\circ$ , and increase in the direction indicated by the arrow.

played according to their polar angles  $\vartheta$ , which increases in going from the top to the bottom of the graphs. Then it is also evident the signal attenuation by increasing the polar emission angles. However, the modulation functions from  $\text{Pb}4f_{7/2}$  core level were quite noisy, so we decided to exclude the Pb XPD patterns from the evaluation of the R-factor during the structural relaxation, and to retain only the XPD patterns from the Ag core level. This is because modulation noises may strongly affect the calculation of the R-factor, introducing artefacts that do not actually depend on the atomic structure.

XPD patterns of the  $\text{Ag}3d_{5/2}$  core level were collected at four different excitation energies at 450, 500, 550 and 580 eV. These photon energies were chosen in order to maximize the photoionization cross-section, and at the same time to enhance multiple scattering modulations on changing the kinetic energy. Indeed, working at relatively low photoelectron kinetic energies (in the present case between 85 eV and 212 eV), we can focus mainly on the backward scattering features, from which relevant information on the interlayer distances, as well as on the nearest neighbor bond lengths, can be extracted. This is the reason why the back-scattering regime is particularly suitable for XPD investigations of very low-dimensional surface systems such as ultra-thin films.

The experimental polar angles in our experiments was varied between  $0^\circ$  and  $60^\circ$  in steps of  $0.9^\circ$ ; for each polar configuration, the azimuthal angle span over an interval of  $110^\circ$ . In this way, the total experimental angular range is as large as  $33550^\circ$ . The MSCD simulation package was used throughout this work to calculate the theoretical multiple scattering patterns. The diffraction cluster chosen for the simulations are proved to be large enough to include all the most significant modulation features. It consists of three layers of Ag plus the Pb overlayer, and such a cluster would contain 80–100 atoms, depending on the position of the emitter. Considered the actual IMFP of the photoelectrons from the  $\text{Ag}3d_{5/2}$  core level, only the Ag atoms of the first two layers are selected as emitters. The theoretical patterns were obtained by summing the contributions

of all non-equivalent atoms (for both Ag and Pb species), and averaging over the two rotational domains.

Three of the experimental diffraction patterns are illustrated in the first row of fig. 6.4a. Before the actual structural analysis, it is important to carry out some preliminary evaluations. The latter takes into account the experimental data sensitivity to the Pb layer and the correct adsorption sites of the Pb atoms, which also determines the relative position of the  $c(6\times 2)$  cell with respect to the substrate.

In order to test our sensitivity to the presence of Pb, it is sufficient to compare the experimental data with the XPD patterns of the substrate. The simulated diffraction patterns of the clean Ag(100) surface are reported in the second row of fig. 6.4a. Differences between the simulated and the corresponding experimental patterns of the clean Ag substrate are clearly visible at all three photon energies. This first result proved that variations in the Pb atomic positions will produce modifications in the simulated XPD patterns, significant enough to ensure that our structural relaxation procedure is effective. Considering the geometry of the Ag surface, there are three possible positions at which the Pb overlayer atoms can match the substrate atoms, giving rise to the aforementioned superlattice, which can be obtained by translation of the  $c(6\times 2)$  cell along specific lattice directions. For simplicity, they are named hollow, bridge and on-top structures, according to the adsorption site of the Pb atoms at the corner (and at the center for symmetry reasons) of the  $c(6\times 2)$  cell. Obviously, the remaining Pb atoms will be found in some intermediate positions, owing to the different lattice parameters of the Pb layer and the substrate. A schematic representation of these three positions is given in fig. 6.4b, and the corresponding simulated XPD patterns, as well as the calculated R-factors, are reported in fig. 6.4a. Let's now compare these calculated modulation functions with the experimental patterns. First of all, it is easy to notice that none of them yield a good agreement with the experimental data. The simulations shown in the figure have been performed under identical conditions, except for the Pb adsorption site. Although a reasonable choice of both the structural and non-structural parameters has been made, none of them has been optimized yet. The theoretical patterns of the on top position are clearly different from the experimental data, especially at a photon energy of 450 eV, where the two patterns are completely inconsistent each other (R-factor = 1.39). Therefore, this position can be safely ruled out from our further analysis. The best set of simulated patterns corresponds to the hollow configuration (R-factor = 0.54), while for the bridge geometry a much higher R-factor was found (1.00). For example, at  $h\nu = 500$  eV, the highest intensity spots should be located at azimuthal angles which are multiples of  $45^\circ$ ; which is true only in the hollow case. Comparing the patterns at  $h\nu = 450$  eV, one realizes that the positions of the maxima and minima at large polar angles are inverted for both the on top and bridge structures. In the hollow model, instead, these spots are found close to their correct positions. Finally, it is not surprising that Pb atoms prefer to adsorb in the fourfold hollow sites of the Ag(100) surface. In fact, investigations of low coverage phases formed by atomic adsorption on the Ag(100)

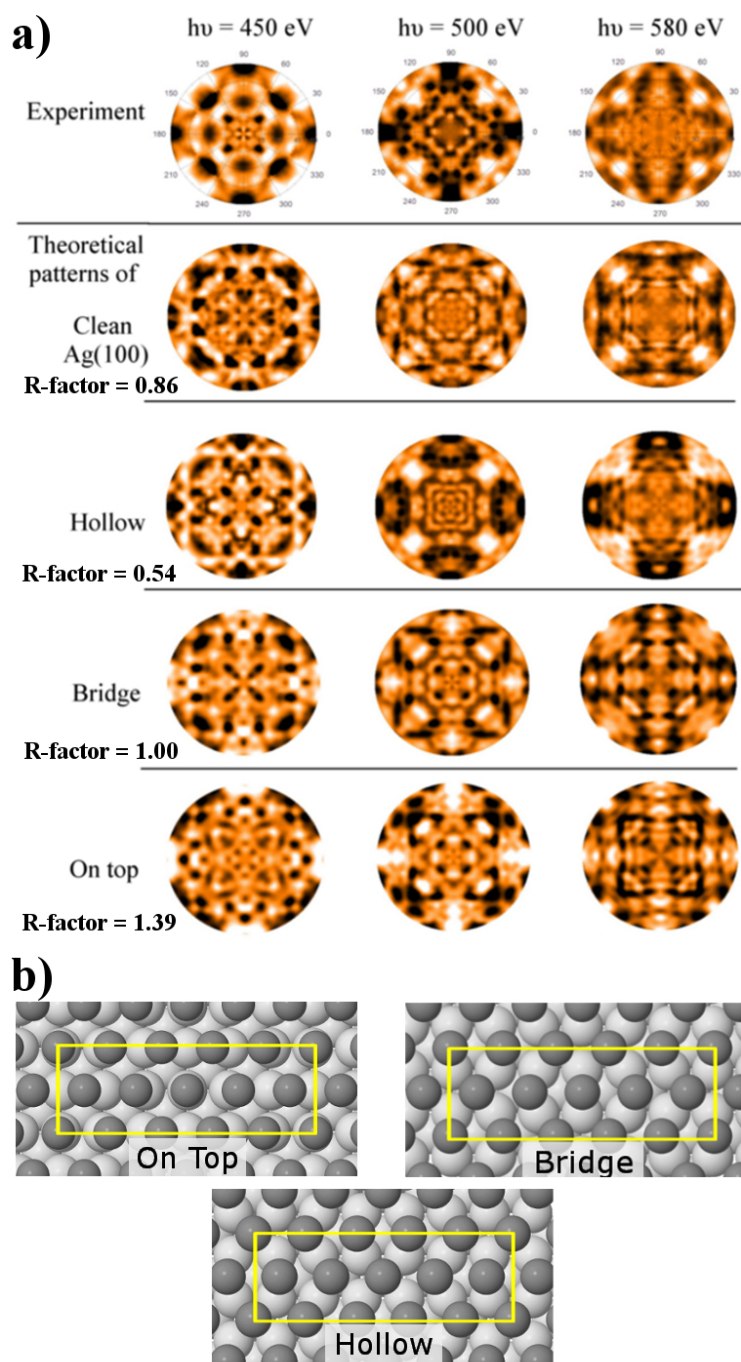


**Figure 6.4:** (a) Diffraction patterns used to compare of all the possible Pb adsorption sites and the corresponding R-factors. See the discussion on the experimental sensitivity to the Pb adlayer in the text. (b) 3-dimensional illustrations of the allowed adsorption sites; only one domain is shown for each of them.

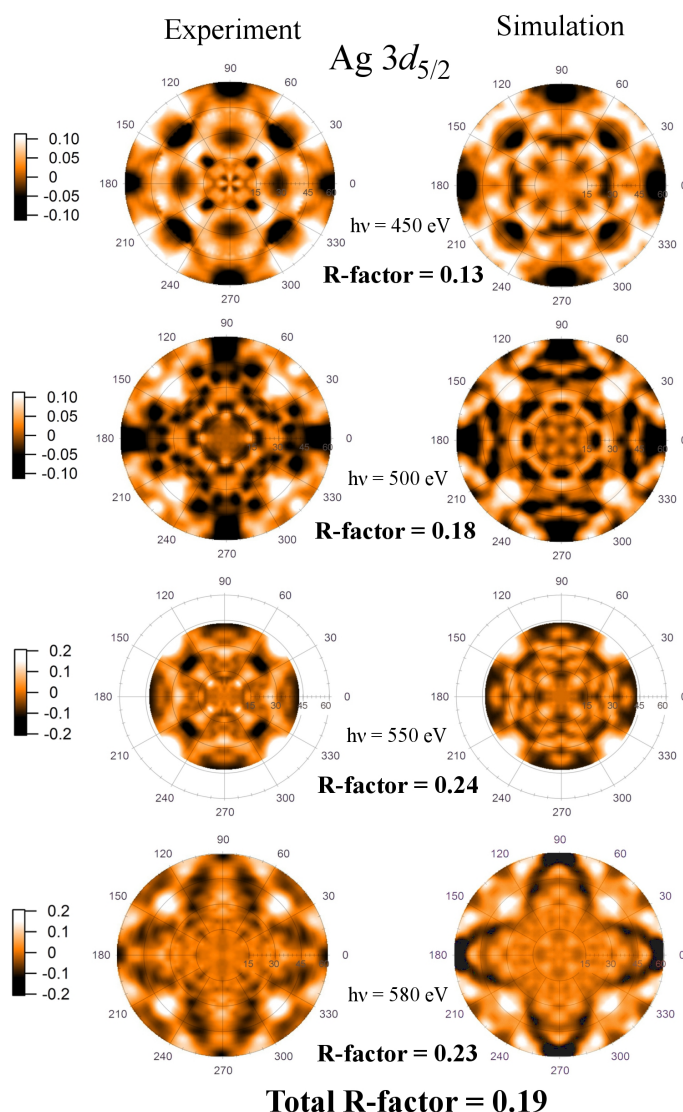


**Figure 6.5:** Experimental (left) and simulated (right) diffraction patterns for the  $Ag3d_{5/2}$  component. The color scales on the left side indicates the  $\chi$ -function amplitude. Photon energies and the partial R-factors are reported in the middle, while the global reliability factor including the whole data set, is given in the bottom. For experimental reasons, the XPD data at photon energy of 550 eV has a smaller angular interval.

surface have generally evidenced the preference for the hollow configuration [16].

In figure 6.5 are reported the stereographic projections of both the experimental and the simulated XPD data. The experimental patterns of the  $Ag3d_{5/2}$  core level are shown in the column on the left and simulations obtained from a best fitting procedure are presented on the right one. The photon energy

increases in going from the top to the bottom of the graph, and the partial R-factor calculated for each photon energy is reported in the middle. The total R-factor, obtained as a weighted average over all photon energies, is given in the bottom of the same figure. In all XPD plots, the amplitude of the modulation function,  $\chi(\vartheta, \varphi)$ , is indicated by a color scale (see legends on the left). The polar angle increases in the radial direction, as reported on the horizontal axis, while the value of the azimuthal angle is indicated on the circular scale around each stereographic projection.

The agreement between theory and experiment can be assessed both qualitatively and quantitatively. In fact, the final R-factor of  $0.19 \pm 0.01$  indicates an excellent agreement between the experimental data and the computational results. Therefore, structural model elaborated from our XPD analysis, shown in figure 6.6, yields a reliable description of the actual surface geometry. This conclusion is additionally supported by the observation that all the experimental primary diffraction spots, together with a large number of higher-order features, are correctly reproduced by the simulations. Also the values of the modulation amplitudes match to a large extent the experimental data.

The experimental patterns describe a fourfold azimuthal symmetry, as expected for the [100]-oriented Ag surface. Indeed, this symmetry reflects the square geometry characteristic of the arrangement of both the emitter atoms (Ag) and a large part of the scatterers. However, a lot of the diffraction features are also originated by the scattering events occurring on Pb atoms. These contributions become particularly significant at low kinetic energy, as in the present case, where the XPD technique is extremely surface sensitive. On the contrary, the patterns acquired at higher electron energy show remarkably Ag bulk-like features, which is less useful to directly probe the Pb film geometry. Consequently, the smaller partial R-factors obtained for the XPD data collected at lower kinetic energy further supports the validity of structural model concerning the interface region of the Pb/Ag(100) system.

However, some small discrepancies between experiment and simulations can be still found. These differences are more pronounced at large polar angles, i.e., on the border of the XPD patterns. For example, in the theoretical patterns some diffraction features are present at  $\varphi \approx (40^\circ \div 50^\circ)$  and at large polar angles, whereas they are missing in the experimental ones. On increasing the electron kinetic energy, this problem becomes even more evident. A possible explanation of these mismatches could be the following. The electron inelastic mean free path increases with increasing kinetic energy; from the computational point of view, a bigger cluster and a larger RA matrix are required to keep a sufficient accuracy. However, very large clusters or RA matrices will demand considerable computational efforts. Therefore, a reasonable compromise between the size of these quantities and the calculation time is sought. Owing to the limited cluster size and the reduced number of RA matrix elements, as well as to cluster boundary effects, simulated XPD features can differ from the experimental patterns especially at grazing emissions angles.

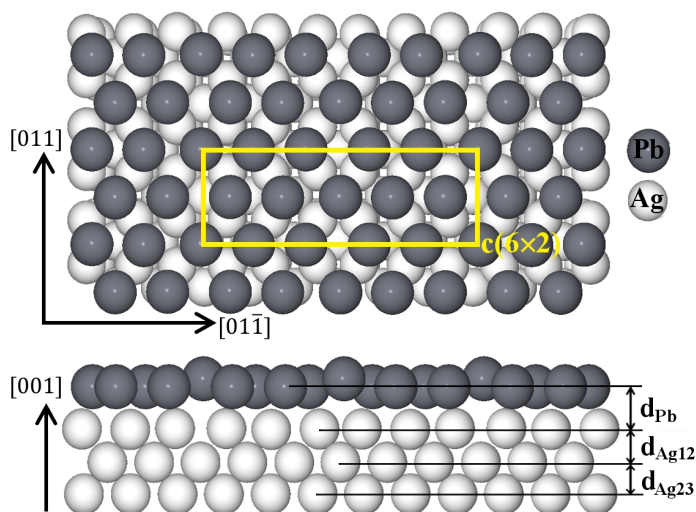


**Figure 6.6:** Top (upper panel) and side (lower panel) view of the structural model for the Pb/Ag(100) surface proposed on the basis of XPD investigations. The interlayer distances discussed in the text are reported on the right side of the bottom picture. The yellow rectangle indicates the  $c(6 \times 2)$  supercell.

The structural model we propose on the basis of our combined LEED and XPD analysis is shown in figure 6.6. The dark gray spheres represent Pb atoms and the bright grey ones indicate the Ag substrate. From this picture, it is evident that the Pb surface thin film forms a pseudo-hexagonal layer, with in-plane primitive vectors of slightly different lengths. This periodicity is independently confirmed both by previous LEED measurements, and by the BZ map as will be described later in fig. 6.1 and fig. 6.7b. The Pb layer is quasi-hexagonal because of the strong lattice matching with the substrate. In fact, the Pb atoms are arranged to form a commensurate and periodic superlattice with the substrate,  $c(6 \times 2)$  superstructure, whose unit cell is indicated by the yellow rectangle in figure 6.6 (following the same convention used in fig. 6.1). Again, only the one of two domain is illustrated; the other one can be obtained by simply rotating the hexagonal Pb layer by  $30^\circ$  (the  $c(6 \times 2)$  cell undergoes a  $90^\circ$  rotation). The rectangular supercell contains 10 Pb atoms and 12 Ag atoms of the first Ag layer; hence the Pb coverage is slightly smaller than 1 ML.

The structural relaxation is carried out according to the following procedure. In the first step, all the atoms in the topmost three Ag layers and in the Pb layer are constrained in a planar arrangement, and the three interlayer distances are allowed to vary all at the same time. As shown in the lower part of figure 6.6, a small interlayer relaxation is found for Ag substrate:  $d_{\text{Ag}12} = 2.04 \pm 0.05 \text{ \AA}$  and  $d_{\text{Ag}23} = 1.90 \pm 0.05 \text{ \AA}$ . The spacing between the first Ag layer and Pb overlayer,  $d_{\text{Pb}}$ , is equal to  $2.55 \pm 0.05 \text{ \AA}$ . This is a reasonable estimate, because it is close to the average between the bulk interlayer distances of the Ag ( $2.04 \text{ \AA}$  [17]) and of the Pb(111) ( $2.86 \text{ \AA}$  [18]) lattices, a similar distance is

found also in the case of ultra-thin Pb films grown on Ag(111) surface [13]. A fine structural relaxation is performed for all the non-equivalent atoms inside the  $c(6\times 2)$  cell of the Pb layer and for the Ag atoms in the first substrate layer, while the interlayer distances are held fixed. The choice to relax only these two layers is due to the fact that they have a stronger influence on the diffraction patterns than the remaining layers because of the electron mean free path reasons. We optimized the  $(x, y, z)$  positions of the 10 Pb and 12 surface layer Ag atoms by the implementation of the steepest-descent algorithm. The final result shows a corrugation of the Pb layer, accompanied by an in-plane displacement for both layers. Along the direction normal to the surface, the most significant effect is the buckling of the Pb atoms placed in the center and at the corners of the  $c(6\times 2)$  unit cell. The atoms in these site are raised by  $0.4 \pm 0.1 \text{ \AA}$  with respect to the average height of the Pb film. This is the consequence of the strong lattice stress arising when two layers of different symmetry match to form a commensurate lattice. In fact, the Pb atoms preferentially adsorb in hollow sites; but, owing to the geometrical mismatch, not all of them are allowed to occupy lattice sites of this type. Actually, some Pb atoms are found in quasi-bridge positions. Interestingly, during the local atomic relaxations, some of the Pb atoms shift from the quasi-bridge to quasi-hollow sites along the  $[011]$  direction, thus getting closer to the Pb atom at the center of the supercell. These in-plane displacement have two main consequences. The first one is the outward buckling of the central Pb atom discussed above, in order to maintain the same Pb-Pb bonding distance. The second one is the expansion of the Ag lattice in the region underneath the buckled Pb atom along the  $[01\bar{1}]$  direction ( $0.08 \pm 0.03 \text{ \AA}$ ). This shift, instead, is probably forced by the Coulomb repulsion from the larger electron cloud surrounding the buckled Pb atom.

## 6.5 Valence band studies by means of ARPES

Besides the structural characterization of the  $c(6\times 2)$ -Pb phase by means of XPD, we also used ARPES to investigate the valence band dispersion at the interface. The combination of these two techniques allows, on one hand, to unravel the mechanisms with which the Pb film grows and bonds to the substrate, and, on the other hand, to study the electronic structure in relation with the binding effect between the film and silver surface.

The main ARPES results are summarized in figure 6.7. Part of these data were collected at the VUV photoemission beamline of Elettra, the others were measured at the LSE at ICMP of EPFL. In fig. 6.7a the main lattice symmetries in  $k$ -space (i.e., in the reciprocal space) are schematically drawn in a two-dimensional plot (the  $x$ - and  $y$ - axis correspond to the cartesian components of the  $\vec{k}_{||}$  vector,  $k_x$  and  $k_y$ ). The same symmetries appear as those obtained from our XPD results. The green square is associated to the Ag(100) substrate, and the high symmetry points,  $M_{Ag}$  and  $X_{Ag}$ , are also indicated. Intuitively enough, the blue and red hexagons represent the Brillouin Zones (BZ) of the two rotational domains of the Pb overlayer. Due to the overlap with the Ag

substrate underneath, each of the 2 hexagonal lattices show 2 types of non-equivalent  $K_{\text{Pb}}$  points. One lies along the  $\Gamma M_{\text{Ag}}$  direction, the other one forms an angle of  $60^\circ$  with the first. The three segments drawn in this figure indicate the directions along which the band dispersion reported in panels c), d) and e) are measured.

Figure 6.7b displays a constant energy map (CEM) acquired at a binding energy of  $-0.6$  eV. The photon energy used was 21.22 eV. This image results from the four-fold symmetrized sum of three data sets, measured along the  $\Gamma-M_{\text{Ag}}$ , the  $\Gamma-X_{\text{Ag}}$  and the  $\Gamma-K_{\text{Pb}}$ . At the center of the map, some dark patterns, whose shape reminds two rotated flowers, are clearly visible. They originate from the  $p_{xy}$  bands of Pb, and are related to the hexagonal symmetry of the rotational domains. As we approach the BZs boundaries, twelve dark rings are visible around the central flower shapes. They are found exactly on the vertices of the red and blue hexagons, which correspond to the  $K_{\text{Pb}}$  points of both the domains. These pocket-like shapes are characteristic of quasi-free standing Pb(111) thin films, that are have already been observed in the case of other surfactant layers [19]. However, the pockets in this case are more rounded than those typical of the surfactant Pb layer, which have a triangular shape. As already mentioned before, not all these  $K_{\text{Pb}}$  points are equivalent. In fact, the spots near the  $M_{\text{Ag}}$  point of the substrate appear doubled. A closer view of a double pocket is reported on the right side of fig. 6.7b. The horizontal line separating the two rings is originated by the Ag  $sp$  state, and, its middle point corresponds to the  $M_{\text{Ag}}$  high symmetry point.

The images in the lower part of fig. 6.7 display the band dispersions of the Pb/Ag interface along the three directions shown in panel a). The horizontal axis of image c) corresponds to the red line in a), while that of image b) corresponds to the blue line, and so on. The plots on the right side of every image schematically show the bands individuated in the experimental image, and the dashed vertical lines mark the high symmetry points. The brightest line in c) is the Ag  $sp$  state and the weaker one is its Umklapp replica at  $M_{\text{Ag}}$  due to the Ag  $(1 \times 1)$  periodicity (both are indicated with the yellow lines in the graph on the right side). A second weak signal shows up as a small curve right below the Fermi level, for  $k_x$  values between  $1.5 \text{ \AA}^{-1}$  and  $1.9 \text{ \AA}^{-1}$ . This signal is labeled as “Ag U” in panel c), is generated by the Umklapp of the Ag  $sp$  state on the  $c(6 \times 2)$  lattice periodicity. Then all the other bands shown in the image belong to Pb  $6p$  states. The band labeled with  $\text{Pb}_1$  has prevalently the character of Pb  $p_z$  state, and is centered in the  $\Gamma$  point.  $\text{Pb}_1$  appears in all the three images (indicated with the green line on the plots on right side) and shows large dispersions both in energy and  $\vec{k}_\parallel$  space. In addition, the intensity and the band shape of  $\text{Pb}_1$  depend strongly on the photon energy. Two sets of bands, the  $\text{Pb}_3$  (red) and  $\text{Pb}_2$  (blue), which describes the dispersion of the Pb  $p_{xy}$  band, are evidenced in c). The former, which has its band minimum at  $K_{\text{Pb}}$ , is doubled due to the presence of its Umklapp replica owing to the substrate symmetry at  $M_{\text{Ag}}$  (which is the symmetric axis between the two branches of the  $\text{Pb}_3$  band). The latter ( $\text{Pb}_2$ ), instead, are shown as a blue double parabola and exhibit a dispersion which is symmetric with respect to the  $M_{\text{Ag}}$  point. The splitting of

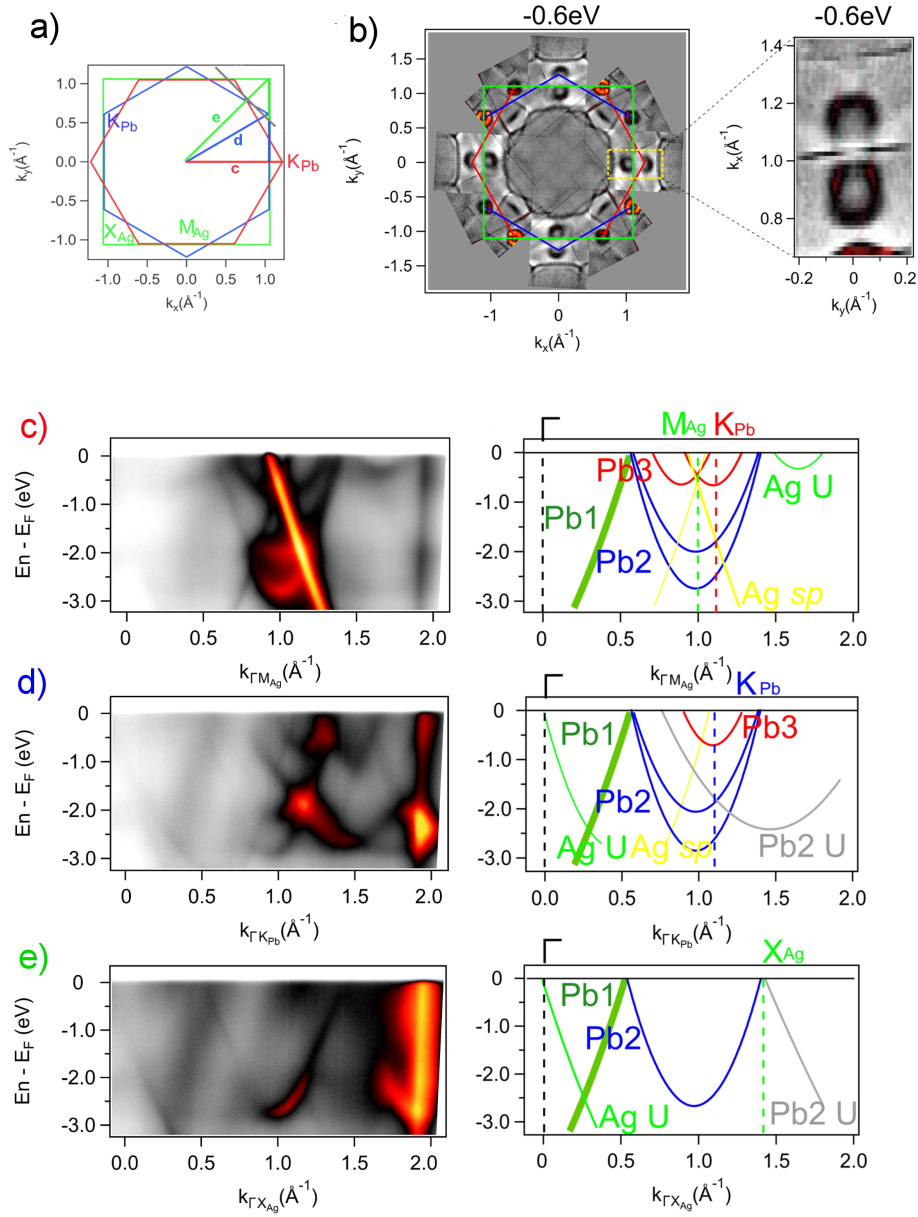


**Figure 6.7:** a) A sketch of the Brillouin zone of the Pb/Ag(100) interface projected on  $\vec{k}_{\parallel}$  plane, and the high symmetry directions along which band dispersions in c), d) and e) are measured, are traced and labeled accordingly. The panels on the right schematically represents the bands shown in the map on the left. b) A constant energy map at  $-0.6$  eV binding energy. The colored contour lines are the same as in panel a) the image on the right is a close-up of the region of the double pockets around the  $M_{Ag}$  points.

$Pb_2$  is originated by the presence of the two rotated hexagonal domains. Dispersion of the two branches of the  $Pb_2$  band also give rise to the hexagonal flower

shapes in the CEM discussed before in panel b). In the image labeled d), all the above-mentioned features are still present. However, while  $\text{Pb}_2$  is unchanged,  $\text{Pb}_3$  becomes a single parabola because of the lack of the symmetry planes resulting in band folding as observed in c). This is the reason why not all the twelve pockets in fig. 6.7b are equal: only when the BZ of Ag(100) straddles the  $\text{Pb}_2$  band, the latter appears doubled at the  $M_{\text{Ag}}$  point because of the Umklapp process. Moreover, two new Umklapp bands can be found in d). One from the Ag  $sp$  band folding owing to the  $c(6 \times 2)$  symmetry (also named “Ag U”); the other one is generated by the folding of the  $\text{Pb}_2$  band on the substrate periodicity ( $\text{Pb}_2$  U). The latter is very intense and intersects with both the curves of  $\text{Pb}_3$  reaching a minimum at a  $k_x$  value close to  $1.5 \text{ \AA}^{-1}$ . Compared to the previous images, the dispersion along  $\Gamma$ - $X_{\text{Ag}}$  in panel e) shows much simpler bands. In fact,  $\text{Pb}_3$  is absent and  $\text{Pb}_2$  displays a single parabola. This behavior is accounted for by the fact that this symmetry direction is equidistant from the two rotational domains, whose band dispersions thus overlap in  $k$ -space.

In summary, a thorough analysis of both the CEM and the band dispersion along selected BZ cuts further validated the previous LEED and XPD results for the symmetry of Pb-Ag interface and the periodicity of the supported ultra-thin Pb film. The constant energy map unambiguously shows the presence of two Pb lattice domains with six-fold symmetry, rather than with the four-fold symmetry of the substrate. Moreover, also the twelve non-equivalent pockets and the rotated flower-like shapes all point out the same symmetry of the overlayer. The parabolic profile of the Pb  $p_{xy}$  and Pb  $p_z$  bands are observed. The absence of band hybridization between  $p_{xy}$  and  $p_z$  Pb states suggests that Pb-Ag interaction is not strong and the Pb layer behaves like a quasi free-standing overlayer.

## 6.6 Conclusions

In the present work ultra-thin Pb films have been thoroughly characterized by means of LEED, XPD and ARPES. The combination of these three complementary techniques has allowed to obtain information of different properties of the system under study. A deep understanding of the atomic arrangement at the interface, as well as an accurate characterization of the bonding electron states have been achieved.

At 1 ML Pb coverage, a  $c(6 \times 2)$  ordered phase is observed on the Ag(100) surface. Its symmetry and periodicity have first been tackled by LEED, from which the sixfold symmetry of the Pb layer could be derived and the extra spots could be assigned to the larger  $c(6 \times 2)$  coincidence cell. The quasi-hexagonal symmetry of the 2D Pb monolayer has been independently confirmed later by the XPD patterns and by the constant energy ARPES maps. In fact, the presence of two rotated domains associated to the Pb  $p_{xy}$  states leads to the appearance of the double flower shapes and of the twelve pockets on the border of the PB BZ, in the CEM of fig. 6.7b.

In the structural analysis of the XPD patterns, the relaxation of the atomic positions close to the interface region have led to the elaboration of a theoretical model, in excellent agreement with the experimental data, yielding a final R-factor as low as 0.19. The proposed structure is modeled in fig. 6.6. The most relevant effect is the 0.4 Å buckling of the Pb atoms in the hollow sites. This is a consequence of the in-plane displacements of the other Pb atoms from a less favorable bridge site to a quasi-hollow site. These lateral shift reduce the in-plane distances among the Pb atoms surrounding the one in the hollow site, which is consequently shifted upwards with respect to the plane. On the other hand, the locally higher density of Pb atoms in this area causes, though to smaller extent, an expansion of the underlying Ag layer; most likely due to the ensuing electron-electron repulsion. It is important to underline that an out-of-plane buckling of the atoms is frequently observed during the formation of two dimensional films, in particular when the overlayer is strained to stay in registry. Moreover, the Pb atoms in the film seems to interact much more strongly with each other rather than with the substrate. In fact, the core level photoemission spectra in fig. 6.2 do not show large chemical shifts due to Pb–Ag interactions. Consistently with these observations, both the parabolic dispersion of the Pb  $p_{xy}$  state and the pocket-shaped features in the Fermi surface map, observed by ARPES, further suggest the quasi free-standing (or surfactant) nature of the Pb ultra-thin film [19].

## References

- [1] Dil, J. H. *et al.* Rashba-type spin-orbit splitting of quantum well states in ultrathin Pb films. *Phys. Rev. Lett.* **101**, 266802 (2008).
- [2] Zhang, T. *et al.* Superconductivity in one-atomic-layer metal films grown on Si(111). *Nat. Phys.* **6**, 104 (2010).
- [3] Qin, S., Kim, J., Niu, Q. & Shih, C.-K. Superconductivity at the two-dimensional limit. *Science* **324**, 1314 (2009).
- [4] Han, Y. & Liu, D. J. Quantum size effects in metal nanofilms: comparison of an electron-gas model and density functional theory calculations. *Phys. Rev. B* **80**, 155404 (2009).
- [5] Woodruff, D. P. *The chemical physics of solid surface – Surface Alloy and Alloy surface*, vol. 10 (ELSEVIER, 2002).
- [6] Vrijmoeth, J., van der Vegt, H. A., Meyer, J. A., Vlieg, E. & Behm, R. J. Surfactant-induced layer-by-layer growth of Ag on Ag(111): origins and side effect. *Phys. Rev. Lett.* **72**, 3843 (1994).
- [7] Camarero, J. *et al.* Atomistic mechanism of surfactant-assisted epitaxial growth. *Phys. Rev. Lett.* **81**, 850 (1998).
- [8] Bychkov, Y. A. & Rashba, É. I. Properties of a 2D electron gas with lifted spectral degeneracy. *JETP Lett.* **39**, 78 (1984).
- [9] Nicolay, G., Reinert, F. & Hüfner, S. Spin-orbit splitting of the *L*-gap surface state on Au(111) and Ag(111). *Phys. Rev. B* **65**, 033407 (2001).
- [10] Guan, D. *et al.* Strongly enhanced electron-phonon coupling in the Rashba-split state of the Bi/Ag(111) surface alloy. *Phys. Rev. B* **83**, 155451 (2011).
- [11] Gierz, I. *et al.* Structural influence on the Rashba-type spin splitting in surface alloys. *Phys. Rev. B* **81**, 245430 (2010).
- [12] Ast, C. R. *et al.* Giant spin splitting through surface alloying. *Phys. Rev. Lett.* **98**, 186807 (2007).
- [13] Ast, C. R. *et al.* Orbital selective overlayer-substrate hybridization in a Pb monolayer on Ag(111). *Phys. Rev. B* **73**, 245428 (2006).
- [14] Schmidt, U., Vinzelberg, S. & Staikov, G. Pb UPD on Ag(100) and Au(100)–2D phase formation studied by in situ STM. *Surf. Sci.* **348**, 261 (1996).
- [15] Hoesler, W. & Moritz, W. LEED studies of lead on copper (100). *Surf. Sci.* **117**, 196 (1982).
- [16] Nakagawa, T. *et al.* Transition between tetramer and monomer phases driven by vacancy configuration entropy on Bi/Ag(001). *Phys. Rev. B* **75**, 155409 (2007).

- [17] Li, H., Quinn, J., Li, Y. S., Tian, D. & Jona, F. Multilayer relaxation of clean Ag(001). *Phys. Rev. B* **43**, 7305 (1991).
- [18] Huang, G. Q. Surface lattice vibration and electron-phonon interaction in Pb(111) ultrathin superconducting films from first principles: both with and without Si substrate. *New J. Phys.* **13**, 093023 (2011).
- [19] Baumberger, F., Tamai, A., Muntwiler, M., Greber, T. & Osterwalder, J. The electronic structure of a surfactant layer: Pb/Cu(111). *Surf. Sci.* **532**, 82 (2003).

## Chapter 7

# K adsorption on epitaxial graphene

### 7.1 Introduction

During my PhD, I also took part in the study of potassium adsorption on supported graphene. My role in this project consisted in the analysis of the XPD data, in order to experimentally determine the adsorption geometry of the K atoms on epitaxial graphene grown on Ir(111). A comparison has been made between the experimental XPD results and the theoretical predictions based on the DFT calculations performed by Prof. D. Alfé<sup>1</sup>. An excellent agreement has been found between XPD data and theoretical simulations.

There are many reasons which make the investigation of atomic adsorption of Alkali Metals (AM) on supported graphene a very interesting topic. The first is that K-doped graphene represents a simplified model to reproduce the interaction of K with graphite, which is still a controversial issue at present [1]. The second one is related to the possibility to gain some insight on the effects of K adsorption both on the bonding between graphene and the Ir substrate, and on the electron-phonon interaction of doped graphene in the framework of many-body interactions [2,3]. Lastly, owing to the ionic character of the bond between AM atoms and graphene, charge transfer from the adsorbate to the carbon support is expected; the ensuing charge redistribution around the Fermi level may be exploited as a tool to control the conductivity of graphene [4]. Certainly, the investigation of all these phenomena, requires an accurate structural determination.

AMs are highly reactive chemical species characterized by a fairly simple hydrogen-like electronic configuration. When deposited on a metal support, these atoms can act as potential donors towards the substrate, thus easily changing the concentration of free carriers in the latter. For these reasons, the intercalation of AM atoms in a graphite substrate caught considerable attentions

---

<sup>1</sup>University College London, London, UK.

among the researches. In particular, it is well known that the K-covered graphite (0001) surface undergoes different phase transitions, depending on the K coverage, and each surface phase seems to be associated to a particular electronic state [5]. However, after more than 20 years of studies, the extent of the charge transfer from K to graphite is still debated [1]. Despite the relatively simple structural and electronic properties of graphite (strong in-plane bonds between C atoms and, on the other hand, weak interlayer forces between graphite layers in the stacking direction), the nature of the K-C interaction still needs to be unraveled. From this point of view, K-doped graphene represents a model system which offers a direct insight into the K-C bonding nature.

In free standing graphene the free charge carriers behave like Dirac fermions, which lead to an electron mobility much larger than the one found in normal metals. However, the band structure of the free standing graphene shows the well-known Dirac cones with a purely metallic character. Therefore, in order to induce semiconducting properties in the graphene sheet which is far more useful in sight of possible technological applications, a band structure modification is required, in such a way to create a tunable band gap. Indeed, doping graphene with AMs seems to offer a viable method to manipulate the electronic structure around the Dirac point [6,7].

Graphene grown on Ir(111) is a widely characterized system [8–10]. It is also well known that the carbon network interacts very weakly with this transition metal substrate. Therefore, the carbon layer in these conditions can be considered as quasi-free-standing [11], and lend itself as an excellent support for studying the interaction between the AM atoms and the single layer graphene. In this chapter, I will describe the structural aspects of the ordered ( $2\times 2$ ) phase formed by K adsorption on single-layer graphene grown on a Ir(111) substrate.

## 7.2 Experimental setup

As already mentioned before, the graphene layer was grown on a (111)-oriented Iridium single crystal, which is cleaned by  $\text{Ar}^+$  sputtering, followed by annealing cycles to 1370 K. In order to remove residual C contaminants, a series of chemical treatments in a  $\text{O}_2$  background ( $p = 1 \times 10^{-7}$  mbar,  $T = 600\text{--}1100$  K) is performed. The procedure used to grow the graphene on Ir(111) by Chemical Vapor Deposition (CVD) is diffusely reported in literature [12], and, is essentially based on the pyrolytic decomposition of ethylene over the heated sample surface, which leads to C-H bond breaking. The C atoms released in this way can subsequently arrange themselves into the honeycomb network characteristic of graphene. Potassium was evaporated from a well-outgassed sources (SAES getters). Once the purity of the K beam produced by the evaporator has been checked, K atoms were deposited at a sample temperature of 313 K, until the distinctive ( $2\times 2$ ) LEED pattern was observed.

The XPD data were collected at the SuperESCA beamline by using the 5 degrees of freedom manipulator. Different photon energies were sampled to induce photoemission from the C1s core level. The experimental data set is

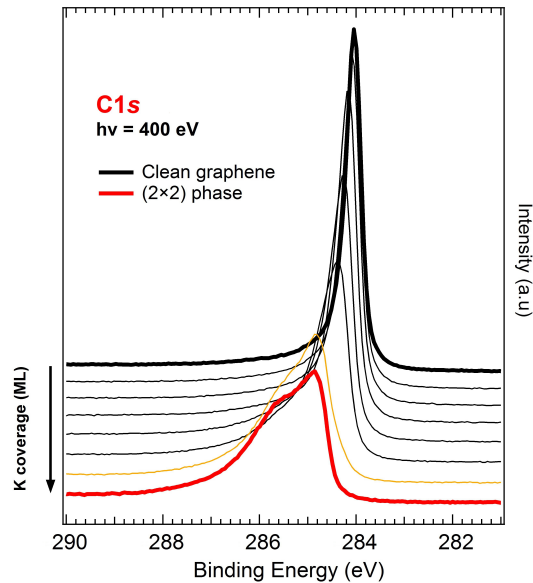


**Figure 7.1:** Evolution of the C1s core level spectrum with increasing K dosa.

composed of four XPD scans acquired at 360, 400, 500 and 600 eV. For each of these photon energies, the spectra were collected at emission angles within a single azimuthal period, and subsequently replicated. Since this surface presents a threefold azimuthal symmetry, measurements were performed on “slices” of the solid angle corresponding to  $\Delta\vartheta = 80^\circ$  and  $\Delta\varphi = 120^\circ$  (the polar and azimuthal angular intervals, respectively), thus the whole data set spans over 16320 different angular configurations.

### 7.3 Preliminary considerations

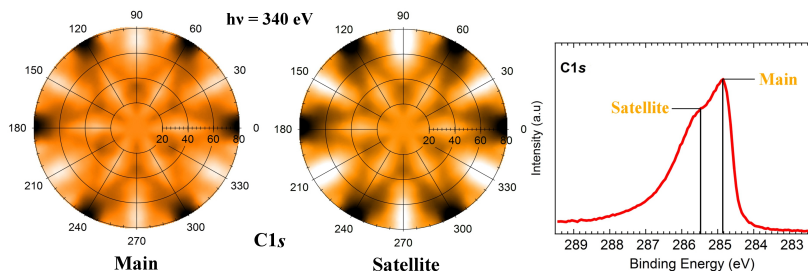
Prior to the actual XPD investigations, a preliminary analysis of the photoemission spectra aimed at identifying the chemical species on the surface is of fundamental importance. This procedure helps to individuate a suitable XPS core level component BE and lineshape which will be used to extract structural information from the analysis of its modulation functions.

Fig. 7.1 reports the evolution of the C1s core level spectrum with increasing K exposure, monitored at  $h\nu = 400$  eV. As indicated by the arrow on the left side of the graph, the K coverage increases in going from the black spectrum on the top (clean graphene) to the red one on the bottom, which corresponds to the completion of the (2×2)-K/graphene phase. The surface phase transitions observed at increasing K exposure are clearly accompanied by a shift of the spectrum towards higher BE, and by the appearance of a shoulder with a higher BE with respect to the main peak. The origin of these spectral changes has to be found in the K–C and K–K interactions. Concerning the main peak (which initially lies at a BE of 284.2 eV), its BE shift is mainly due to the bond-

ing with the adsorbed K atoms; while the intensity decrease can be ascribed to the shielding/scattering effects from the same K overlayer. The same spectrum is observed for the  $(2\times 2)$ -K phase formed on graphite, and the BE shift can be described by using the rigid band model [13]. Owing to the charge transfer from K adatoms to graphene, empty states of the valence band are filled, which shift rigidly upwards thus increasing the FL of the whole system. As a consequence, the measured C1s core level is located at higher BE compared to that of the spectrum of undoped graphene. In addition, the gradual spectral broadening with increasing K dosage is visible in fig. 7.1, and different processes contribute to this effect. First of all, the CT increases the DOS around the FL, which enlarges the phase space for the electron-hole pair creation thus enhancing the spectral asymmetry. A second reason for the Gaussian broadening of the C1s component can be found in the distribution of many non-equivalent C atoms located in different lattice sites which have slightly shifted BEs. Finally, the increased spectral width can be ascribed to the long-range dipole fields built up due to the ionic bonding between K adatoms and graphene [14]. The electrostatic interactions between the K layer and graphene are able to reduce the core-hole lifetime thus increasing the Lorentzian width of the C1s core level spectrum. On the other hand, the origin of the shoulder at higher BE is far less intuitive than that of the main component. At a first sight, this double-peaked structure may be assigned to geometrically non-equivalent C atoms coordinated with different number of K atoms. However, as will be proved later, this is not our case. An analogous behavior was observed in the C1s spectrum of graphite during the K adsorption, where a similar  $(2\times 2)$ -K phase was also detected. However, any attempt to find out a direct relationship between the intensity ratio of the two components and the size of the corresponding non-equivalent populations of C atoms, did not give any satisfactory result [13].

Similarly, in the K-graphene system we investigated, the XPD modulations of the two peaks demonstrate that the extra shoulder in the C1s core level spectrum doesn't originate from differently coordinated C atoms. Indeed, if geometrical differences actually existed between these two species, we would expect to observe different XPD patterns for the two photoemission components. This hypothesis can be clearly ruled out by comparing the XPD patterns of the main peak (left), and of the high BE shoulder (right), displayed in fig. 7.2. Besides slight differences in the modulation amplitudes, all the diffraction features are found in the same position with the same shape in both patterns. For these reasons, we concluded that there are no structural differences between the C atoms which give rise to the main peak and the ones associated to the high BE shoulder. Therefore, the extra feature must be interpreted as a satellite of the main C1s component, generated by photoelectrons which have lost energy in final state interactions.

In the last years, scientists have made large efforts to identify the nature (either ionic or metallic) of the similar K-graphite bonding system, so that the origin of the observed satellite structure has become clearer. Actually, the satellite structure observed in the C1s XPS spectrum can arise from the excitation of photoelectrons travelling through the metallic K overlayer. In fact, at low



**Figure 7.2:** Comparison between the 2D modulation functions of the main (left) and satellite (center) components as derived from the deconvolution of C1s core level spectrum ( $h\nu = 340$  eV). On the right side is reported the corresponding photo-emission spectrum acquired over a BE range that includes both two peaks.

K coverage, a large charge transfer occurs from the K overlayer to the C substrate, so that the adatoms show a prevalently ionic character with a localized charge distribution. When the quasi-monolayer K film is formed, showing the characteristic  $(2 \times 2)$  LEED pattern, the K–K interaction prevails on the K–C interaction. As a consequence, the charge transfer from K to graphene is reduced and the metallic 4s bands of the K overlayer are observed close to the FL, this is called the depolarization effect [1,5,13,15]. Nevertheless, the actual extent of this observed charge transfer in the  $(2 \times 2)$  phase is still under debate, since some discrepancies remain in the results reported in different works [1].

## 7.4 Structural determination by means of XPD

Once we had made sure that the modulation of the C1s core level component at higher BE does not add any structural information to that of the main component, our analysis focused selectively on the XPD patterns of the latter.

Multiple scattering calculations were performed by using the MSCD simulation package, and parabolic atomic clusters including 150 atoms on average, are chosen in all the following simulations. The first thing we evaluated was the convergence of the calculations in terms of the RA-matrix dimensions, the maximum diffraction order and the pathcut. Then we determined the optimum values for the non-structural parameters, i.e. the inner potential (2 V), the Debye temperature (1000 K) and the height of the extension of the electron cloud into the vacuum level (2.0 Å). These parameters were subsequently held fixed to the best values so obtained during the subsequent R-factor minimization procedure adopted for structural relaxation.

The starting point for our structural investigation of the K adsorption geometry was provided by the preliminary DFT calculations performed by D. Alfé. Very accurate simulations were carried out, from which the structure of both the K-graphene and the graphene-Ir(111) interfaces could be derived. In particular, the calculated interlayer distance between the graphene sheet and the Ir(111) substrate is equal to  $4.21 \pm 0.13$  Å, while the K-graphene interlayer distance

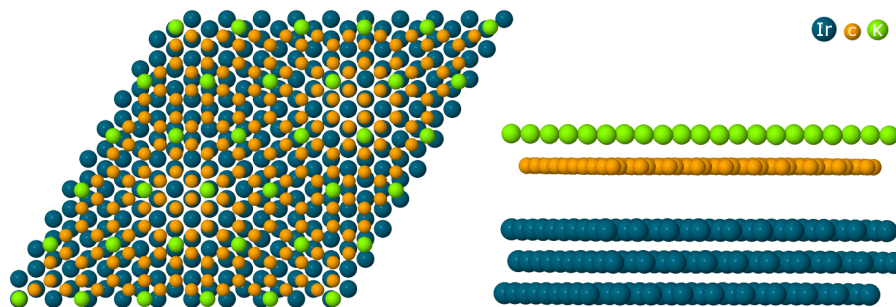


**Figure 7.3:** Structural model of the  $(2\times 2)$ -K/graphene/Ir(111) phase as obtained from the DFT calculations; the top view is shown on the left, the side view on the right.

is  $2.88 \pm 0.50$  Å. In addition, the DFT results unequivocally proved that the lowest-energy adsorption site for K atoms is the sixfold hollow site, where each adatom sits at the center of the hexagon formed by the six C atoms below. A model of the structure obtained from the DFT is shown in fig. 7.3. As explained in the inset on the top right corner, the blue spheres correspond to the Ir atoms of the substrate, the golden ones represent the C atoms of the quasi-free standing graphene layer, and the green spheres represent the K adatoms. The latter adsorb in the hollow sites of the graphene layer, thus giving rise to the observed  $(2\times 2)$  surface periodicity.

Owing to the relatively large distance of the graphene layer from the substrate, the contribution to the overall C1s core level photoemission signal due to electrons back-scattered from the Ir substrate is essentially negligible. In fact, the simulations performed either including or neglecting the metal substrate do not show appreciable differences. Therefore, the presence of Ir substrate was ignored in all the subsequent XPD simulations.

The main issue we are going to tackle by means of XPD is the determination of the distance between the K overlayer and the supported graphene sheet. Because their mutual distance is directly related to their interaction strength, and affects the behavior of the valence band close to Fermi level. In addition, an affirmative XPD result would further validate the theoretical DFT predictions.

The variation of the calculated R-factor as a function of the K-graphene interlayer distance (labeled with  $d_{K-GR}$ ) is shown as red dots in fig. 7.4. These values of the R-factor were then fitted to a polynomial function of the distance; the fit curve is reported in the same graph as a blue solid line. The minimum position of the fit curve yields the most reliable estimate of the K-graphene distance. Owing to the scattering of the points in the R-factor curve, a wide interval of  $d_{K-GR}$  values, ranging from 1.3 Å to 3.6 Å is chosen in order to perform a more accurate curve fitting. The best estimate we finally obtained for  $d_{K-GR}$  is  $2.90 \pm 0.25$  Å, which yields an R-factor of 0.11. Notice that, this rather large K-graphene interlayer distance is in excellent agreement even with

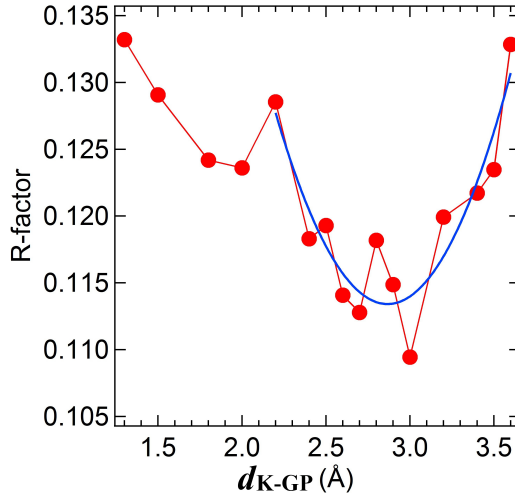


**Figure 7.4:** R-factor dependence on the K-graphene distance,  $d_{\text{K-GP}}$ . The red dots are the calculated values of the R-factor, whereas the blue curve describes the parabolic fit used to determine the position yielding the lowest R-factor.

the DFT predictions mentioned before, thus further supporting the reliability of both results.

Our final results are illustrated in fig. 7.5, where the experimental XPD patterns acquired at different photon energies are shown (left column), together with the corresponding simulated patterns (right column). The partial R-factors obtained for each photon energy are also reported, and the total R-factor calculated over the whole data set is displayed at the bottom. An excellent agreement can be already evidenced from a qualitative comparison between the experimental and the theoretical modulation functions. Besides the correct azimuthal periodicity, also the position and the relative intensity of the diffraction features are reproduced fairly well in all the simulations. More precisely, in the 2D modulation functions collected at 360 and 400 eV photon energies, the six-fold highest amplitude modulation features are found at large polar angles for both in the experimental and simulated patterns. The experimental pattern corresponding to the photon energy of 500 eV displays a star-like shape cut by several dark stripes visible in the central region, which appears with the same shape and at the same position within the simulated one. Finally, in the experimental pattern of 600 eV, this feature assumes the shape of snowflakes, which is also produced correctly by the XPD simulations.

Despite the very low total R-factor, 0.11, the partial R-factors, except for the 400 eV case, are pretty large. By definition, the global R-factor is not the arithmetic mean of the partial R-factors, but their weighted average. The weight associated to each pattern is defined as the absolute value of the modulation amplitude. The larger the amplitude of a particular modulation function, the more significant its contribution is to the value of the averaged R-factor.

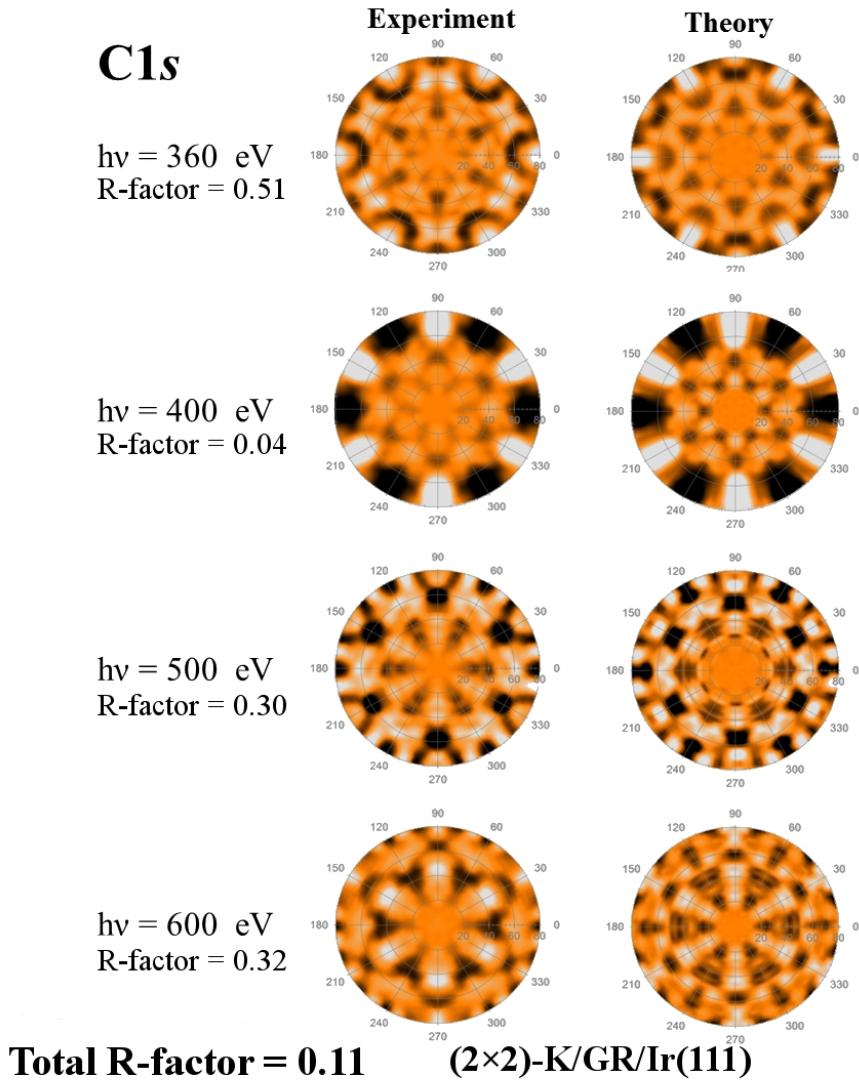


**Figure 7.5:** Comparison between the experimental diffraction patterns of the C1s core level and the simulated ones.

Since the pattern measured at 400 eV shows the largest modulation amplitude, it has the heaviest weight in the whole data set, and it lowers significantly the total R-factor. On the contrary, although the XPD pattern at 360 eV photon energy has a large partial R-factor, this doesn't appreciably raise the average value, because the photoemission signal at 360 eV shows smaller modulations than at 400. The weighted average method just described is one of the strong points of the procedure used to calculate the Pendry's R-factor. In fact, the larger is the modulation amplitude of a certain XPD pattern, the less it is affected by unwanted noise, which would introduce variations not related to real

structural effects.

## 7.5 Conclusions

In this chapter the XPD results obtained for the  $(2\times 2)$ -K/GR/Ir(111) phase have been discussed. The comparison between experimental data with DFT calculations allowed a thorough structural analysis, concerning both the K adsorption site and the adlayer-graphene distance. Relaxing the distance between the K overlayer and the graphene sheet, we obtained a best estimate of  $2.90 \pm 0.25$  Å, which is in very good agreement with the DFT result ( $2.88 \pm 0.50$  Å). This value is slightly larger than those found in the case of the  $(2\times 2)$ -K/graphite structure ( $2.79$  Å [16] and  $2.82$  Å [15]), but well within our experimental error bars. Besides the errors, a possible reason is given by the different extent of charge transfer from the K adatoms to the graphene layer and to graphite. K atoms adsorbed on graphite can interact with more substrate layers, and hence donate more charge per C atom compared to K atoms deposited on a quasi-free-standing graphene monolayer. Since the fewer electrons are donated to the substrate, the larger is the ionic radius of the K atoms, then the smaller charge transfer to the graphene sheet leads to a larger interlayer distance.

In addition, comparing the diffraction patterns of the two  $C1s$  core level photoemission components has shed light on the origin of the satellite structure that appears on the high BE side of the main peak. Since both components show similar XPD modulations, we have ruled out the hypothesis that they originate from geometrically non-equivalent carbon atoms. Interestingly, similar satellite structure in the  $C1s$  core level spectrum has been observed also in the case of the  $(2\times 2)$ -K/graphite(0001) surface, and photoemission studies on this system have led to identical conclusions. Besides the satellite structure, the BE shift and the spectral broadening effect of the main component have been discussed by using the close similarity between the  $C1s$  spectrum of the  $(2\times 2)$ -K phase formed on graphene and graphite. In the low K coverage phase, the BE shifting and the broadening effects are most likely a consequence of the charge transfer from K to graphene. In fact, previous rigid band model had predicted a CT induced BE increase induced by the higher occupation of the graphite VB. Moreover, a similar ionic-to-metallic transition of the K atoms on increasing K coverage has been observed for the K adlayer grown both on graphene and on graphite [4,15]. In correspondence to the formation of the  $(2\times 2)$  phase, a large charge rearrangement inside the K layer is observed, which leads to a non-localized carrier distribution. Therefore, the  $C1s$  core level photoelectrons can interact both with the 2D quasi-free electron gas of the K adlayer and with the long-range polarization field produced at the interface by the residual charge transfer from K to C atoms [14].

It should be considered that, the stacked graphite layers can impose some constraints on the adsorption geometry of AM atoms. By contrast, the AM atoms supported on a single graphene layer are free to migrate, that the interactions between overlayer atoms have a stronger 2D character. For this reason,

some differences can arise between the interaction mechanisms responsible for the K-GR bonding and those involved in the K-graphite system [4]. In conclusion, additional studies on the K-GR system are needed in order to describe in detail the nature of the photoelectron excitation process which produces the high BE shoulder in the C1s XPS spectrum.

## References

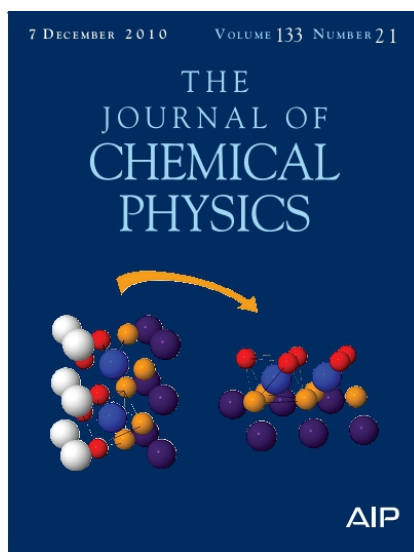
- [1] Caragiu, M. & Finberg, S. Alkali metal adsorption on graphite: a review. *J. Phys.: Condens. Matter* **17**, R995 (2005).
- [2] Chen, J.-H. *et al.* Charged-impurity scattering in graphene. *Nat. Phys.* **4**, 377 (2008).
- [3] Bianchi, M. *et al.* Electron-phonon coupling in potassium-doped graphene: angle-resolved photoemission spectroscopy. *Phys. Rev. B* **81**, 041403 (2010).
- [4] Jin, K.-H., Choi, S.-M. & Jhi, S.-H. Crossover in the adsorption properties of alkali metals on graphene. *Phys. Rev. B* **82**, 033414 (2010).
- [5] Ishida, H. & Palmer, R. E. Electronic structure and phase transitions of submonolayer potassium on graphite. *Phys. Rev. B* **46**, 15484 (1992).
- [6] Ohta, T., Bostwick, A., Seller, T., Horn, K. & Rotenberg, E. Controlling the electronic structure of bilayer graphene. *Science* **313**, 1130681 (2006).
- [7] Bostwick, A., Ohta, T., Seller, T., Horn, K. & Rotenberg, E. Quasi particle dynamics in graphene. *Science* **313**, 1130681 (2006).
- [8] N'Diaye, A. T., Bleikamp, S., Feibelman, P. J. & Michely, T. Two-dimensional Ir cluster lattice on a Graphene Moire on Ir(111). *Phys. Rev. Lett.* **97**, 215501 (2006).
- [9] Coraux, J. *et al.* Growth of graphene on Ir(111). *New J. Phys.* **11**, 023006 (2009).
- [10] Lizzit, S. *et al.* Band dispersion in the deep 1s core level of graphene. *Nat. Phys.* **6**, 345 (2010).
- [11] Lacovig, P. *et al.* Growth of dome-shaped carbon nanoislands on Ir(111): the intermediate between carbidic clusters and quasi-free-standing graphene. *Nat. Phys.* **6**, 345 (2010).
- [12] N'Diaye, A. T., Coraux, J., Plasa, T. N., Busse, C. & Michely, T. Structure of epitaxial graphene on Ir(111). *New J. Phys.* **10**, 043033 (2008).
- [13] Bennich, P. *et al.* Photoemission study of K on graphite. *Phys. Rev. B* **59**, 8292 (1999).
- [14] Lugo-Solis, A. & Vasiliev, I. *Ab initio* study of K adsorption on graphene and carbon nanotubes: role of long-range ionic forces. *Phys. Rev. B* **76**, 235431 (2007).
- [15] Ancilotto, F. & Toigo, F. First-principles study of potassium adsorption on graphite. *Phys. Rev. B* **47**, 13713 (1993).

- [16] Ferralis, N. *et al.* Low-energy electron diffraction study of potassium adsorbed on single-crystal graphite and highly oriented pyrolytic graphite. *Phys. Rev. B* **70**, 245407 (2004).

## Appendix A

# Publications

- [1] **R. R. Zhan**, E. Vesselli, A. Baraldi, S. Lizzit, and G. Comelli, “The Rh oxide ultrathin film on Rh(100): An x-ray photoelectron diffraction study”, *J. Chem. Phys.* **133** 214701 (2010). SELECTED AS JOURNAL COVER.



- [2] S. Surnev, F. Allegretti, **R. R. Zhan**, A. Baraldi, E. Vesselli, G. Comelli and F. P. Netzer. “Surface structure and properties of nickel oxide layers grown on Rh(111)” (paper in preparation).
- [3] F. Allegretti, C. Franchini, **R. R. Zhan**, A. Baraldi, S. Lizzit, S. Surnev and F. P. Netzer, “Structural determination of a two-dimensional  $M_nO_y$  oxide on a stepped Pd(1 1 21) surface” (paper in preparation).
- [4] A. Crepaldi, **R. R. Zhan**, S. Moser, A. Baraldi, K. Kern, C. Carbone and M. Grioni, “ARPES and XPD study of Pb/Ag(100)  $c(6 \times 2)$ : the role of

---

the structural commensurability in the band structure of a Pb monolayer” (paper in preparation).

- [5] M. Bianchi, M. Pozzo, D. Alfè, **R. R. Zhan**, E. Vesselli, A. Baraldi, G. Comelli, Ph. Hofmann, P. Lacovig and S. Lizzit, “A structural investigation of K-doped epitaxial graphene” (paper in preparation).
- [6] E. Miniussi, M. Pozzo, A. Baraldi, E. Vesselli, **R. R. Zhan**, G. Comelli, T. O. Montes, M. A. Niño, A. Locatelli, S. Lizzit, and D. Alfè, “Thermal Stability of Corrugated Epitaxial Graphene Grown on Re(0001)”, *Phys. Rev. Lett.* **106** 216101 (2011).

## Appendix B

# List of the Acronyms

<b>XPD</b>	X-Ray Photoelectron Diffraction
<b>MS</b>	Multiple Scattering
<b>IMFP</b>	Inelastic Mean Free Path
<b>ML</b>	MonoLayer
<b>CLS</b>	Core Level Shift
<b>DFT</b>	Density Functional Theory
<b>ESCA</b>	Electron Spectroscopy for Chemical Analysis
<b>FWHM</b>	Full Width at Half Maximum
<b>LEED</b>	Low Energy Electron Diffraction
<b>SCLS</b>	Surface Core Level Shift
<b>STM</b>	Scanning Tunneling Microscopy
<b>STS</b>	Scanning Tunneling Spectroscopy
<b>GIXRD</b>	Grazing Incidence X-Ray Diffraction
<b>XPS</b>	X-Ray Photoelectron Spectroscopy
<b>TDS</b>	Thermal Desorption Spectroscopy
<b>TPD</b>	Thermal Programmed Desorption
<b>ARPES</b>	Angle-Resolved Photoemission Spectroscopy
<b>CEM</b>	Constant Energy Map
<b>TM</b>	Transition Metal
<b>CT</b>	Charge Transfer
<b>BE</b>	Binding Energy
<b>DOS</b>	Density Of States
<b>UHV</b>	Ultra-High Vacuum
<b>AM</b>	Alkali Metal

---

# Acknowledgment

This dissertation could not have been written without Dr. Alessandro Baraldi and Dr. Erik Vesselli who not only served as my supervisor and co-advisor but also encouraged and challenged me throughout my academic program.

Alessandro has guided me, as a supervisor and a friend, throughout the research projects, never accepting less than my best efforts, thus I've learned how to work out the best results.

Erik is the tutor who knows my strength, and, most of all, my weakness, he has always helped me at the exact moment and in the right way I needed. I've learned a lot from him.

I would like to thank all the colleagues/friends with whom I've worked together throughout these three years.

Thanks a lot to Elisa Miniussi, so brilliant and friendly.

A heartfelt acknowledgment goes to the SuperESCA team, Silvano Lizzit, Paolo Lacovig and Matteo Maria Dalmiglio, great scientists and fantastic people. Thanks also to the nicest and smartest PhD student, Fabrizio Orlando, with whom I've spent a very nice time in Erice.

I would like to express my gratitude to all the collaborators in all my scientific projects reported in this dissertation, without their contributions it was impossible to achieve the results obtained so far. Thanks to Alberto Crepaldi, a dear university colleague and kind co-worker.

Special thanks go to my present family, my parents who raised me to be the person that I am,

and to my future family, Daniele, whom I esteem and believe in.